Probing the Role Played by Magnetic Fields in Star Formation with BLASTPol

by

Laura Marion Fissel

A thesis submitted in conformity with the requirements
for the degree of Doctor of Philosophy
Graduate Department of Astronomy & Astrophysics
University of Toronto

Abstract

Probing the Role Played by Magnetic Fields in Star Formation with BLASTPol

Laura Marion Fissel

Doctor of Philosophy

Graduate Department of Astronomy & Astrophysics

University of Toronto

2013

BLASTPol, the Balloon-borne Large Aperture Submm Telescope for Polarimetry, measures linearly polarized Galactic dust emission in order to map magnetic field morphology in nearby molecular clouds. The role played by magnetic fields in providing support against gravitational collapse of clouds and cores and in forming observed cloud morphology is a key outstanding question in our understanding of star formation. BLASTPol has the unique combination of sensitivity to large scale magnetic fields, and sub-arcminute resolution necessary to trace fields into prestellar cores and dense filaments. Thus BLASTPol provides a crucial link between the low resolution Planck all-sky maps and the detailed but narrow field of view capabilities of ALMA.

The telescope operates simultaneously in three bands at 250, 350 and 500 μm which span the SED peak of 10-20K cold dust. This thesis gives an overview of the instrument, with special focus on the telescope motor control and scanning strategy.

BLASTPol has had two science flights, both launched from Antarctica. The first flight began in December 2010 and lasted for 9.5 days. The 2010 flight had a number of problems, most significantly a damaged IR blocking filter which degraded the optical performance of the telescope. The second BLASTPol flight began in December 2012 and had much better instrument performance resulting in 12.5 days of science data.

The performance of the instrument is reviewed, with the goal of providing insight for future BLASTPol flights and balloon telescopes.

Reduction of the 2010 flight data was challenging because of the systematics associated with the damaged IR blocking filter. A review is given of the data reduction pipeline, instrumental polarization characterization, and a series of null consistency tests designed to reject polarization pseudo-vectors contaminated by systematics. This pipeline was tested with timestreams generated from an instrument simulator. The goal of these simulations was to show that the BLASTPol instrument can be used to reconstruct polarization morphology.

The 2012 data is of better quality and preliminary data reduction products have been run through the 2010 pipeline. Though the resulting maps are preliminary they highlight the potential of these data to provide the most detailed maps to date of magnetic field morphology in molecular clouds. These maps will be used to study the relationship between large and small scale magnetic fields in molecular clouds, the degree of order in the field, and the relationship between the magnetic field structure and the morphology of filaments and cores within the clouds.

Acknowledgements

First I would like to thank Barth Netterfield for his mentorship while acting as my Ph.D. supervisor. When I started my PhD I had plenty of enthusiasm but no absolutely experience in instrumentation. Barth not only had incredible patience in answering my endless series of questions but also faith in my ability to take responsibility for key components of BLASTPol. His encouragement and infectious enthusiasm for ballooning and science in general have made the past seven years incredibly rewarding.

I would also like to thank the members of my thesis committee Chris Matzner and Marten van Kerkwijk for their encouragement and guidance over the years.

I have been very fortunate to work with an amazing team as part of the BLAST collaboration. I would like to thank Mark Devlin, Giles Novak, Enzo Pascale, Jeff Klein and Matt Truch for sharing their wealth of experience with me. It has been fantastic to learn from you and I couldn't ask for a better group of mentors. It has also been an enormous privilege to work with all the incredibly talented members of the BLAST team. Thank you to Elio, Tristan, Tyr, Nick, Josh, Greg, Andrei, Lorenzo, Tony, Brad, Natalie, Steve, Juan and Jamil for making our many field campaigns amazing experiences.

Thank you as well to all of the staff at the Columbia Scientific Balloon Facility with special thanks to Joseph Jones, our CSBF engineer for both BLASTPol flights, and Victor Davison who provided information on the BLAST flight ladder and parachute that was used for the flight train spring constant calculations in Chapter 2. I would also like to thank all the US Antarctic Program contractors at McMurdo Station for putting in so much time and effort in order to allow us do our science.

I also want to thank the astronomers at the National Research Council in Victoria, at the institute formerly known as the Herzberg Institute of Astrophysics, for their support and encouragement throughout my undergraduate and graduate studies.

I would especially like to thank Brenda Matthews, James Di Francesco and Doug Johnstone for sharing their expertise in star formation and for many illuminating discussions on the potential of the BLASTPol data.

I have been very lucky to have an amazing group of friends who have sustained me through my graduate studies. To Mike, Rachel, Deborah and Josh thank you for being endlessly enthusiastic about my research and going on adventures with me in the wilderness of Vancouver Island when I needed a break. Thank you also to my friends from graduate school Sherry, Ivana, Mirza, Libby, Santiago and Daniela for your companionship and support over the past seven years. Also a very special thank you to Cindy Choi who has done an amazingly thorough job of proofreading my text.

Finally I would like to thank my family. This thesis really would not have been possible without the endless support and encouragement of my parents David and Bernadette, my brother Steven and my sisters Sara and Rosemary. I love you and I dedicate this thesis to you.

Contents

List of Tables

List of Figures

Chapter 1

Introduction

1.1 Overview

Understanding the formation of stars is crucial to understanding our observable universe. Without the foundations of star formation theory it would be impossible to construct models of galaxies, chemical evolution of the universe, or planet formation. Despite major advances in recent decades, there are a number of important unsolved problems in star formation.

A major outstanding question in star formation is the role that magnetic fields play in the star formation process. According to some theories magnetic fields play a dominant role in setting both mass and timescales for star formation (see for example Shu et al. (1987); Basu & Ciolek (2004)). According to other theories magnetic fields are relatively unimportant, and it is supersonic turbulence that controls star formation (e.g. Mac Low & Klessen (2004)). In other star formation theories both magnetic fields and turbulence play important roles (Nakamura & Li 2008; 2011).

Magnetic fields are difficult to measure, especially in dense molecular clouds. One method of observing magnetic field structure in star forming regions is to detect polarized submillimeter or millimeter emission from dust grains aligned with the local

magnetic field. Maps of polarized dust emission can be then used to trace magnetic field morphology across the molecular cloud.

The Planck satellite will map the polarization of the whole sky but at only $\sim 5'$ resolution, meaning Planck will have only a few independent polarization measurements per molecular cloud (Planck Collaboration et al. 2011). ALMA (Brown et al. 2004) will map polarization structure in prestellar and protostellar cores and disks but with no sensitivity to larger scale magnetic fields.

My Ph.D. research focused on the design, construction, science planning and data analysis for BLASTPol, the Balloon-borne Large Aperture Submillimeter Telescope for Polarimetry, an experiment designed to map magnetic fields in molecular clouds. BLASTPol observes simultaneously at 250, 350 and 500 μm, with $30''$ diffraction limited resolution at 250μm. BLASTPol is unique in that it can trace magnetic fields across entire molecular clouds with resolution sufficient to follow the fields down into dense cloud substructures, such as cores and dense filaments. In this way BLASTPol bridges the gap between the polarization capabilities of Planck and ALMA.

In this chapter I give scientific background information, explain the advantages BLASTPol has over many other polarimeters and the scientific goals of the experiment. In Chapter 2 I give an overview of the experiment with a particular focus on the systems I was involved in designing: the motor control systems, polarimetry strategy, and motor control software. Chapter 3 focuses on the flight planning work I led and the performance of the instrument during the two BLASTPol science flights. Chapter 4 reviews the analysis pipeline and shows that the instrument can actually reconstruct polarization through consistency checks and simulations, even though the 2010 data had a number of problems. Chapter 5 gives an overview of the data collected in the latest BLASTPol flight launched in late December 2012 and presents preliminary maps of magnetic field morphology in three molecular clouds. A brief summary follows.

1.2 Basic Theory: The Role Magnetic Fields Play in Star Formation

Using the virial theorem, one can analyze the effects of self-gravity, gas pressure and magnetic fields on molecular clouds. In its Lagrangian form (i.e. assuming fixed mass) the virial theorem is

$$\frac{1}{2}\ddot{I} = 2\left(\mathcal{T} - \mathcal{T}_{\mathcal{S}}\right) + \mathcal{B} + \mathcal{W} \tag{1.1}$$

(Chandrasekhar & Fermi 1953), where $I = \int r^2 dm$ is the generalized moment of inertia. Here

$$\mathcal{T} = \int_{V_{cl}} \left(\frac{3}{2}P_{th} + \frac{1}{2}\rho v^2\right) dV = \frac{3}{2}\bar{\rho}\sigma^2 V_{cl} \tag{1.2}$$

is the total kinetic energy of the cloud, where V_{cl} is the cloud volume, σ is the 1D mean velocity dispersion, including thermal (σ_{th}), bulk motion and turbulence (σ_{nt}) contributions, and $\bar{\rho}$ is the mean cloud density. The term $\mathcal{T}_{\mathcal{S}}$, represents the surface kinetic term $\mathcal{T}_{\mathcal{S}} = \oint P_{th}\vec{r}\cdot d\vec{S}$. The energy from the magnetic field is $\mathcal{B}$

$$\mathcal{B} = \frac{1}{8\pi}\int_{V_{cl}} B^2 dV + \frac{1}{4\pi}\oint \vec{r}\cdot\left(\vec{B}\vec{B} - \frac{1}{2}B^2\vec{I}\right)\cdot d\vec{S}. \tag{1.3}$$

Finally, $\mathcal{W}$ is the gravitational energy, which if the acceleration due to outside masses is negligible, is just equal to the self gravity $(1/2)\int \rho\psi\, dV$ or

$$\mathcal{W} = -\frac{3}{5}a\left(\frac{GM^2}{R}\right), \tag{1.4}$$

the gravitational energy of a uniform sphere with an extra factor a to account for deviations in shape and density distribution. The simplest case is an unmagnetized cloud in virial balance supported solely by thermal gas pressure. Bonnor (1956) and Ebert (1957) showed that the maximum mass for such a cloud is

$$M_{BE} = 1.182\frac{\sigma_{th}^3}{\left(G\,\rho_0\right)^{1/2}} = 0.66\left(\frac{T}{10\,K}\right)^2\left(\frac{P_{th}}{3\times 10^5\,k_b\,cm^{-3}\,K}\right)^{-1/2} \tag{1.5}$$

which is of order a solar mass for typical conditions in dense clumps in low mass star forming regions (McKee & Ostriker 2007).

The relative importance of the magnetic field in supporting a cloud against gravitational collapse is usually quantified by the mass to flux ratio $\mu_\Psi \equiv M/M_\Psi$[1] where M_Ψ is the magnetic critical mass defined such that $\mathcal{B} = |\mathcal{W}|$ for a cold cloud in equilibrium:

$$M = c_\Psi \frac{\Psi}{G^{1/2}} \tag{1.6}$$

where Ψ is the magnetic flux threading the cloud (in the simplest case for a uniform poloidal field through a spherical cloud $\Psi = \pi r^2 B$) and c_Ψ is a constant of order unity which depends on the distribution of magnetic fields and density within the cloud. A cold cloud with a constant mass to flux ratio poloidal field has $c_\Psi \approx 0.17$ (Tomisaka et al. 1988). If $\mu_\Psi > 1$ the cloud is *supercritical* and the magnetic field cannot prevent gravitational collapse on its own. For a cold cloud where $\mu_\Psi < 1$ the cloud is said to be subcritical, and gravitational collapse of this cloud is not possible. In order for a subcritical core to collapse either the mass must change (e.g. from flows along field lines), or μ_Ψ must change via *ambipolar diffusion*.

Ambipolar diffusion results from magnetic field lines in dense regions not being perfectly frozen to the gas. The magnetic field only interacts directly with ions and charged grains. Neutrals may drift through the magnetic field lines. In the diffuse ISM, where the ionization fraction is much higher ($\geq 10^4$), the gas is well coupled to the magnetic fields and ambipolar diffusion is negligible (Smith, M.D. 2004). However in dense, shielded regions ionization is primarily due to cosmic ray interaction, thus the ionization fraction is low and the gas to field coupling is weaker. The resulting length scale of ambipolar diffusion is:

$$l_{AD} = \frac{v_A}{n_i \alpha_{ni}} \approx 0.05 pc \left(\frac{v_A}{3\, km\, s^{-1}}\right) \left(\frac{n_i}{10^3\, cm^{-3}}\right)^{-1} \tag{1.7}$$

(McKee & Ostriker 2007) where n_i is the ion fraction, v_A is the Alfvén speed and α_{ni} is the ion-neutral collision rate coefficient. Under the "classical" theory of star formation

[1] In some papers μ_Ψ is defined as M/Ψ in units such that the critical μ_Ψ=1. This is equivalent to the above definition.

(e.g. Shu et al. (1987)) most observed prestellar cores were thought to be quiescent and subcritical, eventually to collapse once ambipolar diffusion caused μ_Ψ to become >1. More recently this argument has been challenged by a model where cloud support is dominated by turbulence and observed structures have lifetimes of order their sound crossing time (see Mac Low & Klessen (2004) for an overview). In order to test star formation theories more observations of magnetic fields are needed.

1.3 Measuring Magnetic Fields

A number of different methods have been used to trace magnetic fields in star forming regions. On the largest scales the Galactic field has been determined by both synchrotron emission caused by high energy cosmic rays spiralling about magnetic field lines, and Faraday rotation of pulsar emission. Such observations have led to a local field strength estimate of $6 \pm 2\,\mu$G (Beck 2001).

The only way to directly measure magnetic field strengths in molecular clouds is to observe Zeeman splitting of line emission. By measuring the Stokes I and V spectra of the line, one can fit for both the direction and magnitude of the line-of-sight magnetic field component B_{LOS} (Heiles & Crutcher 2005). However the line splitting Δv_z is generally very small, such that even for lines at radio frequencies the line width $\delta v >> \Delta v_z$ so Zeeman splitting observations are sensitivity limited.

1.3.1 Dust Polarization

Dust polarization observations can be used to map the direction of B_{POS}, the local magnetic field direction projected on the plane of the sky. Polarized dust emission requires both non-spherical dust grains (or at least grains with anisotropies in surface composition) and a method for aligning the grains with the local magnetic field. This alignment process need not be instantaneous, but must be fast compared to the typical

collision timescale that would destroy the alignment of a grain with respect to the magnetic field.

Alignment of dust grains with an external magnetic field is an area of active research. A good review of different grain alignment mechanisms can be found in Lazarian (2007). It is currently believed that the dominant mechanism for grain alignment is the result of torques produced by anisotropic radiation fields (Hoang & Lazarian 2008). These torques are thought to be capable of aligning grains in relatively dense clouds $A_V \sim$10 (Bethell et al. 2007).

If the grains are on average aligned so that their long axes are perpendicular to the local magnetic field direction, then optical light from a background star is most likely to be absorbed if its electric field vector is aligned with the plane that contains the long axis of the grain (see Figure 1.1). *Thus starlight polarized from selective extinction due to magnetically aligned grains should have a net polarization in the direction of the plane of sky magnetic field component* B_{POS}. On the other hand thermal emission from magnetically aligned grains are more likely to have electric field vectors along the plane containing the long axis. By the same logic *thermal emission from magnetically aligned grains should have a net polarization perpendicular to* B_{POS}. Thus by observing the polarized dust emission from a molecular cloud and rotating the polarization vectors by 90°one gets a map of the direction of B_{POS}.

Linear polarization can be characterized by measuring the linear Stokes parameters I, Q and U. Stokes I is the total intensity. Stokes Q and U are defined as follows:

$$Q = p \cos 2\Phi, \tag{1.8}$$

$$U = p \sin 2\Phi, \tag{1.9}$$

where Φ is the position angle of polarization pseudovector $\vec{E}$ and p is the degree of polarization defined as:

$$p = \frac{\sqrt{Q^2 + U^2}}{I}. \tag{1.10}$$

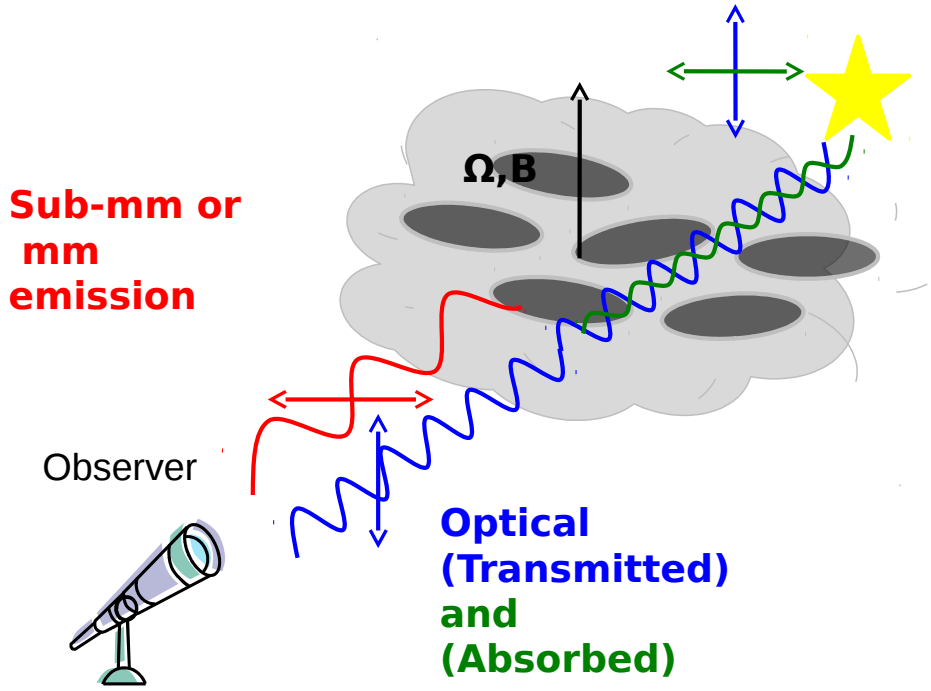

Figure 1.1: Cartoon showing showing the geometry of polarized radiation from dust grains with long axes preferentially aligned perpendicular to the cloud magnetic field. Optical/near infrared photons from background stars are preferentially absorbed if the electric field vector $\vec{E}$ is parallel to the grain long axis. The result is that an observer sees a net linear polarization of background starlight parallel to the local magnetic field direction projected on the sky B_{POS}. A dust grain is more likely to emit radiation with $\vec{E}$ parallel to the grain long axis, resulting in a net polarization perpendicular to B_{POS}.

Polarization is usually plotted with line segments showing the inferred orientation of B_{POS} (Φ for optical polarimetry, $\Phi + \pi/2$ for submm polarimetry), with the length proportional to p. Φ has a 180° ambiguity, as such measurements of polarization can be used to infer the *orientation* but not the *direction* of the magnetic field lines. We therefore refer to these line segments as pseudovectors rather than true vectors[2].

The degree of polarization p is not directly related to the magnetic field strength. It is typically found to be a few percent, with lower polarization strengths seen in high density regions and higher p values found in lower density cloud regions (Matthews et al. 2009).

1.4 Observations of Magnetic Fields in Star Forming Regions

1.4.1 Zeeman Splitting Observations

The largest sample of Zeeman splitting measurements of B_{LOS}, the line-of-sight magnetic field strength in molecular clouds is reviewed in Crutcher (2012). They take B_{LOS} measurements for a number of clouds and construct a probability density function of B_{LOS} which is used to infer information about the underlying probability density function of B_{TOT}. Bayesian analysis suggests that most molecular clouds have turbulent and magnetic field energies which are comparable, and that in a few cases magnetic energy may dominate over turbulent energy. At low densities ($n_H <\sim 300\,\mathrm{cm}^{-3}$) the maximum magnetic field strength is consistent with a fairly constant $\sim 10\mu$G, while at higher densities the clouds are consistent with a mean mass to flux ratio of 2-3, suggesting that the clouds are generally supercritical and that magnetic pressure alone is insufficient to balance gravitational contraction.

[2]Technically they are Spin-2 tensors.

1.4.2 Optical and Near-infrared Polarimetry

Most maps of magnetic field structure across molecular cloud complexes are from optical or near infrared polarimetry. Optical polarimetry provides a "pencil beam" measurement of the magnetic field direction along the line-of-sight to a background star, but can only probe the relatively low density regions of the cloud (A_V of a few).

Goodman et al. (1990) used optical polarimetry to map magnetic field morphology in three nearby star forming complexes: Taurus, Ophiuchus and Perseus. They found that the pseudovector directions had considerable uniformity over large distances, but that the angle between B_{POS} and individual filamentary clouds within the complexes varied significantly.

In the Taurus, FCRAO observations of low column density gas ($A_V < 2$) traced by ^{12}CO and ^{13}CO J=1-0 show striations aligned with the local magnetic field direction (Goldsmith et al. 2008; Heyer et al. 2008). Heyer et al. (2008) calculated $\langle \mu_\Phi \rangle = 0.27$ implying that the cloud envelope is subcritical and dominated by magnetic support. Herschel observations of nearby clouds have found tenuous sub-filaments or striations that are perpendicular to the main filaments, and in several cases where complementary polarimetry observations exist, appear to align parallel to B_{POS} (Palmeirim et al. 2013) (Figure 1.2). These observations suggest that dust and gas might be accreting onto clouds along magnetic field lines. However in order to probe the magnetic field inside the dense filaments where stars are forming submm or mm polarimetry is required.

1.4.3 Submillimeter and Millimeter Polarimetry

Submm polarimetry has been used to map B_{POS} for a large number of clouds. Two of the most prolific instruments were the SCUPOL polarimeter on the James Clerk Maxwell Telescope (Matthews et al. 2009) and the Hertz polarimeter at the Caltech Submillimeter Observatory (Dotson et al. 2010). Most of these polarization maps

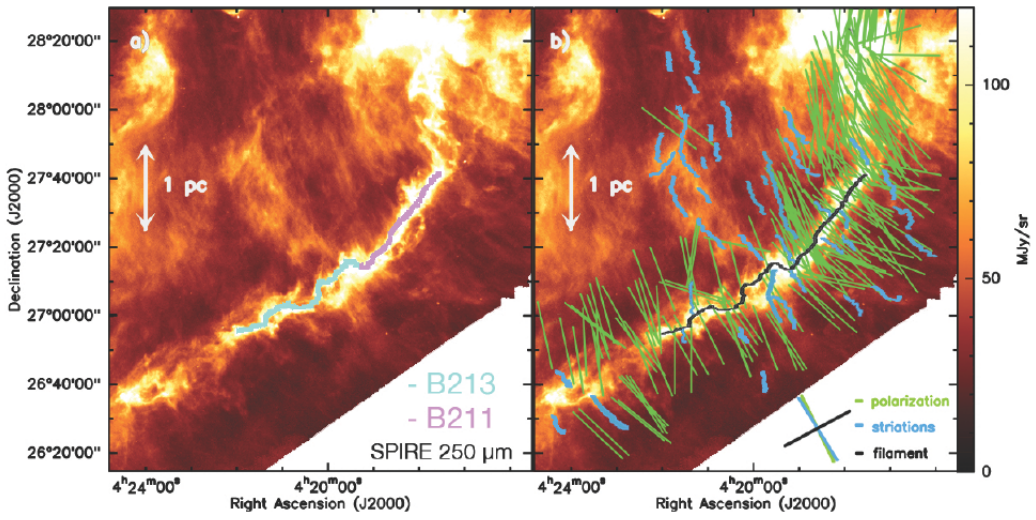

Figure 1.2: From Palmeirim et al. (2013): *a)* Herschel 250μm observation of the B211/B213/L1495 region of Taurus with the main filaments labeled. *b)* Herschel 250μm map with optical and infrared polarimetry showing B_{POS} (green lines), and CO striations found by Heyer et al. (2008) (blue lines) overlaid.

have been fairly small, mapping field structure on the scale of cores, or nearby dense filaments (for example the Orion filament mapped by Matthews et al. (2001) with the SCUBA polarimeter).

The degree of polarization can be very low for bright compact objects, for example the central region of G 331 has p <0.2% in 450 μm observations taken with the SPARO polarimeter (Li et al. 2006). Many observations have found a decrease in p with increasing submm intensity (Matthews et al. 2001). This so called depolarization effect could be due to beam dilution of tangled magnetic field structures, a decrease in grain alignment efficiency at high densities or a change grain properties at high densities.

The only large scale dust polarization maps to date have come from 450 μm observations of four bright giant molecular clouds (GMCs) with the SPARO instrument (Li et al. 2006). Li et al. (2006) found evidence of large scale organization of magnetic fields, implying that they contribute a significant fraction of energy to cloud support. However SPARO's beam FWHM of 4′ means it only traces large scale magnetic fields.

1.4.4 Estimates of Field Strength from Polarization Observations

It is not possible to calculate field strength directly from the measured degree of polarization, as even weak fields can align dust grains. Chandrasekhar & Fermi (1953) outlined a method (hereafter the CF method) to use the dispersion in the measured magnetic field angles to estimate magnetic field strength. The method depends on the fact that turbulent motions in the gas will lead to random deviations in the magnetic fields due to freezing of the field to the gas. Thus observing the irregularities in B_{POS} gives an estimate of the magnitude of B_{POS}:

$$B_{POS} \;=\; Q\sqrt{4\pi\rho}\frac{\delta v}{\delta\Phi} \;\approx\; 9.3\sqrt{n(H_2)}\frac{\Delta v}{\delta\Phi}\mu G, \tag{1.11}$$

(Heiles & Crutcher 2005), where Q is a factor of order unity, ρ is the gas density, δv is the one dimensional velocity dispersion, $\delta\Phi$ is the dispersion in polarization angle (in degrees), $n(H_2)$ is the gas number density and Δv is the velocity FWHM. Ostriker et al. (2001) applied the CF method to isothermal cloud simulations and found that the CF formula could predict reasonably accurate strengths of strong fields if a Q value of 0.5 was used (where Q is used to correct for the smoothing of a tangled magnetic field along the line of sight). Hildebrand et al. (2009) adapted the CF method to clouds where there is ordered structure in B_{POS} that is not associated with turbulence, by calculating the polarization angular dispersion function. Houde et al. (2009) further refined this method by including integration over the telescope beam and turbulent cells along the line of sight.

1.5 BLASTPol

1.5.1 Instrument

My PhD research has focused on the construction, mission planning, science campaign and now data analysis for BLASTPol (Fissel et al. 2010). BLASTPol is the reconstructed

BLAST telescope (Pascale et al. 2008), with additional polarimetry capability. Using a 1.8 m Cassegrain telescope, BLASTPol images the sky onto a focal plane consisting of bolometric detector arrays at 250, 350 and 500 μm. The polarimeter consists of polarizing grids mounted in front of bolometric detector arrays, with a rotating achromatic half wave plate. BLASTPol maps linearly polarized dust emission with a diffraction limited beam FWHM of 30″at 250 μm.

1.5.2 Advantages of a Balloon Platform

Observing magnetic fields in the densest regions of molecular clouds generally requires submillimeter or millimeter polarimetry, where the emission is optically thin. However, most ground based polarization observations have been limited to mapping cores and dense filaments (Matthews et al. 2009; Dotson et al. 2010). Opacity from atmospheric water vapour requires ground based polarimeters to either observe in narrow windows in the atmospheric transmission spectrum, or observe at millimeter wavelengths, far from the peak of the SED of cold dust (T$\sim$10-30k). BLAST and later BLASTPol were designed to operate on a stratospheric balloon platform, where the atmospheric transmission is almost 100% (see Figure 1.3).

A balloon platform gives BLAST several advantages over ground based polarimeters:

- Because BLAST does not have to observe through narrow windows in the atmospheric transmission spectrum the three BLAST bands at 250, 350 and 500μm were chosen to bracket the SED peak of 10-20 K dust. For example 12 K dust (assuming β=2) should be 4.4, 8.8 and 11.7 times brighter at 250, 350 and 500 μm respectively than at 850 μm, the central frequency of SCUBA polarimeter (Greaves et al. 2003) SCUPol.

- Not observing through atmospheric transmission windows means that the three

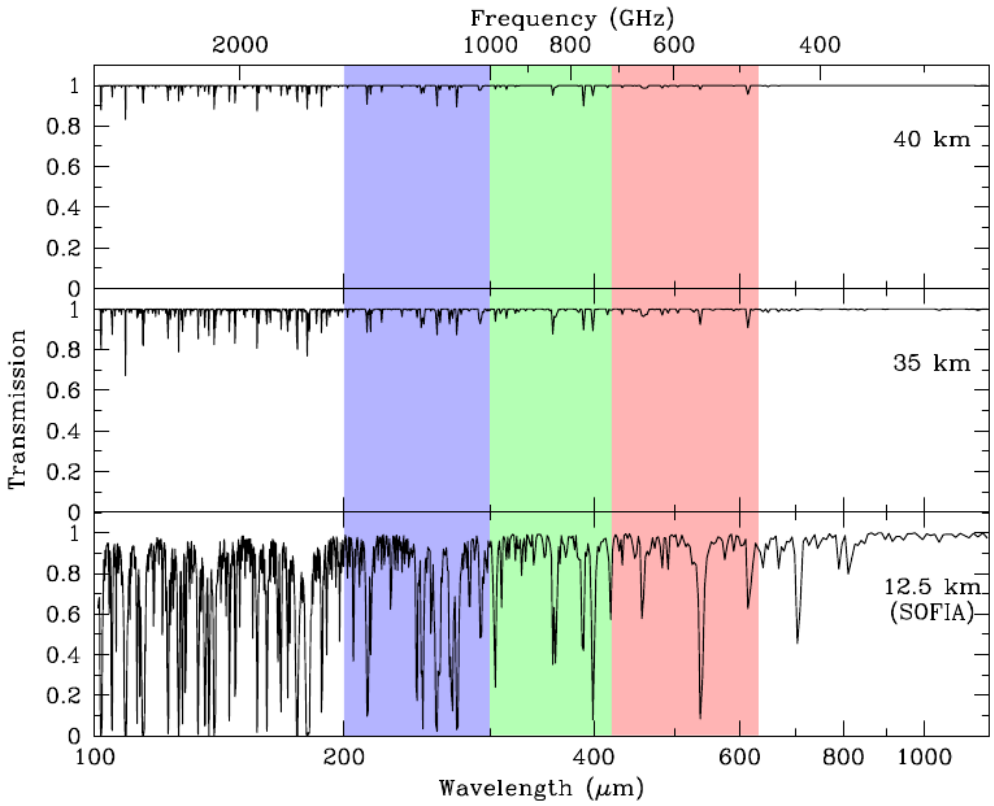

Figure 1.3: Atmospheric transmission at submillimeter wavelengths calculated for the altitudes used by SOFIA and at 35km and 40km above sea level. BLASTPol's at float altitude over two science flights ranged between 36-39 km above sea level. From Wiebe (2008).

BLAST bands were made very wide: $\Delta f/f \sim 30\%$. Indeed, the BLAST bands include most of the radiation between 200-650μm.

- Ground based polarimeters are generally limited by atmospheric loading, which is not the case for BLASTPol.

The disadvantage of a balloon platform is that the time available for observations is limited by the length of the balloon flight. At present summer launches from Antarctica offer the longest stratospheric flights. For Antarctic flights there are no day/night cycles, which require large quantities of ballast to be dropped to maintain a stable altitude, and in the summer stratospheric wind patterns set up in a circumpolar vortex keeping the balloon circling Antarctica (rather than drifting out to sea). Flights longer than one month are possible though BLASTPol only has sufficient cryogens for 10-14 days of science observations.

1.5.3 Potential of BLASTPol Combined with Other Facilities

Observations from the Herschel telescope have shown that clouds contain ubiquitous filamentary structure with characteristic widths of $\sim$0.1 pc (André et al. 2010). Star formation tends to preferentially take place in filaments of high column density ($A_V \geq 8$ mag). The role played by magnetic fields in this picture is unclear. Several examples have been found where optical polarization measurements show field directions which appear perpendicular to the main filament and parallel to sub-filaments or striations (Palmeirim et al. 2013), but no polarimeter has had the combination of sensitivity and resolution to survey the field direction in filaments across entire molecular clouds. With bands covering the same frequencies as Herschel's SPIRE instrument and slightly worse spatial resolution[3] BLASTPol is an obvious follow-up to Herschel.

[3]Herschel 500 μm beam FWHM is 36″, compared to 60″for BLASTPol at the same band.

The Planck surveyor will map polarization of the entire sky at a resolution of $\sim 5'$. Planck will have only have a few pseudovectors per cloud, and it will not have sufficient resolution to probe fields in individual filaments even in nearby Gould's Belt objects ($5'$ corresponds to 0.2 pc resolution at a distance of 150 pc). ALMA will provide high resolution measurements of the magnetic field structure in cores and disks, but it will resolve out all structures on scales of $\sim 60''$or larger. Thus there is a gap between the large spatial scales probed by Planck and the high resolution observations of fields using ALMA polarimetry, which BLASTPol is well suited to fill.

1.5.4 BLASTPol Science Goals

How does magnetic field direction correlate with cloud morphology? Faint, low column density ^{12}CO filaments observed in Taurus (Goldsmith et al. 2008; Heyer et al. 2008) seem to closely follow magnetic field lines traced by optical polarimetry, which could indicate streaming of molecular gas along field lines. BLASTPol will investigate the alignment between intermediate and high density filaments seen in Herschel observations (e.g. Hill et al. (2011)).

How does magnetic field direction correlate with core and protostellar morphology? In a magnetically dominated collapse a flattened inner core or "infall envelope" of $\sim$3000 AU is expected to form with its axis of symmetry parallel to the local magnetic field. The corresponding magnetic field shape is expected to show a pinched, or "hour glass" structure (Girart et al. 2009). If cores are supported by magnetic fields and collapsing along field lines, then there should be a positive correlation between the core minor axes and the local field direction traced by BLASTPol. Similar observations have been made for three nearby starless cores (Ward-Thompson et al. 2000), three low mass protostars (Davidson et al. 2011), and two Bok globules (Ward-Thompson et al. 2009) but a much larger sample size is needed to determine if there is a significant statistical correlation.

How ordered are magnetic fields in molecular clouds? Numerical simulations have shown that molecular clouds with strong magnetic fields show less polarization angle dispersion than clouds with weak fields (Ostriker et al. 2001). Recently, polarization maps have been used to characterize the magnetized turbulence power spectrum (Houde et al. 2011). We plan to apply this analysis to all of our BLASTPol polarization maps.

What is the polarization spectrum of BLASTPol target clouds? The percentage polarization at a particular wavelength is a function of grain composition, alignment efficiency and temperature. The three BLASTPol bands bracket an observed minimum in the polarization spectrum near 350μm (Vaillancourt et al. 2008) providing crucial data points at wavelengths which are difficult to observe from the ground. BLASTPol will make observations of the polarization spectrum over many different clouds and will use the data to probe the alignment efficiency with temperature and dust column.

The ultimate goal for BLASTPol data will be to combine our data with complementary observations (e.g. gas velocity information from molecular line observations, age and evolutionary state based on embedded source populations) and generate quantitative statistics which can be compared to predictions from simulations of star formation.

Chapter 2

The BLASTPol Instrument

2.1 Chapter Overview

In this Chapter I give an overview of the BLASTPol instrument and control software. Particular detail is given on the systems I was responsible for: instrument polarimetry modulation strategy and preflight tests, the motor systems, motor control software, and solar power design. Some of the text in this chapter is adapted from Fissel et al. (2010).

2.2 Introduction

BLASTPol, the Balloon-borne Large Aperture Submillimeter Telescope for Polarimetry, is a stratospheric 1.8 m telescope which maps linearly polarized submillimeter emission with bolometric detectors operating in three 30% wide bands at 250, 350, and 500 μm. BLASTPol's diffraction-limited optics were designed to provide a resolution of 30″, 42″, and 60″ at the three wavebands, respectively. The detectors and cold optics are adapted from those used by the SPIRE instrument on Herschel (Griffin et al. 2003).

BLASTPol is a rebuilt and enhanced version of the BLAST telescope (Pascale et al. 2008) upgraded to include polarization capability. BLAST was designed to conduct confusion-limited, wide-area extragalactic and Galactic surveys at submillimeter (submm) wavelengths from a balloon platform. BLAST had two Long Duration Balloon (LDB) flights. The first was a 4 day flight from Kiruna, Sweden in June of 2005, the second an 11 day flight from Antarctica in December 2006. After termination of the Antarctic flight the parachute could not be detached, which resulted in the payload being dragged $\sim$200 km across the Antarctic plateau in 24 hours. BLAST was largely destroyed, but fortunately the pressure vessel containing the hard drives that stored all of the experimental data was recovered. In addition, the mirrors, detectors and receiver were all recovered and have been used in the construction of BLASTPol.

BLAST provided the first deep, wide area maps at 250, 350 and 500 μmbands that are very difficult or often impossible to observe from even the best ground-based sites in the world. Some science highlights include measurement of the cosmic FIR background at 250, 350 and 500 μm, including a 0.8 deg^2 confusion-limited map in the GOODS South region, where it was shown that more than half of the FIR background light originates in galaxies at redshift$>$1.2 (Devlin et al. 2009; Marsden et al. 2009; Pascale et al. 2009), and the determination of luminosities, masses and temperatures of more than a thousand compact sources in the Vela Molecular Ridge, which may form into stars (Netterfield et al. 2009).

After the BLAST 2006 flight a polarimeter was added and BLAST was transformed into BLASTPol, a uniquely sensitive polarimeter for probing linearly polarized Galactic dust emission. BLASTPol is designed to map the magnetic field structure across a large number star forming regions. These maps will provide a fantastic data set for studying the role magnetic fields play in the star formation process, an important outstanding question in our understanding of how stars form. BLASTPol can map magnetic fields across entire Giant Molecular Clouds (GMCs), with sufficient resolution to probe fields

in dense filamentary sub-structures and molecular cores. The experiment provides a crucial bridge between the large area but coarse resolution polarimetry provided by experiments such as Planck (5′ resolution) and the high resolution (<1″) but small field view (<60″) polarization measurements from the ALMA telescope.

2.3 The BLASTPol Telescope

2.3.1 Optical Design

BLASTPol utilizes a Ritchey-Chrétien telescope consisting of a 1.8 m parabolic primary mirror (M1) and a 40 cm correcting secondary (M2). The field of view of the telescope at 250 μm is $13.5' \times 6.5'$ at the focus. The Offner relay re-imaging system redirects the light to a series of cryogenically cooled (1.5 K) re-imaging optics (M3, M4, M5) arranged in an Offner-relay configuration, with M4 serving as a Lyot stop. Figure 2.1 shows a schematic of the optical path of the BLASTPol telescope and Figure 2.2 shows the layout of the cold optics box.

Radiation emerging from M5 is split into three frequency bands by low-pass edge dichroic filters (Ade et al. 2006), which allow imaging of the sky simultaneously at 250, 350 and 500 μm. Figure 2.3 shows the band-passes of each array measured with a Fourier Transform Spectrograph (Angilè in press). The first dichroic filter reflects wavelengths shorter than 300 μm and transmits longer wavelengths. This reflected light is directed onto a filter directly in front of the 250 μm array, which reflects wavelengths shorter than 215 μm, and is further defined by the waveguide frequency cutoff at the exit of each of the feedhorns coupled to the detector array. For the 350 and 500 μm arrays, the band is defined at the short-wavelength end by the transmission of a dichroic filter and at the long-wavelength end by the waveguide cutoff. Each band has a $\sim$30% frequency width. The frequency performance of the filters was evaluated with Fourier transform spectroscopy.

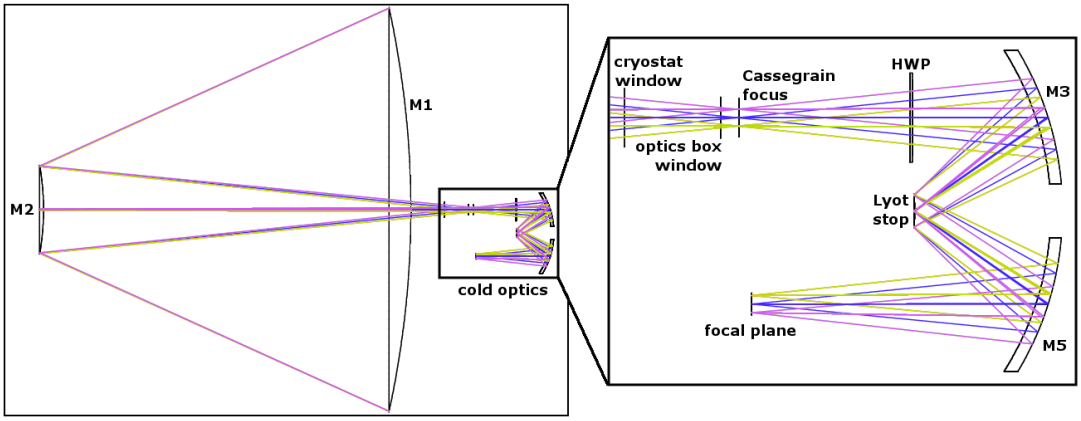

Figure 2.1: Schematic of the optical layout for the BLASTPol telescope and receiver is shown on the left, with the cold optics, located within the cryostat, shown in an expanded view on the right. The image of the sky formed at the input aperture is re-imaged onto the bolometer detector array at the focal plane. M4 serves as a Lyot stop, which defines the illumination of the primary mirror for each element of the bolometer detector arrays. The three wavelength bands are separated by a pair of dichroic beamsplitters (not shown) which are arranged in a direction perpendicular to the plane, between M5 and the focal plane. The position of the half wave plate (HWP), placed 19.2 cm from the focus of the telescope, is labeled.

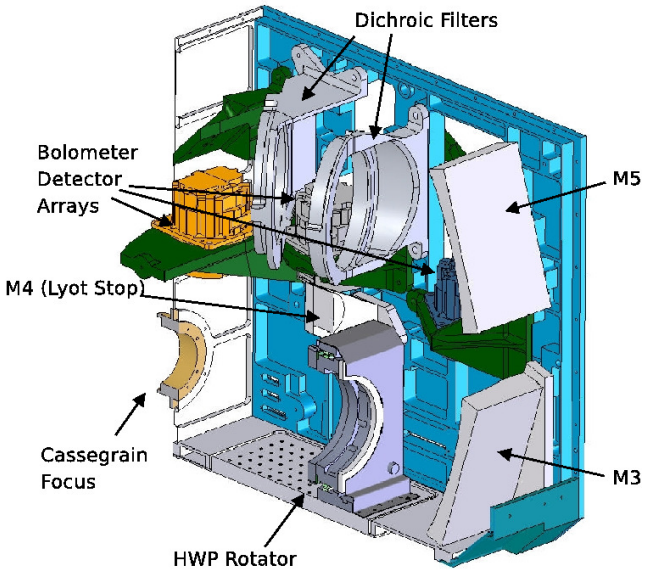

Figure 2.2: A cutaway view of the BLASTPol optics box. The light enters from the lower left and is re-imaged onto the bolometer detector arrays (BDAs). Dichroic filters split the beam into each of the BDAs for simultaneous imaging of the sky at 250, 350 and 500 μm. A modulating half wave plate (HWP) is mounted between the entrance to the optics box and M3, and polarizing grids have been mounted directly in front of each of the BDAs. The stepper motor which rotates the HWP is located outside the optics box.

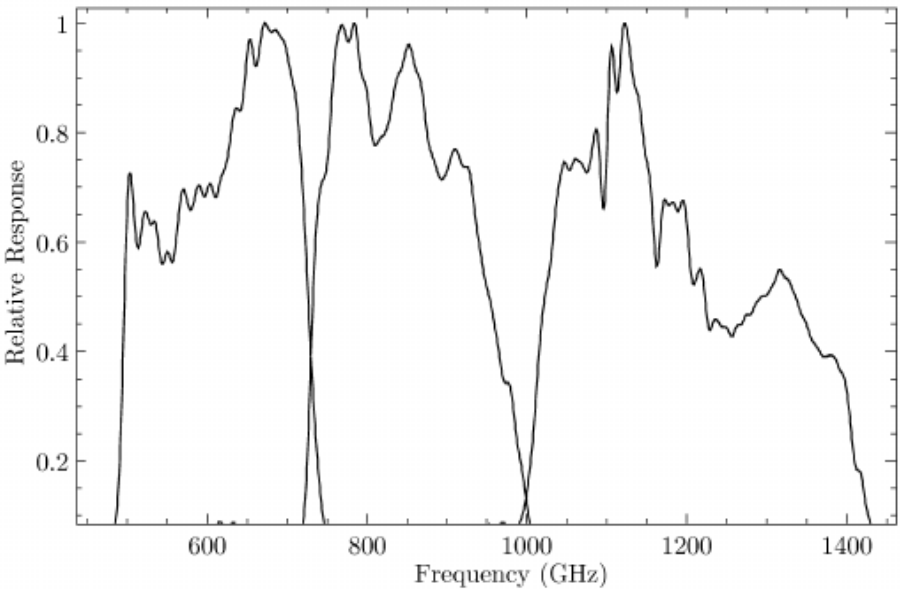

Figure 2.3: Relative frequency response of the BLAST bands from Wiebe (2008). The band-pass of each filter was measured with a Fourier Transform Spectrometer using a nitrogen source and normalized to the peak spectral response. Absorption lines from residual water in the FTS can be seen in all three bands.

The primary mirror from the BLAST 2006 flight was scratched and could not be repaired. A replacement primary mirror was manufactured for BLASTPol. The surface of the new mirror had an RMS of $\sim$1.0 μm. The secondary mirror was also recovered after BLAST 2006 and has been reused for BLASTPol (after resurfacing to remove scratches). The estimated antenna efficiency of the telescope is $> 80\%$, with losses caused by both the roughness of the primary and the quality of the re-imaging optics. More information about the optical design and performance of the BLAST telescope can be found in Olmi (2002) and Pascale et al. (2008).

For the 2010 BLASTPol flight the secondary mirror was mounted directly on the primary mirror supported by carbon fiber struts. After the 2010 flight the mounting was changed when it was discovered that the weight of the secondary mirror was causing a large scale deformation of the primary mirror that was introducing sidelobes (Angilè in press). For the 2012 flight new carbon fiber support struts were manufactured so that the secondary mirror could be mounted on the gondola inner frame.

Temperatures of the primary and secondary mirrors do not remain constant throughout the flight. Diurnal temperature variations of $\sim 10^{\circ}$ C have been observed on previous BLAST flights Pascale et al. (2008). These thermal variations result in changes to the radii of curvature of various optical surfaces. To compensate, the position of the secondary mirror with respect to the primary can be changed in flight by three stepper motor actuators. These actuators are also used to set the original tip/tilt alignment of the secondary. Analysis of the BLAST optical system indicates that the distance between the primary and secondary mirrors must be kept to within 100 μm to avoid significant image degradation.

2.3.2 Detectors

The BLASTPol focal plane consists of 149, 88 and 43 detectors at 250, 350 and 500 μm respectively. The detectors consist of silicon-nitride micro-mesh ("spider-web") bolometric detectors coupled with $2f\lambda$ smooth-walled conical feed-horn arrays. The bolometer detector array design is based on the Herschel SPIRE instrument detectors (Glenn et al. 1998; Rownd et al. 2003). Each array also contains diagnostic channels: two dark bolometers, two thermistors and one resistor. Detector transfer functions have been measured from cosmic-ray hits and typical detector time constants are $\sim$2 ms (Pascale et al. 2008).

For BLAST the detector sensitivity was limited by photon shot-noise loading from the telescope. The total emissivity of the warm optics is dominated by blockage from the secondary mirror and support struts which was estimated to be $\sim$ 7% (Pascale et al. 2008).

The responsivity of the detectors changes with loading and with gain variation in the readout electronics. To correct for the changing responsivity a calibration lamp located in a hole in the Lyot stop (M4) is pulsed for 300 ms every $\sim$15 minutes. Amplitude variations of the calibration pulses as measured by each detector can then be used to correct for the drift in responsivity over time.

Each bolometer is pre-amplified by differential JFET amplifiers which are thermally coupled to the cryostat vapour cooled shield. To reduce the effects of low frequency 1/f noise the detectors are AC biased with a sine wave of frequency $\nu = 200.32$ Hz. The frequency of the sine wave is much higher than the frequencies associated with the signal from scanning the telescope across the sky. The data acquisition electronics are then used to demodulate the detector signals and provide noise stability to low frequencies ($<$ 30 mHz), which allows the sky to be observed in a slowly-scanned mode. The data are collected using a high-speed, flexible, 22-bit data acquisition system, which can synchronously sample up to 600 channels at a sample rate of

10.4 kHz. Output from the bolometer channels is then processed by an Altera FPGA (where the data are low pass filtered at 4 kHz). The data are then processed by an Analog Devices Digital Signal Processor (DSP), where it is demodulated and further low pass filtered to $\sim$30 Hz and a 100.16 Hz sample rate. The resulting time ordered data (hereafter TOD) are then written to disk. More details on the bolometer readout can be found in Pascale et al. (2008).

2.3.3 Cryogenics

For the instrument to operate nominally the detectors must be cooled to $<$300 mK and the re-imaging optics must be cooled to 1.5 K. The BLASTPol receiver contains an optics box mounted inside a long hold-time liquid-nitrogen and liquid-helium cryostat dewar. A closed-cycle ^{3}He refrigerator keeps the detectors at 300 mK during flight. This self-contained, recycling refrigerator can maintain a temperature of 280 mK with 30 μW of cooling power for 4 days. It can be recycled within 2 hours. The ^{3}He refrigerator uses a pumped ^{4}He pot at $\sim$ 1 K for cycling. The pumped pot maintains 1 K with 20 mW of cooling power for outside pressures of 15 Torr or less. The entire optics box containing the re-imaging optics is also cooled to 1.5 K.

2.4 Polarimeter

2.4.1 Overview

Photo-lithographed polarizing grids (see Figure 2.4) are mounted in front of the feed-horn arrays for each bolometer detector array. The grids are patterned with either horizontal (H) or vertical (V) wire orientations (Figure2.5) in order to alternate the polarization component sampled by 90° from horn-to-horn and thus bolometer-to-bolometer along the scan direction . BLASTPol scans primarily in azimuth so a source on the sky passes along a row of detectors, and thus the time required to measure one

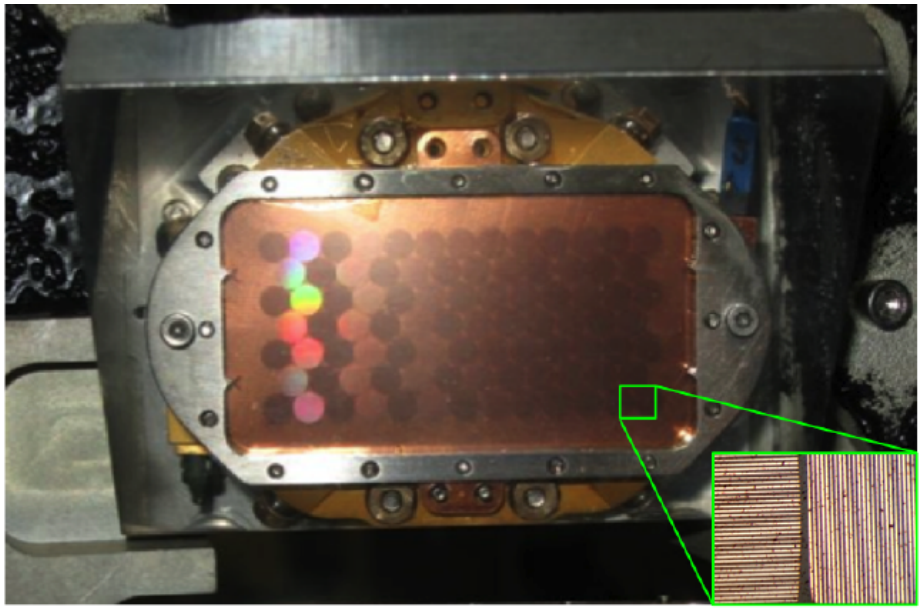

Figure 2.4: Picture of the 350 μm polarizing grid from Angilè (in press). The lower right inset is an enlarged image of the boundary between two grid sections corresponding to two adjacent bolometers, showing where the wire orientation changes from horizontal to vertical.

Stokes parameter (Q or U) is just equal to the separation between bolometers divided by the scan speed. For the 500 μm detector array where the bolometers are separated by 90″, and assuming a typical scan speed of 0.05 °/second, this time would be 0.5 seconds. This timescale is short compared to the characteristic low frequency (1/f) noise knee for the detectors at 0.035 mHz (Pascale et al. 2008).

2.4.2 Half Wave Plate

In order to measure both Stokes Q and U and provide polarization modulation a cryogenic (4 K) achromatic half wave plate (HWP) has been incorporated into the optical design as shown in Figure 2.2. The HWP is mounted inside the optics box 19.2 cm from the Cassegrain focus of the telescope to minimize the modulation of any potential HWP local defects. The predicted modulation efficiency across the BLAST bands is given in Figure 2.7.

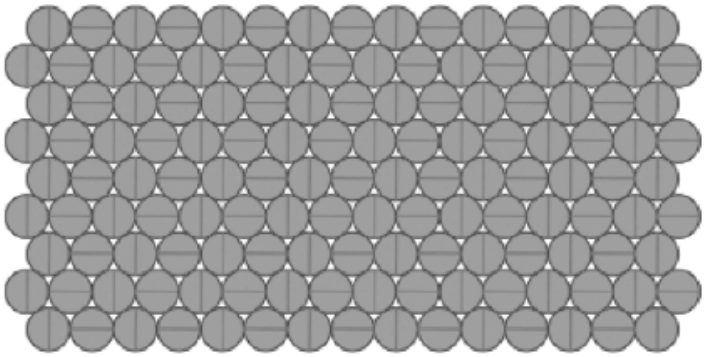

Figure 2.5: Schematic of the 350 μm polarizing grid layout. Vertical (V) or horizontal (H) lines show the orientations of the wires in the polarizing grid for each bolometer. The patterned polarizing grid is designed to have adjacent bolometers sample orthogonal polarization components. Therefore by scanning the telescope a measurement of a single Stokes Q or U parameter can be made in the time it takes for a source to move from one detector to an adjacent detector (≤ 0.5 s).

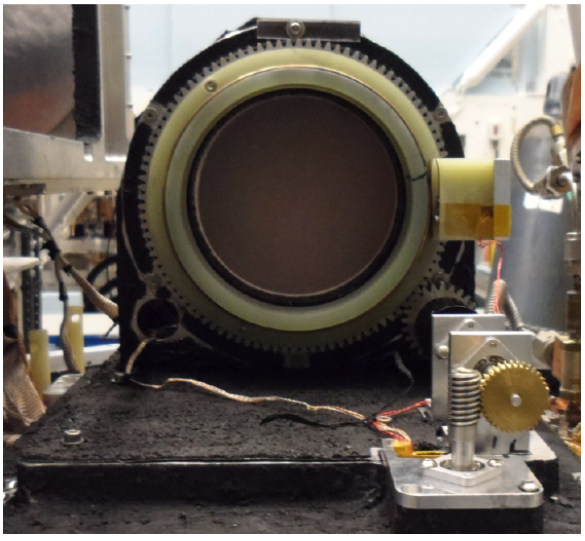

Figure 2.6: Picture of the BLASTPol sapphire achromatic HWP and rotator mechanism.

The use of a rotating HWP as a polarization modulator is a widespread technique at millimeter and submillimeter wavelengths (for example Hanany et al. (2005), Savini et al. (2006), Pisano et al. (2006) and Johnson et al. (2007)). The BLASTPol HWP is 10 cm in diameter and is constructed from 5 layers of sapphire, each 500μm in thickness. The layers are hot pressed together with a 6 μm layer of polyethylene, and an anti-reflection coating (made from metal mesh filter technology (Zhang et al. 2009)) is hot pressed to each surface of the HWP. Figure 2.7 shows the predicted transmissions and modulation efficiencies for the BLASTPol HWP as a function of frequency. They are based on data taken at room temperature, which has been used to estimate the 4 K performance of the HWP.

The rotator uses a pair of thin-section steel ball bearings housed in a stainless steel structure. It is driven by a gear train and G-10 shaft connected to a stepper motor outside the cryostat. A ferrofluidic vacuum seal is used for the drive shaft. Angle sensing in the cryostat is provided by a potentiometer element making light contact with phosphor bronze leaf springs and outside the cryostat by an incremental encoder connected to the motor. Both the rotator and potentiometer are based on a design used successfully by the SPARO telescope (Renbarger et al. 2004).

We operate the HWP in a stepped mode, rather than a continuously rotating mode, to avoid heating the cold stages of the cryostat. Rotating the HWP has a noticeable effect on the bolometer voltage levels. The top panel in Figure 2.8 shows the TOD of a 500 μm bolometer when the HWP is stepped by 22.5°. The HWP angular position is indicated in the middle panel by the HWP motor encoder readings. The large bolometer signal is likely due to changes in detector loading as the HWP rotates since transmission is not uniform across the surface of the HWP. Rotating the HWP also heats the 300 mK stage of the cryostat (bottom panel) likely due to vibrations of the rotator shaft and bearings. Thermal recovery from the HWP move, seen in the 300 mK strap temperature and the bolometer TOD, takes about one minute.

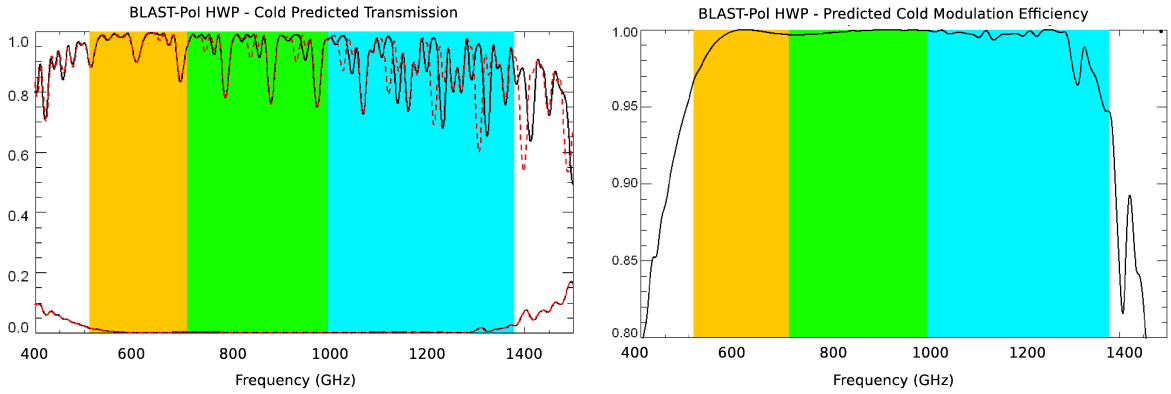

Figure 2.7:

Left: The predicted transmissions through the HWP as a function of frequency. The approximate extent of the BLAST band-passes is also indicated. *Solid Black Curve:* transmission between two parallel polarizers (i.e. Q=1 to Q=1) with the HWP axis at 0 deg (black line). *Red Dashed Curve:* transmission between two parallel polarizers Q=1 to Q=1 with the HWP axis at 90 deg (or equivalently Q=-1 to Q=-1 with the HWP axis at 0). Red and Black Lower Curve: transmission with the HWP axis at 0 deg between two perpendicular polarizers. *Right:* predicted modulation efficiency (as a function of frequency), obtained as $(T_{copol} - T_{xpol})/(T_{copol} + T_{xpol})$. Note that the y-axis scale ranges from 0.8 to 1.

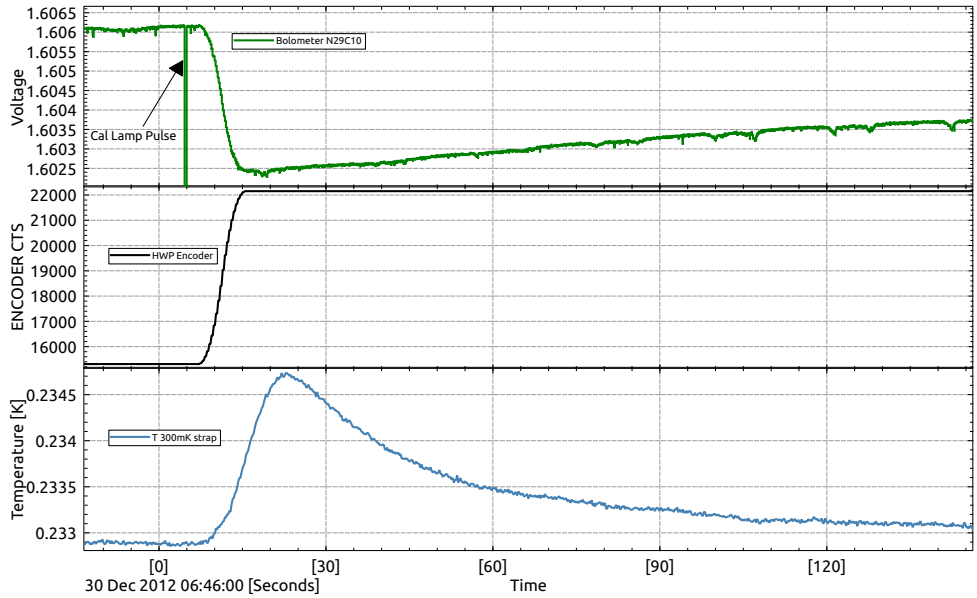

Figure 2.8: 500 μm bolometer response to a rotation of the HWP (HWP) by 22.5 degrees. *Top Panel:* 500μm bolometer N29C10. *Middle Panel:* HWP motor encoder readings showing the angular position of the HWP in time. *Lower Panel:* Temperature of the 300 mK strap, which is thermally coupled to the 300 mK stage of the cryostat. Note that just before the HWP was rotated the calibrator lamp was pulsed. The large change in the bolometer voltage when the HWP rotates is associated with loading changes due to non-uniformities in the HWP transmission. A longer timescale thermal recovery can be seen in both the 300 mK strap temperature and the bolometer timestream.

The HWP rotator is stepped between a sequence of four different positions corresponding to HWP angles Φ of 0°, 45°, 67.5° and 22.5°. This sequence allows Stokes Q and U to be measured with a single bolometer and avoids HWP rotations larger than 45°. The HWP is stepped to the next angle in the sequence after every raster scan of the target, typically every 15 minutes. In theory, measuring the polarization at these four HWP positions should be sufficient to reconstruct the I, Q and U Stokes parameters, even without the patterned polarizing grid. However the measurements at different waveplate angles take place at least 15 minutes apart, timescales much longer than the characteristic 1/f knee of the observations. Software controlling the HWP rotations is described in Section 2.7.4.

2.4.3 Preflight Polarimetry Strategy Tests

BLASTPol is the first submm polarimeter to attempt to reconstruct linear polarization using a patterned polarizing grid and a stepped HWP for additional modulation. Before construction of the polarimeter feasibility tests were run using BLAST 2006 observations of the calibrator VY CMa, which was mapped more than 20 times over the 11 day flight for a total of 6.7 hours. Total intensity maps were made of VY CMa with the optimized mapmaker almagest (Wiebe 2008) using different combinations of bolometers corresponding to BLASTPol horizontal (H) and vertical (V) polarizing grid orientations as shown in Figure 2.5 and also with different data time ranges. Figure 2.9a shows a map of VY CMa (the bright source at the center of the image) using all 500 μm bolometers and all data ranges. The maps were then differenced to test BLASTPol's polarization measurement strategy. The difference maps for a polarimeter with identical beam shapes for each detector and no 1/f noise should consist of white noise.

Several residual tests were run:

- **H bolometer maps - V bolometer maps** *Figure 2.9b:* This test is equivalent to

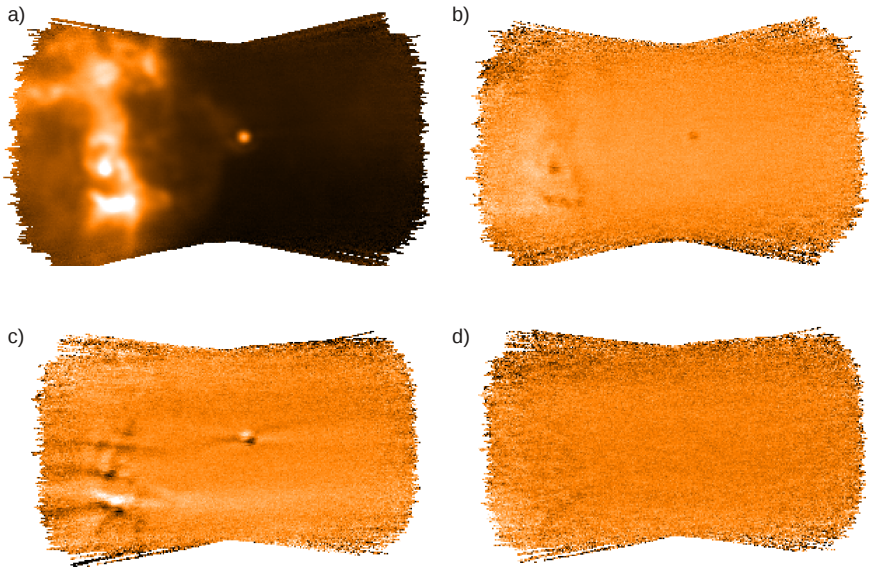

Figure 2.9: Results from pre-flight tests of the BLASTPol polarization reconstruction strategy using BLAST 2006 observations of the star VY CMa. *a)* A 500μm map of VY CMa using all bolometers and all available data. *b)* Residual signal from maps of VY CMa made with H bolometers - maps made with V bolometers. (See Figure 2.5). *c)* Residuals from maps of VY CMa made with even numbered scans - maps made with odd numbered scans. *d)* Difference between a map of H-V bolometers for even numbered scans - a map of H-V bolometers for odd numbered scans.

measuring a single linear polarization Stokes parameter (Q or U) of an unpolarized source using only a patterned polarizing grid with each adjacent bolometer measuring orthogonal polarization components and no HWP polarization modulation. Significant residuals of order several percent can be seen due to differences in the beam shape and responsivity of the 500 μm bolometers.

- **Odd numbered scan maps - Even numbered scan maps** *Figure 2.9c:* This test is equivalent to measuring a single linear polarization Stokes parameter (Q or U) with a polarimeter consisting of a grid that passes only one polarization component, with a HWP that rotates the polarization of the light by 90° after every scan. Significant residuals (of order several to $\sim$10 percent) are seen with streaking patterns characteristic of low frequency 1/f noise.

- **(H-V maps with even numbered scans) - (H-V maps with odd numbered scans)** *Figure 2.9d:* This test differences maps with both H and V bolometers and even and odd numbered scans and is equivalent to a polarimeter consisting of a polarizing grid which samples orthogonal polarizations components for each adjacent bolometer and a HWP that is stepped after every scan. Most of the polarization residuals from the previous simulations are not present.

These differencing tests show that both the patterned polarizing grid and HWP are necessary to reconstruct polarization: the patterned grid allows fast sampling of Stokes parameters, while the HWP stepping allows single bolometer measurements of the polarization and can reduce residuals due to differences in bolometer beam shapes.

2.5 Gondola

The BLASTPol gondola provides a pointed platform for the telescope and attaches to the balloon flight train. The gondola can generally be broken down into two parts:

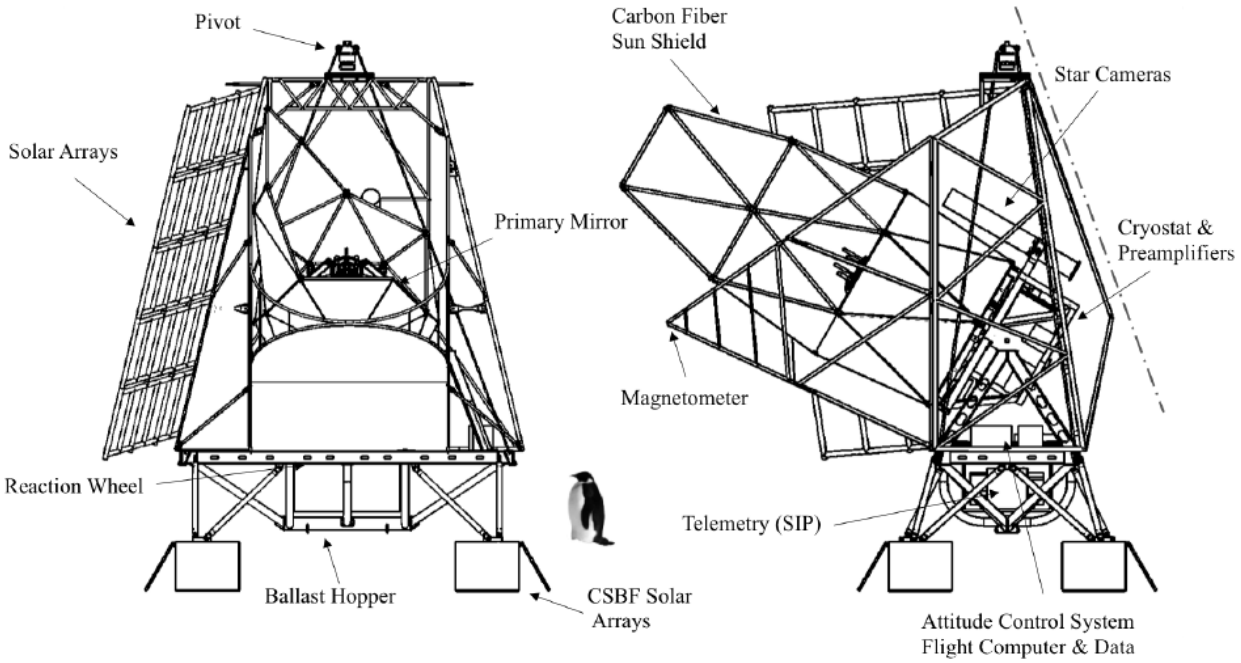

Figure 2.10: Front and side schematic drawings of the BLAST gondola. A 1-m tall Emperor penguin is shown for scale. The inner frame, which can be pointed in elevation, consists of the two star cameras, the telescope and its light baffle, the receiver cryostat, and associated electronics. The telescope baffles and sunshields have been updated for BLASTPol. Taken from Angilè (in press).

an outer frame, which points the telescope in azimuth and houses the power system, support electronics, motors and master flight computers, and an inner aluminum frame which points in elevation and houses the mirrors, cryostat, receiver, data acquisition system, and primary pointing sensors. Figure 2.10 shows a schematic layout of the BLAST gondola with several features labeled.

The inner frame is mounted to two pyramids which form an elevation axis. On the starboard side the inner frame is mounted to an elevation bearing and on the port side it is mounted to a direct drive rotary motor which is responsible for pointing the telescope in elevation.

Inner and outer frame sunshields were constructed to keep solar radiation off

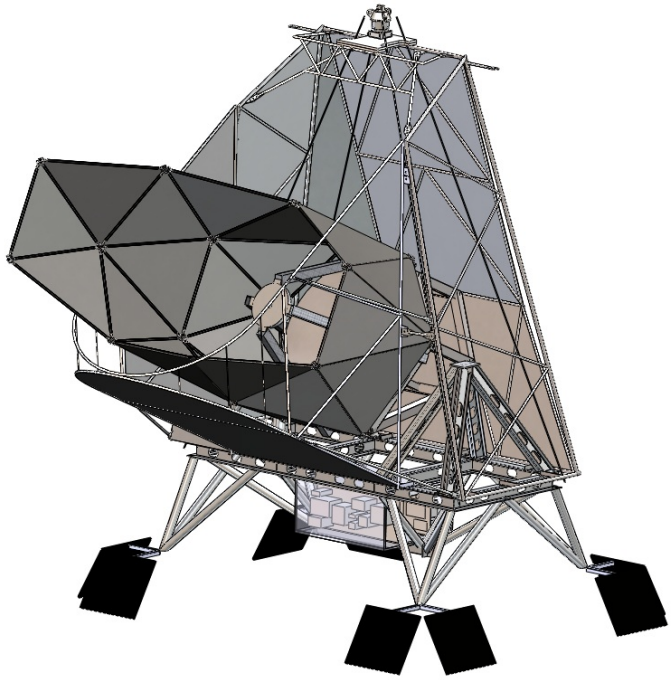

Figure 2.11: A drawing of the BLASTPol gondola showing the inner and outer frame gondola structures and sunshields, including the inner frame baffle which allows the telescope to point to an azimuth distance of $< 45^{\circ}$ from the Sun.

the primary and secondary mirrors. All Antarctic balloon flights take place during December to January when the Sun is located near the inner Galaxy. Many potential BLASTPol targets are located at high galactic longitudes (see Section 3.2.1 for a discussion of BLASTPol target selection), so a requirement for the shields is that the telescope is able to point in azimuth to within 45° of the sun, without sunlight incident on either the primary or secondary mirrors. Figure 2.11 shows the BLASTPol sunshields, which are constructed from aluminized mylar. The outer frame shields are mounted to an aluminum frame, while the inner frame shields are mounted to a 4 m long asymmetric carbon fiber frame. For more information on the BLASTPol shield design and thermal properties see Soler (2013). The sunshields allow the telescope to observe targets with $Az - Az_{\odot}$ ranging from 170° to 40°, where 0°would have the telescope pointing directly at the sun.

2.5.1 Electronics

Because of the long latency of sending commands to the telescope during flight (typically 20 seconds to 5 minutes) and the probability of intermittent communications blackouts, the gondola must be able to operate autonomously. The primary control is provided by a set of redundant master control computers (MCCs). Each computer runs an identical version of the flight control software, the *master control program* or *mcp*, which handles data acquisition and storage, pointing reconstruction, motor control, telemetry and housekeeping (Wiebe 2008). Because there is insufficient bandwidth in the telemetry downlink pathways to transmit the data[1], all data are stored on solid state hard drives connected to the flight computers. The hard drives must therefore be recovered after the flight.

Figure 2.12 shows the main components of the BLAST electronics systems. A

[1]The exception is during the first ∼12-24 hours after launch when the payload is still within sight of the balloon facility so that the line-of-sight (LOS) transmitters can be used.

detailed discussion of most components is given in Wiebe (2008). Here I give a brief overview of the major systems, with differences highlighted between the BLAST and BLASTPol architectures.

Flight Computers

Telescope operations are controlled by two identical redundant flight computers or *master control computers* (MCCs). The computers were replaced for BLASTPol (the old flight computers were destroyed when BLAST was dragged by the parachute in 2006) and are APOLLO boards, manufactured by the Eurotech company. Each flight computer runs an identical version of the flight control code *mcp*, or *master control program*. The computers read data from the Attitude Control System (ACS) and Data Acquisition System (DAS) over the BLASTBus and write data to solid state hard disks.

BLAST Cards

The BLAST Cards are a set of flexible electronic cards designed to both read and generate analog and digital signals. Each card consists of a single motherboard and can have up to three daughter cards. Types of daughter cards are:

- Analog input/output cards;
- Digital input/output cards;
- Thermometry cards;
- Digital to Analog (DAC) transmitters.

These cards are used in the Attitude Control System.

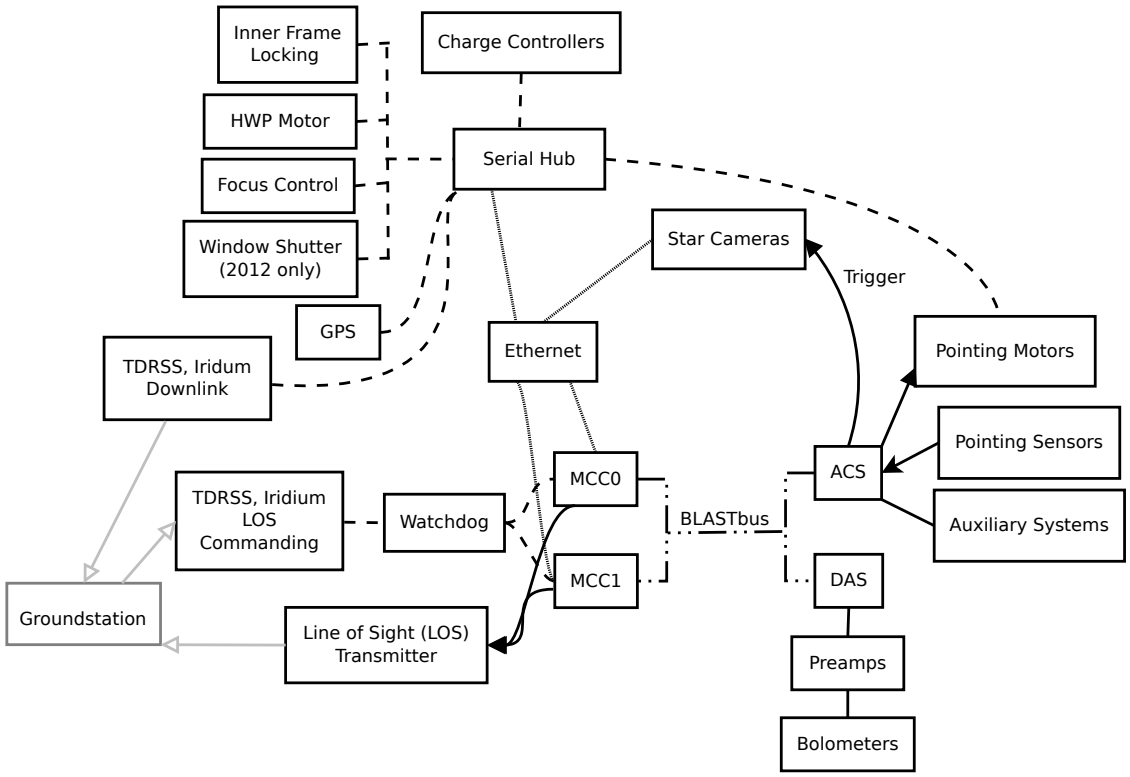

Figure 2.12: Schematic overview of the major electronic systems on BLASTPol. Dashed lines represent communication over serial, gray lines indicate radio transmission. All other forms of communication are annotated.

Attitude Control System (ACS)

The Attitude Control System (ACS) uses two BLAST Cards which in total contain two analog daughter cards, two digital cards and two thermometry cards. The ACS provides analog and digital sampling for all systems which are not managed by the DAS or directly by the MCCs, including gyroscope communications, star camera triggering, pointing sensors and power switching.

Data Acquisition System (DAS)

The Data Acquisition System or DAS reads out the detector signals, using 14 custom built analog-to-digital (ADC) cards plus an additional two cards for cryostat and bias generation and general housekeeping. The signals are then communicated to the flight computers over the BLASTBus (Wiebe 2008).

Watchdog Circuit

The watchdog circuit monitors the flight computers and will power cycle a computer if an error or loss of communication is detected. The circuit uses counters, one for each flight computer, and if the countdown reaches zero, the flight computer is power cycled. The computers can reset the counter by 'tickling' the watchdog, which consists of sending a logical signal over three parallel lines generated by an *mcp* subprocess. Thus if *mcp* crashes on one of the flight computers, the affected computer will be power cycled and control will be switched to the other flight computer. After power cycling the countdown circuit is inhibited for $\sim$5 minutes in order for the rebooted computer to have time to fully boot and restart *mcp*. The watchdog also ensures that only the computer in control of the telescope can write to the BLASTBus.

Serial Communications

Communication with motor controllers, charge controllers, the differential GPS, and over-the-horizon telemetry is routed through RS-232 serial communication. Most devices are connected through a Devicemaster 16 port RS-232 serial hub. The serial hub communicates with the flight computers via an Ethernet link.

Use of the serial hub has one major drawback. The *nslink* driver for the hub blocks communications from a computer that has recently rebooted. The blackout lasts for 5.5 minutes. Under normal circumstances, i.e. when both flight computers do not reboot at the same time this is not a problem, however if both computers reboot simultaneously there will be a $>$5 minute serial communication blackout. The serial lines which send commands to the flight computers are critical to flight operations so they are routed through the watchdog circuit instead of the RS-232 hub.

Stepper Motors

Several BLASTPol systems use AllMotion EZStep stepper motors:

- Inner frame locking mechanism;
- HWP rotator;
- Secondary Mirror Actuators, which are used to set the focus and tip-tilt of the secondary relative to the primary mirror;
- The protective shutter for the cryostat vacuum window, which was added for the 2012 flight.

These motors are controlled by a series of daisy-chained EZStep motor controllers and communicated with over RS-232 serial via the serial hub.

Telemetry and CSBF Electronics

During the course of the flight a subset of the data may be transmitted over the NASA telemetry pathways provided by NASA's Columbia Scientific Balloon Facility's Standard Instrument Package (SIP), which is part of the provided balloon electronics package. Over most of the flight the telescope is in communication with a ground station computer, where a subset of (compressed) data are sent to monitor the state of the telescope. BLASTPol has four downlink channels: high bandwidth line-of-sight (LOS) transmission, which is only available for the first ∼12-24 hours after launch, transmission over the TDRSS Network (with both an omni-directional antenna and a High-gain pointed antenna), and transmission over the Iridium Network. Commands can also be sent to the telescope via, LOS, TDRSS or Iridium to execute tasks or change parameters.

2.5.2 Pointing Sensors

In-flight pointing is measured to an accuracy of $\sim 1'$ by a number of fine and coarse pointing sensors. The primary pointing sensors consist of two optical star cameras mounted on the inner frame and aligned along the telescope axis and fiber-optic gyroscopes. The optical star cameras measure positions of stars on the sky and compare these positions to a star catalog, using the last known pointing solution as an initial guess. Gyroscopes are then used to integrate the pointing solution in-between star camera solutions. The star cameras can return a solution approximately every second, if stationary and pointed at a bright star field.

BLASTPol also uses a number of coarse pointing sensors. The goal for these sensors is to provide a rough pointing solution, accurate enough to be sure that the telescope is pointing at the correct field even if the star cameras cannot find solutions. Additionally the gyroscope output is known to have a non-stationary offset which

drifts on timescales of order half an hour. Coarse pointing sensors are used to calculate gyroscope offsets which are then subtracted from the gyroscope TOD.

BLASTPol has a variety of coarse pointing sensors, each of which can be vetoed or allowed to contribute to the pointing solution depending on the sensor performance:

- *Magnetometer:* The magnetometer measures the magnetic field of the Earth and then compares the field direction to a model to reconstruct the orientation of the gondola. Near the magnetic poles however the field lines are highly inclined so the accuracy is limited to a few degrees. To avoid magnetic fields from motor currents the magnetometer is mounted on the outer frame "chin" sunshields.

- *Omni-Sun Sensor:* This sensor consists of twelve photodiode sensors mounted radially which cover 360° in azimuth. Sensitivity to shadowing by cables or other structural components makes the sensor only useful over a limited azimuth range. The omni-sun sensor was only flown in 2010.

- *Pinhole Sun Sensors:* Pinhole Sun Sensors (PSS) use voltages generated by a photodiode array to reconstruct the azimuth and elevation of the sun. Individual PSS units cover a range of $\sim$40° in azimuth, but a number of units can be mounted in different locations to give an unobstructed view of the sky. The PSS units are small and have low power consumption and unlike the omni-sun sensor do not require a separate computer for processing.

- *Differential GPS:* A differential GPS (DGPS) consisting of at least three GPS units mounted a fixed distance apart can be used to reconstruct the orientation of the gondola. The accuracy of the azimuth reconstruction depends on the baseline between the antennas. BLASTPol flew a DGPS unit with a largest baseline of 3 meters in 2010. For the 2012 flight BLASTPol used data from a different DGPS unit which was part of the CSBF electronics package.

- *Roll Star Camera:* An additional star camera was mounted on the outer frame, with the goal of better constraining the roll pendulations of the telescope which are poorly constrained by the inner frame star cameras and gyroscopes.

- *Elevation Encoder:* The elevation motor has a built-in encoder. It offers high precision measurements of the angle between the inner and outer frame, however its accuracy as an elevation coarse sensor is limited by the fact that the entire gondola outer frame pendulates with an amplitude of a few arcminutes.

- *Inclinometers:* Liquid bubble inclinometers are mounted on the inner frame as a backup for the elevation encoder and on the bottom of the gondola directly below reaction wheel center as a measure of the tilt of the outer frame. The sensor measures the direction of acceleration, so it is not sensitive to motions due to the acceleration of the payload.

Post-flight pointing reconstruction uses only the gyroscopes and star cameras (Rex et al. 2006). The algorithm is based on a similar multiplicative extended Kalman filter technique (Markley 2003) used by WMAP (Harman 2005), which has been modified (Pittelkau 2001) to allow for the evaluation of the star camera and gyroscope alignment parameters. The offsets between the star cameras and the submm telescope are measured by repeated observations of pointing calibrators throughout the flight. Post flight absolute pointing accuracy using this system is typically $< 2''$, and random pointing errors were found to be $< 3''$ rms (Pascale et al. 2008; Marsden et al. 2008).

The performance of various pointing sensors and quality of the resulting pointing solution will be discussed in N. Gandilo's thesis.

2.5.3 Power Systems

BLASTPol consumed an average of 400 Watts of power during nominal operations in 2010 and 390 Watts in 2012. During large telescope slews the motors required extra

power of up to ∼150 Watts. Also during the first 12-24 hours while the telescope was within line-of-sight we used video and telemetry transmitters to communicate with the payload, which consume an extra ∼150 Watts.

BLASTPol flights take place during the Antarctic summer, which limits the battery charge capacity (and therefore mass) required as the sun is always above the horizon. Our solar panels were manufactured by SunCat Solar, LLC of Tucson, Arizona. The individual cells are A 300 mono crystalline silicon solar cells manufactured by Sunpower. Each cell is 12.5 by 12.5 cm in size with a thickness of 270 microns and can produce 6.83 Amps at a voltage of 0.38 V at peak power and an operating temperature of 100°C.

The individual cells are arranged into solar panel modules, with each module containing 30 cells connected in series, which can produce 79 Watts ($6.83\,A \times 30 \times 0.38\,V$). Bypass diodes are installed in parallel with every ten cells so that an electrical break down would only result in the loss of a third of the module power. The individual modules are connected in series in a "string" of three panels, which results in an open circuit voltage for each string of 34.56 V.

The entire solar array consists of six strings connected in parallel. The total power the array was designed to produce at normal sun illumination was 1147 Watts at a typical battery voltage of 28 Volts. Even if the sun was at an angle 60 degrees from the normal of the solar panels, the panels are designed to provide 574 Watts of power which is well over the typical power consumed by BLASTPol.

The panels were mounted on an aluminum frame with the panel normal angle ∼110° from the telescope beam in azimuth and ∼14° above horizontal in elevation. The sun elevation in late December in Antarctica ranges from ∼8-40°.

BLASTPol uses four Odyssey Extreme PC1200 sealed gel type lead-acid battery units. Each unit has a nominal voltage of 12 V, and a charge capacity of 40 Amp hours, which at BLASTPol's typical power consumption of 400W and battery voltage

of 28.0 V would last for ∼5.6 hours. Charging of the batteries is controlled by a TriStar MPPT Solar Controller manufactured by the Morning Star Corporation.

During the 2010 post-flight analysis the bolometer TOD showed anomalous features which correlated with motor current spikes, probably indicating that cryostat readout electronics were very sensitive to noise on the power lines (see Section 4.2.1). The receiver and cryostat were isolated by creating a second power system, with a separate charge controller which charged half the batteries and used two strings of solar panel modules. Three strings of solar panels were used to charge all other systems (including the flight computers, ACS and motors).

2.6 Motor Control

2.6.1 Overview

BLASTPol relies on three direct-drive brushless DC motors to point the telescope. An elevation drive points the inner frame housing the telescope, receiver, DAS and primary pointing sensors. The entire balloon gondola is then pointed in azimuth.

Because of conservation of angular momentum changing the velocity requires the azimuth motors to transfer angular momentum to and from various "sinks". The primary azimuth pointing motor is attached to a high moment of inertia reaction wheel, which allows control of angular momentum on short timescales (0.1 s to ∼15 s). Over longer timescales we use a motor attached to an active pivot connecting the gondola suspension cables to the balloon flight train. This pivot motor can be used to transfer angular momentum through the flight train into the balloon, which has a very large moment of inertia.

Motors use magnetic fields to generate a force which moves a rotating part (rotor) relative to the stationary part of the motor (stator). The force comes as a result of interacting magnetic fields in the rotor and stator. Different types of motors offer

different degrees of complexity and power consumption. For the BLASTPol pointing motors we use Brushless DC (BLDC) direct drive motors (DDR). Figure 2.13 shows a cartoon of a brushless DC motor setup. The rotor usually contains rare earth magnets, while the stator contains at least three coils of wire which generate a magnetic field when current is passed through them. The interaction of the rotor magnetic field and the time varying field from the motor windings causes the rotor to turn.

BLDC motors require a motor controller, a device to which battery power and a control signal are inputted. The controller outputs time phased AC currents to each of the stator coils. In order to generate the correct phases the controller also requires commutation feedback from a sensor measuring the angular position of the rotor with respect to the stator.

The motors used by BLASTPol are direct drive (DDR), which means the rotor is coupled directly to the load, not connected through a gear train or belt system. There are several advantages of using BLDC DDR motors:

- In non-DDR motors which use belts or gears, motor tuning is more difficult, with additional motor backlash and vibrations;
- Motors which use brushes require periodic replacements. Brushes also wear out more quickly in the low atmospheric pressure balloon environment ($\sim$0.005 atm), and more importantly are a cause of excess of electromagnetic interference from arcing due to the lower breakdown voltage of air at float altitudes.
- Gears require periodic lubrication and belts require tightening, while brushless DDR motors require almost no maintenance.

The properties of the three BLASTPol pointing motors, the reaction wheel, pivot and elevation drive, are summarized in Table 2.1.

The behavior of direct drive motors can be predicted largely by two constants: the torque constant k_T in units of Nm/Amps, which relates the current required to obtain

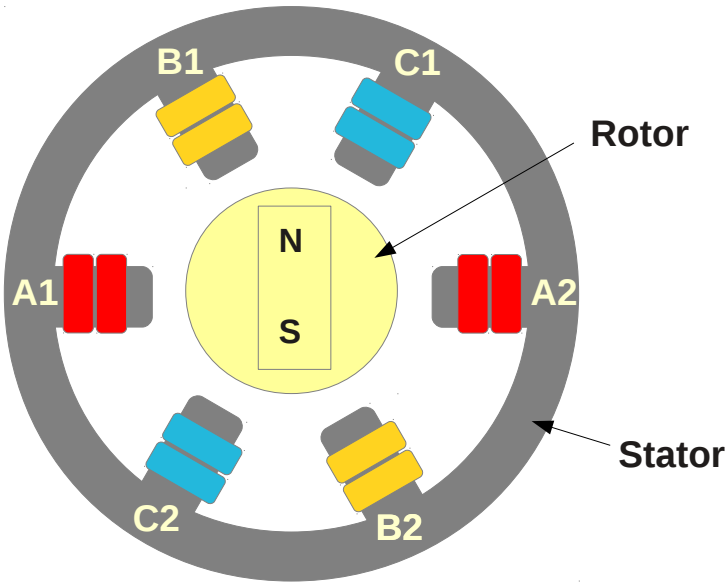

Figure 2.13: Cartoon showing the basic components of a brushless DC motor. The BLDC consists of a rotor which has a permanent magnet. The stator has a series of windings (in this case 3 pairs of windings), which produce a time varying magnetic field when an AC current is run through them. The current run to each of the winding pairs is out of phase generating a rotating magnetic field in the motor, which causes the rotor to turn. In order for the motor to rotate smoothly and efficiently the motor controller requires position feedback on the orientation of the rotor, to phase the winding currents appropriately.

Motor	Elevation	Reaction Wheel (2010)	Reaction Wheel (2012)	Pivot
Model number	C053A	D062M	D063M	K1782008Y1
Manufacturer	Kollmorgen	Kollmorgen	Kollmorgen	Bayside
Commutation Feedback	Sine Encoder	Sine Encoder	Sine Encoder	Resolver
Motor Controller (MC)	EtherCat	EtherCat	EtherCat	AMC Digiflex
Peak Torque (Nm)	53.7	33.5	64.4	81
Max. Continuous Torque (Nm)	20.9	9.8	17.7	30
Max. Continuous Current (A)	12.5	6.0	5.7	10.0
k_T (Nm/A)	2.30	2.30	4.42	3.18
k_V (V_{RMS}/kRPM)	139	139	268	192
R (Ω)	1.40	3.56	4.83	1.7

Table 2.1: Properties and relevant constants for the BLASTPol pointing motors.

a given torque (assuming zero motor velocity), and the voltage constant k_V (V/kRPM) which gives the back EMF generated by spinning the motor a certain number of revolutions per minute. The back EMF implies that there is a maximum speed ω_{max} at which the motor can rotate where the voltage supplied by the battery (V) is equal to the back EMF voltage:

$$\omega_{max} = \frac{V}{k_v}. \tag{2.1}$$

The requirement that our motors be able to provide torque means that in practice the motor systems are designed to operate at a fraction of ω_{max}. If a motor is rotating at a velocity ω, the corresponding back EMF voltage is $k_v\,\omega$. The maximum torque that the motor can supply is then:

$$\tau_{max} = \frac{V - k_v\,\omega}{R}\,k_T \tag{2.2}$$

where R is the motor winding resistance.

2.6.2 Commutation Feedback Sensors

In order for the brushless DC motors (BLDC) motors to phase the currents in the stator coils to optimize the rotation of the rotor the controller requires high resolution, low latency measurements of the rotor orientation. The commutation feedback sensors used by the BLASTPol pointing motors are:

- *Sine Encoders:* Sine encoders are incremental encoders (which record changes in position of the rotor relative to the stator), but instead of outputting square waves, they output two 90°out of phase voltage signals. Sine encoders therefore provide analog-encoded rotor position to the motor controller which can be used to reconstruct the motor position to extremely high precision. Both the elevation and reaction wheel motors use sine encoders.

- *Resolvers:* The pivot uses a Harowe Heavy Duty Brushless 21BRCX-601-H91/20 resolver with $16'$ accuracy (peak-to-peak). A resolver is a rotary electrical transformer which has both a rotor and stator. The stator has three windings: an exciter winding and two phase windings. Running an AC voltage through the stator exciter winding induces current in the two rotor windings, which in turn induces current in the stator phase windings. By monitoring the stator phase winding voltages the sine and cosine components of the angular orientation of the rotor can be reconstructed. A resolver measures the absolute angular position of the rotor.

2.6.3 Elevation Drive

The elevation of the inner frame is controlled by a C053A Kollmorgen Cartridge Direct Drive servo motor mounted on one side of the inner frame at the attachment point

to the outer frame. A free bearing provides the connection point between the inner and outer frames on the other side. The motor specifications are given in Table 2.1. The position feedback is provided by a Heidenhain Endat sine encoder, which is a sine encoder with added hardware to keep the position of the motor in memory even when the motor is not powered. The encoder has a resolution of 134,217,728 counts per revolution.

Before flight the center of mass of the inner frame is adjusted to be along the cross-elevation axis by attaching 4 to 6 lead bricks. As cryogens boil-off in-flight the center of mass of the inner frame changes. To compensate and avoid over-taxing the elevation drive, we have incorporated a balance system consisting of two hermetically sealed tanks of fluid: one mounted at the front bottom of the inner frame and the other at the top-back of the inner frame. As cryogens boil-off fluid is pumped from the bottom tank to the top tank keeping the inner frame more or less in balance. A high density saline solution (Dynalene HC-50), which has a freezing temperature below -50°C, is used as the pumped fluid.

During launch the release of the payload can result in rotational accelerations of the cable suspended gondola of several hundred $^\circ/s^2$. To prevent damage to the inner frame or elevation drive during launch accelerations, an elevation locking mechanism is used. The locking mechanism consists of a series of lock holes on the port side of the inner frame and a steel pin mounted on the outer frame pyramid and controlled by a stepper motor. Before launch the pin is moved into one of the lock holes, preventing the inner frame from moving. After launch a command is sent for the lock motor to retract the pin from the lock hole so that the elevation drive can move freely.

The range of inner frame elevation allowed is limited by the clearance of the inner frame baffle with respect to the outer frame sunshields and suspension cables. The lower limit is set by the elevation where the inner frame baffle contacts the ground shield or telescope "chin". In 2010 the lower elevation limit was 23.5°. For the

2012 flight modifications were made to the chin design in order to reduce the lower elevation limit to 19.5° so that Saturn could be observed. The upper elevation limit is set by where the inner frame baffle contacts the suspension cables. The upper limit was set to 55° for both the 2010 and 2012 flights.

2.6.4 Reaction Wheel

The reaction wheel consists of a 0.76-m radius disk made of 7.6 cm thick aluminum honeycomb, with forty-eight 0.9 kg brass disks mounted around the perimeter. Total mass of the reaction wheel is $\sim$100 kg, and the moment of inertia is $\sim$27 kg m^2. The reaction wheel is mounted at the azimuthal center of mass of the telescope, directly beneath the active pivot. By spinning the reaction wheel angular momentum can be transferred to and from the gondola, allowing precise control over the telescope azimuth velocity with minimal latency.

The original BLASTPol motor was a Kollmorgen Housed Direct Drive Motor D062M, which is a multi-pole hollow shaft motor that comes pre-assembled in a case with a cross-roller bearing. The D062M can provide a maximum continuous torque of 9.8 Nm or peak torque of 33.5 Nm for less than two seconds. Commutation feedback is provided by a high resolution sine encoder which comes pre-installed into the motor assembly and which offers 27 bit ($26''$) resolution. Before delivery from the manufacturer, the motor unit was opened and the bearing grease was replaced with low temperature grease.

After the motor failed during the 2010 flight (Section 3.2.7) the reaction wheel motor was replaced with a D063M motor. The D063M is a higher torque version of the D062M (see Table 2.1) and also uses a dual bearing system. In addition this time the low temperature grease was not requested. A Copley Controls Accelnet EtherCat Drive (AEP-090-36) was used to drive both the 2010 and 2012 motors. The drive can output a peak current of 36 A or a peak continuous current of 12 A.

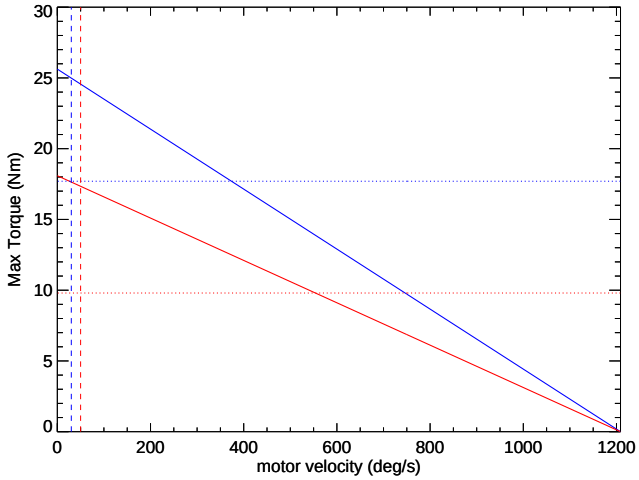

Figure 2.14: Maximum torque vs speed for the reaction wheel motor, made using equation 2.6.1 and motor properties given in Table 2.1. The 2012 motor (blue) can provide more torque than the 2010 motor (red). Dotted horizontal lines show the maximum continuous torque for the motor and the dashed vertical lines give the reaction wheel set point speed.

The 2012 motor has a higher back EMF constant (k_V) than the 2010 motor (Table 2.1) but also a higher torque constant (k_E). Figure 2.14 shows a Maximum Torque-Speed Curve for the reaction wheel calculated from Equation 2.6.1. In practice we limit the motor speed to below 400 °/s for safety reasons, indeed the motor control loops (Section 2.6.7) attempt to keep the reaction wheel spinning close to a commanded set point velocity (50 °/s in 2010 and 30 °/s in 2012).

A saturation time t_{sat}, or the amount of time that the motor can be run at the continuous torque limit (τ_C) before it reaches a maximum velocity, can be also be calculated:

$$t_{sat} = \frac{\omega_{max}}{\alpha_{max}} \frac{I_{RW}\omega_{max}}{\tau_C}, \tag{2.3}$$

where I_{RW} is the moment of inertia of the reaction wheel. Using ω_{max} =400 °/s, and $I_{RW} = 27\,\mathrm{kg\,m^2}$ the saturation time for the reaction wheel motor was 19.2 s in 2010 and

10.6 s in 2012. Torque on longer timescales must be provided by the active pivot motor.

2.6.5 Pivot Motor

BLASTPol is a cable suspended gondola. At the interface between the gondola suspension cables and the balloon flight train is an active pivot with an integrated motor. The active pivot provides many important functions:

- It allows the gondola to rotate relative to the balloon orientation without saturating the reaction wheel.
- Over short timescales it can provide torque by torquing against the flight train which can be modeled as a weak spring (see below).
- Over long scales the pivot can be used to transfer angular momentum to the balloon, which because of its volume ($1.1 \times 10^6\,\mathrm{m}^3$) has a very high moment of inertia.

Figure 2.15 (left panel) shows a picture of BLASTPol just after launch in 2012. The balloon, whose volume is less than 1% of the inflated volume at float altitudes, connects to a parachute (red). The parachute connects through lifting straps to a steel cable flight ladder, which connects to the BLASTPol pivot.

The balloon flight train system can be modeled as a series of harmonic oscillators. By applying torque τ to the bottom of the flight ladder, the pivot can cause an angular rotation of θ relative to the balloon:

$$\tau = -\kappa_{eff}(\theta)\,\theta. \tag{2.4}$$

κ_{eff} is the effective torsional spring constant of the flight train and parachute, which can be described as a series spring constants:

$$\kappa_{eff}^{-1} = \kappa_1^{-1} + \kappa_2^{-1} + \ldots. \tag{2.5}$$

Note that the weakest spring will dominate the effective spring constant.

Here we model the flight train spring constant as shown in Figure 2.15: with the two dominant terms coming from the flight ladder κ_1 and parachute κ_2. The parachute is used to reduce the speed of the descent after balloon termination, while the flight ladder provides the connection to the science payload (in our case at the pivot) and also decreases the solid angle of the balloon as viewed from the BLAST telescope, allowing access to science targets at high elevations.

The spring constant can be determined by considering the energy of the system. We start by considering just the spring constant of the flight ladder. Rotating the pivot causes an angular displacement of $\Delta\theta$ from the equilibrium angle of the flight ladder and the height of the ladder is correspondingly reduced by:

$$\Delta h \;=\; \sqrt{l^2 \;-\; R^2\theta^2} \;-\; l \;\approxeq\; -\frac{R^2\theta^2}{2l^2}, \tag{2.6}$$

where the right side of the equation is only valid when $\theta R \;<<\; l$. We can generalize this relation for a displacement from any angle θ,

$$\Delta h \;=\; \sqrt{l^2 \;-\; R^2\left(\theta \;+\; \Delta\theta\right)^2} \;-\; \sqrt{l^2 \;-\; R^2\theta^2}. \tag{2.7}$$

Then since

$$mg\Delta h \;= \tau\Delta\theta, \tag{2.8}$$

we can write

$$\tau\left(\theta\right) \;\simeq\; mgl\frac{\left(\sqrt{1 \;-\; \frac{R^2\left(\theta \;+\; \Delta\theta\right)^2}{l^2}} - \sqrt{1 \;-\; \frac{R^2\theta^2}{l^2}}\right)}{\Delta\theta} \tag{2.9}$$

which if both θR and $\left(\theta + \Delta\theta\right) R$ are $<< l$ can be simplified to

$$\tau\left(\theta\right) \;=\; -\frac{mgR^2}{2l}\frac{\left(\left(\theta \;+\; \Delta\theta\right)^2 \;-\; \theta^2\right)}{\Delta\theta}. \tag{2.10}$$

So in the limit as $\Delta\theta$ goes to zero equation 2.9 becomes:

$$\tau\left(\theta\right) \;=\; -\frac{mgR^2}{l}\theta, \tag{2.11}$$

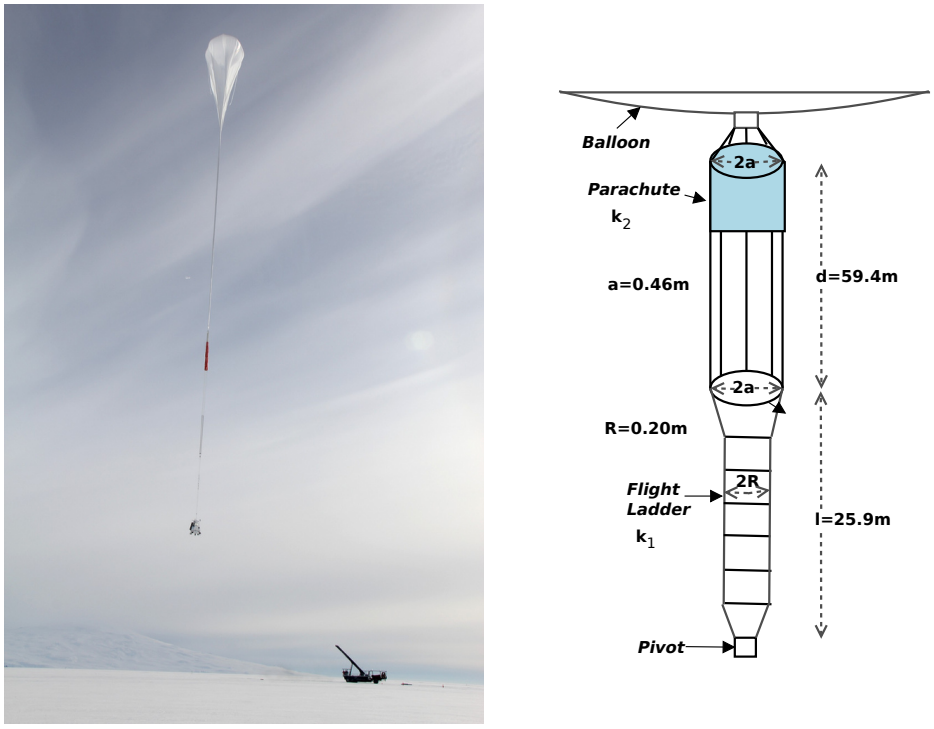

Figure 2.15: *Left:* picture of BLASTPol just after launch in 2012. The balloon, whose volume is less than 1% of the inflated volume at float altitudes, connects to a parachute (red). The parachute connects through lifting straps to a steel cable flight ladder, which connects to the BLASTPol pivot. *Right:* Cartoon of the model used to estimate the flight train dynamics. Here the flight train spring constant is modeled as the combination of the flight ladder κ_1 spring constant and the spring constant of the parachute κ_2. The length of the flight ladder is 25.9 m, and the two steel cables are kept 40 cm apart by metal rungs. The length of the parachute is 59.4 m, while the radius of the parachute support rings a =0.46 m (Davison, V., private communication).

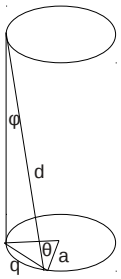

Figure 2.16: *Right:* Cartoon showing the geometry of rotating the bottom parachute ring by an angle θ relative to the top parachute ring. The change in height from this rotation is $\Delta h = \sqrt{d^2 - q^2} - d$.

so the spring constant κ_1 as defined in equation 2.4 is then

$$\kappa_1 = \frac{mgR^2}{l}, \tag{2.12}$$

which for a 2200 kg telescope, a cable ladder separation of $2R = 0.406$m and a flight train length l = 25.9 m gives a spring constant of 34 Nm/rad or 0.6 Nm/$^\circ$.

Calculating the spring constant of the parachute κ_2 is complicated by the fact that the parachute lines are not constrained to be kept apart by a certain distance, so the equivalent for R in Equation 2.6 is a function of θ. Note that if $\theta > 180^\circ$ the parachute lines cross meaning the effective spring constant goes to zero.

Figure 2.16 shows the geometry. Here:

$$h = \sqrt{d^2 - q^2} = d\,cos(\phi) \approxeq d\left(1 - \frac{1}{2}\left(\frac{q}{d}\right)^2\right). \tag{2.13}$$

But from the geometry of the parachute q can be written as a function of a and *theta*:

$$q = 2a\,sin\left(\frac{\theta}{2}\right), \tag{2.14}$$

so

$$\Delta h = h - d = -\frac{2a^2}{d}\,sin^2\frac{\theta}{2}. \tag{2.15}$$

Generalizing to a rotation of the bottom of the parachute from θ to $\theta + \Delta\theta$ we get:

$$\Delta h = -\frac{2a^2}{d}\left(sin^2\frac{\theta}{2} - sin^2\frac{\theta + \Delta\theta}{2}\right). \tag{2.16}$$

The second term can be Taylor expanded about θ:

$$sin^2\frac{\theta + \Delta\theta}{2} \approx sin^2\frac{\theta}{2} + 2\sin\frac{\theta}{2}\cos\frac{\theta}{2}\frac{\Delta\theta}{2} = sin^2\frac{\theta}{2} + \frac{1}{2}sin\theta\,\Delta\theta, \tag{2.17}$$

and Equation 2.16 can be rewritten as:

$$\Delta h = -\frac{a^2}{d}sin\theta\,\Delta\theta. \tag{2.18}$$

A similar analysis to the derivation of κ_1 gives

$$\kappa_2 = \frac{mga^2 f(\theta)}{d}, \tag{2.19}$$

where

$$f(\theta) = \frac{\sin\theta}{\theta}. \tag{2.20}$$

Combining equations 2.5, 2.12 and 2.19 gives:

$$\kappa_{eff} = mg\left(\frac{l}{R^2} + \frac{d}{a^2 f(\theta)}\right)^{-1} \tag{2.21}$$

The predicted spring constants are shown in Figure 2.17. For small or moderate displacements from the equilibrium point ($\theta < 100°$) the flight ladder spring constant dominates Equation 2.21 and the spring constant is relatively flat. As the separation between the parachute straps decreases the spring constant of the parachute decreases. Eventually the parachute spring constant starts to dominate Equation 2.21.

At the end of the BLASTPol 2012 flight a measurement was made to estimate the balloon flight train spring constant. The telescope was made to come to a rest then the azimuth motors were disabled and the reaction wheel motor was powered off. The motor control gains were set so that the term proportional to the reaction

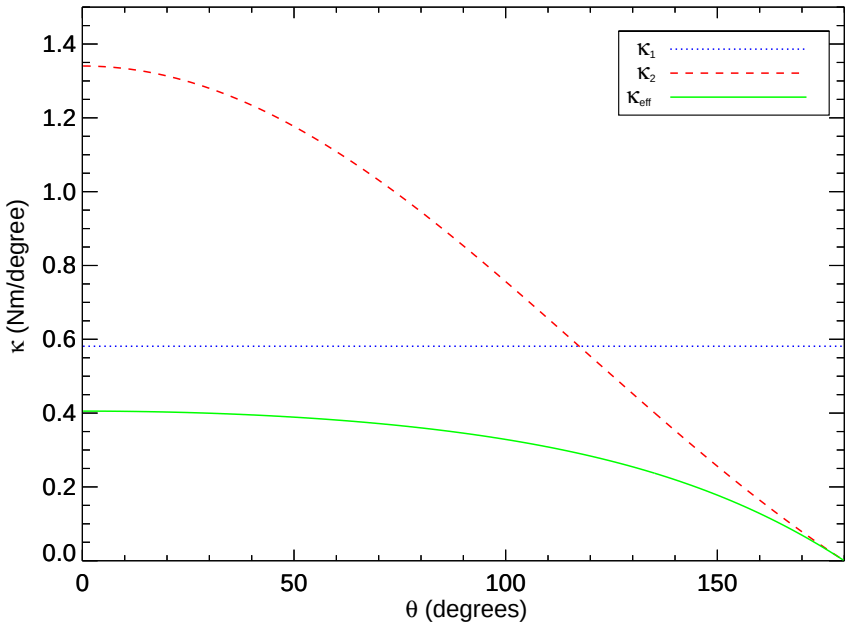

Figure 2.17: Predicted spring constants for the BLASTPol flight train, based on Equations 2.12, 2.19 and 2.21. At moderate displacements from the equilibrium point the effective spring constant κ_{eff} is dominated by the flight ladder spring constant (κ_1) and is relatively flat. After displacements of θ>100°, κ_{eff} drops as the parachute flight train spring constant (κ_2) starts to dominate Equation 2.21.

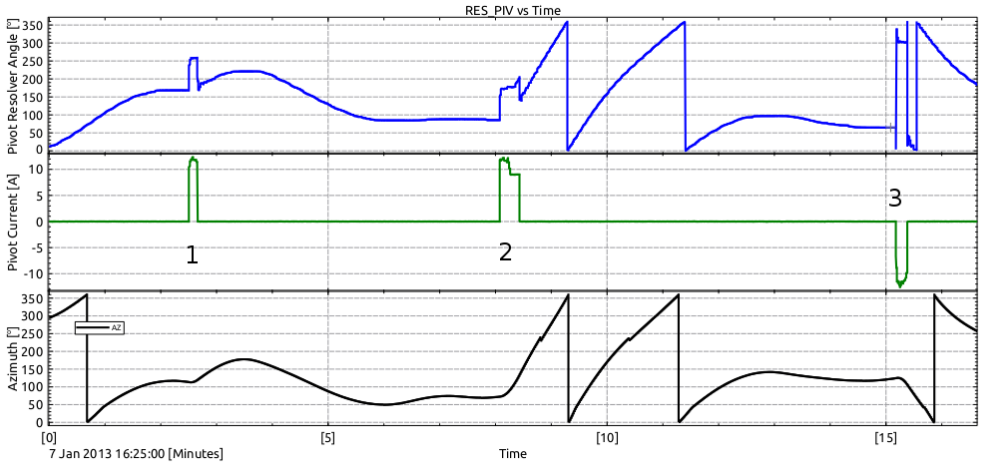

Figure 2.18: Measurements made of the pivot flight train spring constant. *Top:* Pivot resolver angle as a function of time. *Middle:* Pivot motor current with the three current spikes used to measure the spring constant labeled. *Bottom:* Azimuth of the gondola as a function of time.

wheel velocity error was maximized, and the reaction wheel velocity set point was at a maximum. When azimuth pointing was re-enabled the control software requested the maximum possible motor current from the pivot controller.

Figure 2.18 shows the response of the pivot system to several of these tests. When maximum current was applied to the motor the pivot applied a corresponding torque that would twist up the balloon flight train, as measured by the pivot resolver. A estimate for the average spring constant can be made using

$$\kappa_{meas} = \tau/\Delta\theta = \Delta I_{Piv} k_T/\Delta\theta \tag{2.22}$$

where ΔI_{Piv} is the pivot current needed to twist the flight train up by $\Delta\theta$ degrees and k_T = 3.2 Nm/A is the torque constant for the pivot motor. Table 2.2 shows the measured values for each of the three pivot current spikes. The values are in good agreement with those predicted by Equation 2.21 as shown in Figure 2.17.

As a final note Table 2.2 also shows that even when maximum current was applied to the pivot motor the bottom of the flight train still only rotated by ∼90-120°.

Measurement	1	2	3
ΔI_{Piv} (A)	11.8	11.8	-11.7
$\Delta\theta_{Piv}$ ($^\circ$)	90	87	-122
κ (Nm/$^\circ$)	0.42	0.43	0.31

Table 2.2: Measurements of the BLASTPol spring constant κ during the 2012 BLASTPol flight using the formula $\kappa = \Delta I_{Piv}\, k \Delta\theta_{Piv}$. For the pivot motor the torque constant k is 3.2 Nm/A. The measurement numbers refer to different instances when the pivot current was turned to maximum as shown in Figure 2.18.

This is important because if $\Delta\theta$ had been 180°or higher we could have crossed the parachute straps which would have resulted in the spring constant going to zero. As a consequence the pivot would no longer be able to provide torque and the reaction wheel motor would quickly saturate.

2.6.6 Motor Controllers

Two different types of motor controllers were used. For the elevation and reaction wheel drives Accelnet Ethercat (AEP-090-36) drives manufactured by Copley Controls were used. The pivot motor controller is a DPRALTR-020B080 controller from Advanced Motion Controls which can incorporate resolver feedback.

The controllers were commanded by sending an analog voltage signal V_{in} to the controller. The controller was programmed to produce an output current proportional to this input voltage:

$$I_{out} = C\, V_{in} \tag{2.23}$$

The input voltage was produced by a digital to analog converter mounted inside the controller electronics box, powered by a DCDC for greater electronic isolation. The digital signals were generated by DAC transmitter daughter cards in the Attitude

Control System (ACS) and carried to the controller box over a special DAC cable.

The flight computers also communicate with the controllers over isolated RS-232 serial lines. Serial communications are used to read information from the controllers such as motor position, velocity, output current, and controller status fields. The most crucial of these fields are the reaction wheel velocity which is used as an input to the pivot control loop (Section 2.6.7) and the elevation encoder which is used as a coarse elevation sensor (Section 2.5.2).

2.6.7 Control Software

Orientation of the telescope is controlled separately in azimuth (using the reaction wheel (Section 2.6.4) pivot (Section 2.6.5) motors), and elevation (using the elevation drive as described in Section 2.6.3). The motor control software can be broken down into three subsystems:

- *Velocity Computation:* Run as part of the main thread 100.16Hz control loop in *mcp*, the master control program (Wiebe 2008). This code takes as inputs the current pointing solution and scanning strategy and returns requested azimuth and elevation telescope velocities.

- *Current Request Calculation:* Compares requested telescope velocities to the velocity measured by the gyroscopes and then calculates current requests which are sent to the motor controllers.

- *Motor Communications:* Runs in a separate thread from the main *mcp* loop and handles serial communication between the motor controllers and *mcp*.

The motor control code has two modes: position mode and velocity mode. Position mode attempts to point the telescope at a location on the sky:

$$\omega_{req,az} = \begin{cases} -g_{az\,pt}\sqrt{|az - az_{dest}|} & \text{if } az < az_{dest} \\ g_{az\,pt}\sqrt{|az - az_{dest}|} & \text{if } az \geq az_{dest} \end{cases} \tag{2.24}$$

where $g_{az\,pt}$, is the azimuth pointing gain, one of a series of gains terms which can be commanded in flight to adjust and optimize pointing performance. A similar equation is used to calculate $\omega_{req,el}$.

The majority of the flight is spent making raster maps and therefore the telescope mostly operates in velocity mode. Scan control software (see Section 2.7.1) is used to calculate the desired telescope velocity.

Once the requested velocity is calculated a velocity error term is then computed:

$$\Delta\omega_{az} \;=\; \omega_{az} - \omega_{req,az} \tag{2.25}$$

which is just the difference between the requested velocity and the actual telescope velocity. Equation 2.25 can be written in terms of the angular roll and yaw velocities (v_{roll} andv_{yaw}) measured by the gyroscopes as

$$\Delta\omega_{az} \;=\; (v_{roll}\sin(el)\, v_{yaw}\cos(el)) - \omega_{req,az}. \tag{2.26}$$

Then the requested reaction wheel motor current $I_{az\,req}$ is calculated:

$$I_{az\,req} \;=\; g_{p\,az}\,\Delta\omega_{az} \;+\; g_{p\,az}\,g_{i\,az}\int_{t-5}^{t}\Delta\omega_{az}. \tag{2.27}$$

Here, $g_{p\,az}$ is the proportional gain for azimuth control and $g_{i\,az}$ is the integral gain. The proportional gain provides most of the current, but if there are dissipative forces acting on the system (e.g. motor friction, winds pushing on the gondola) the integral term will provide extra torque.

Equivalent equations are used to calculate the elevation current:

$$I_{el\,req} \;=\; g_{p\,el}\,\Delta\omega_{el} \;+\; g_{p\,el}\,g_{i\,el}\int_{t-5}^{t}\Delta\omega_{el}. \tag{2.28}$$

The elevation and reaction wheel motors are responsible for providing pointing control on short timescales, so calculations of equations 2.27 and 2.28 are done on the DSPs in the attitude control system (ACS), in a kilohertz loop.

The pivot motor control is slightly different than the reaction wheel or elevation drive. The primary task of the pivot motor is to keep the reaction wheel velocity near the requested set point $\omega_{rw\circ}$. This is to keep the RW motor speed from passing through zero velocity, where it would have to overcome static friction.

The pivot control equation is:

$$I_{piv\,req} = -g_{rw\,piv}\,\Delta\omega_{rw} + g_{p\,piv}\,\Delta\omega_{az} + I_{fric} \tag{2.29}$$

where $\Delta\omega_{rw} = \omega_{rw} - \omega_{rw\circ}$ is the difference between the actual reaction wheel velocity and the set point velocity, so the $g_{rw\,piv}$ term keeps the reaction wheel speed near the set point. The $g_{p\,piv}$ term is proportional to $\Delta\omega_{az}$ the telescope azimuth velocity error, and can be used to have the pivot motor also provide torque to drive the gondola azimuth scans. Note that in this equation there is no integral term. Instead I_{fric} is used to provide extra torque to overcome friction, where I_{fric} is a box car average over 10 seconds of $f(I_{piv})$ and $f(I_{piv})$ is defined as:

$$f\left(I_{piv}\right) = \begin{cases} +I_{fric\,off} & \text{if } I > 0.03A \\ -I_{fric\,off} & \text{if } I < -0.03A \\ 0 & \text{otherwise .} \end{cases} \tag{2.30}$$

$I_{fric\,off}$ is a commandable parameter usually set to 0.3 A.

2.7 Scanning Strategy

BLASTPol is a mapping experiment and operates in a different mode to many previous ground based polarimeters such SPARO (Dotson et al. 1998) and SCUPOL (Greaves et al. 2003), which chops the telescope pointing between the science target and a reference position that is assumed to have $I = Q = U = 0$.

Large low-frequency so called $1/f$ noise caused by drifts in detector gains, requires that the detector TOD be high-pass filtered. For BLASTPol 2010, we used a high-pass

filter with a cutoff frequency of 50 mHz, meaning that power on timescales greater than 20 seconds is attenuated. At a typical scan speed of 0.05 °/s this corresponds to a size scale of 1.0 degrees, which is the typical width of a BLASTPol map.

The BLASTPol scanning strategy is designed to visit each point on the sky many times, with different bolometers and at different parallactic angles. Making a map with good uniformity of coverage is also crucial. Ideally we would like to observe every pixel in our map multiple times, with every detector in our array at each of the four different HWP positions. In reality, errors in our in-flight pointing and the large size of many of our maps make this impossible.

2.7.1 Mapping Strategy Overview

As described in Section 2.6.7 the motor control software in the master control program (*mcp*) responds to azimuth and elevation velocity requests, which then get translated into motor current requests through the control loops.

The function of the scanning control subroutines in *mcp* is to request appropriate velocities based on the current altitude, azimuth and velocities of the telescope, and properties of the requested scan pattern.

In conventional scans, used for most science maps, the primary scan direction is in azimuth. This is because changes in elevation are known to cause thermal drifts in the bolometer TOD, possibly due to sloshing of cryogens during elevation moves or observation through an elevation dependent air mass. The telescope scans in azimuth while drifting at a constant speed in elevation. The goal is for the telescope elevation to have drifted by δel by the time it has completed one azimuth crossing, where δel is the elevation step size commanded for the scan. *mcp* calculates an appropriate elevation drift speed before each azimuth crossing.

There are three main types of azimuth based scans which trace different shapes on the celestial sphere:

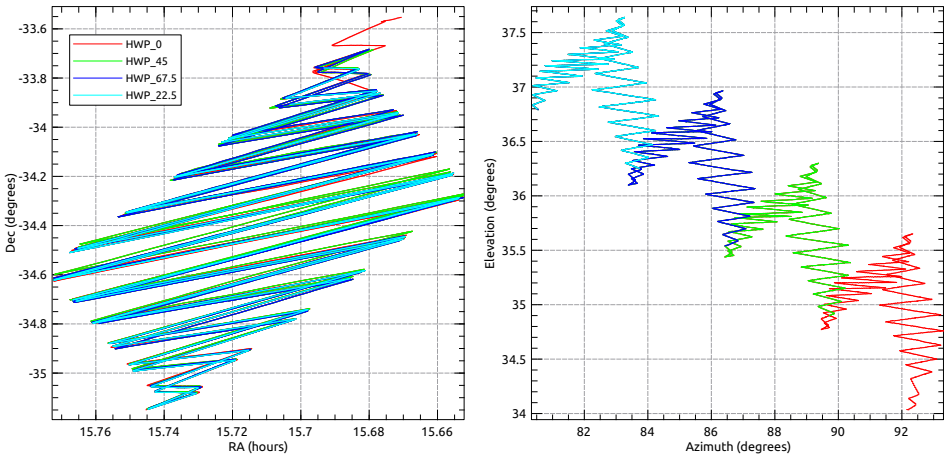

Figure 2.19: Trajectory for a complete scan of the Lupus I quad in right ascension/declination (left) and azimuth/elevation (right). Line colours correspond to the HWP position during each raster. The telescope scan parameters are set so that a single up and down raster takes ∼15 minutes. This way a full *scan* or rasters at all four HWP angles can be completed in ∼1 hour, and trajectories follow more or less the same path on the sky (minimal sky rotation).

- *box:* scans a rectangular area in azimuth-elevation about a center defined in right ascension and declination. The corners of the box will rotate as the parallactic angle of the source changes;
- *quad:* scans a quadrilateral defined by the coordinates of four corners in right ascension and declination;
- *cap:* scans a circular region about a defined center.

Figure 2.19 shows an example scan trajectory for the central bolometer of the Lupus I quad region observed in the 2012 BLASTPol flight, in both RA/Dec (left) and azimuth/elevation (right). The different colours in the figure show the scan trajectory for different HWP angles.

When referring to the data taken it is convenient to define some terminology:

- *Raster:* Corresponds to a single up and down scan at one HWP position. A typical raster takes ∼15 minutes.
- *Scan:* A complete scan of a target consists of four consecutive rasters on a target which cover all four HWP angles. A scan consists of ∼1 hour of data.
- *Observation:* An observation is a set of consecutive scans on one target.

2.7.2 Scanning Parameters

The coverage for an individual up and down raster is set by the scanning velocity, map size and elevation step size.

The azimuth scanning velocity is limited by the sampling rate of the detector readout and the size of the telescope beam. Requiring n samples of the beam FWHM per source crossing limits the angular speed to:

$$\omega < \frac{FWHM\, f}{n}, \tag{2.31}$$

where f is the sampling frequency of 100.16 Hz. For the 250 μm array the diffraction limited beam FWHM is $\sim 30''$. So requiring 3 samples per beam limits the telescope to an angular velocity of less than $0.28^\circ/s$.

The other limiting factor on the BLASTPol azimuth speed is the star cameras. In order to reconstruct pointing post-flight the star cameras must be able to detect and centroid stars. Scanning in azimuth during a star camera exposure causes smearing of the star's point spread function in the scanning direction. To compensate the star cameras have a shorter exposure (60-80ms) during azimuth scans than at azimuth turnarounds. Still at speeds greater than $\sim 0.1^\circ$/s, smearing of the stars usually means that stars are only identified at azimuth scan turnarounds.

The regions mapped by BLASTPol are typically of order a degree^2, small compared to the map sizes made by BLAST (Wiebe 2008). Ideally, the azimuth scan speed is kept

small to 0.05-0.1 $^\circ$/s, so that less time is spent turning around outside of the target area.

For BLASTPol the goal is to complete a raster in 15 minutes. This way a full scan with rasters at all four HWP positions can be completed in an hour. Hour long scans are useful for scheduling observations, but also the requirement of covering all four halfwave plate positions in an hour means that the telescope scans more or less the same trajectory at each HWP position (Figure 2.19).

Limits also need to be placed on the elevation step size δ_{el}, which needs to be large enough that a single up and down raster scan can be completed within a reasonable amount of time but sufficiently small that the array fully covers the target area in a single raster. The field of view of the telescope is $13.5' \times 6.5'$ where the short direction is nearly parallel to elevation. That means that the maximum elevation step size should be $6.5'/2 \sim 3'$.

2.7.3 Dithering

Ideally BLASTPol would be able to cross every point in the map multiple times with every detector at all four HWP angles in a single scan. However full coverage would require an elevation step size of just $10''$(approximately $1/3$ the 250μm FWHM). Observations need to be scheduled in hour long scans, so for most scan regions it is not possible to have an elevation step size that small at reasonable scan speeds. The solution is to dither the center of the scan in elevation from δel to $-\delta el$. The dither step size can then be set to $10''$ or whatever size will give the most uniform coverage in the time available.

Figure 2.20 shows an example scan of the Lupus I map region observed in the 2012 BLASTPol flight. The right panel shows the scan pattern after 2 two scans (green and blue). In this case the elevation of the center of the scan was increased by $10''$ after the first scan. The left panel shows the scan trajectory traces after eight such dither steps.

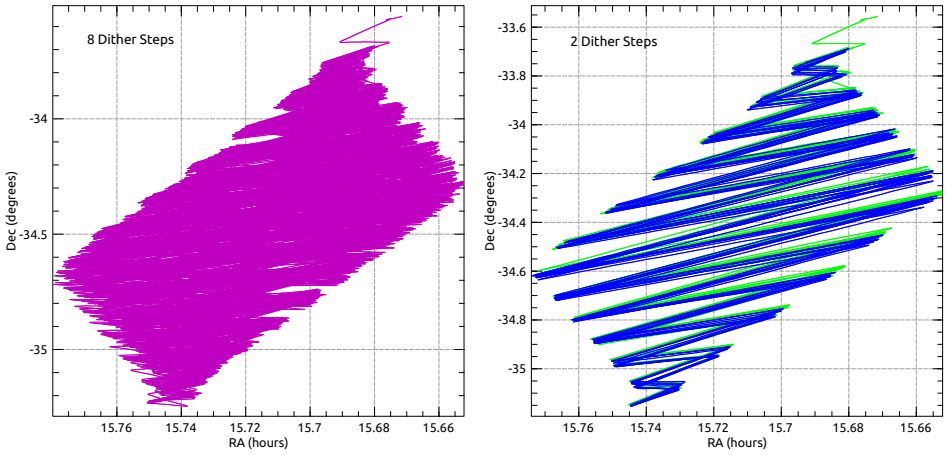

Figure 2.20: Example scans of Lupus I showing the improved map coverage for a single detector due to scan dithering. *Right:* the scan pattern after 2 two scans (green and blue). In this case the elevation of the center of the scan was increased by 10″ after the first scan. *Left:* the scan trajectory traced after 8 dither steps.

2.7.4 HWP Rotation

An additional task of the scanning software in *mcp* is to trigger the HWP to rotate to a new position at the end of every raster. The rotation is triggered at the turnaround before the last azimuth crossing at the bottom of the raster. A flag to step the HWP is set and read by the HWP control thread of *mcp*.

The HWP has two sensors which are used to determine position: a potentiometer on the HWP which is kept at cryogenic temperatures and an encoder which is mounted on the stepper motor (outside the cryostat). The encoder is high resolution (324 encoder steps per 1° of HWP rotation), however the encoder is incremental so if the motor were power cycled we would have no knowledge of its position.

The potentiometer simply gives a voltage as a function of wave plate orientation, so it gives an absolute measurement HWP angle. However defects on the potentiometer contacts can lead to errors in the derived angle of the HWP. Four waveplate angles

were chosen separated by 22.5° where the potentiometer readings were repeatable and accurate.

When a HWP step is triggered, the potentiometer orientation is measured. The control software uses the potentiometer reading to calculate the current HWP orientation, calculates the number of motor steps required to reach the next target HWP angle and executes the move. If the potentiometer gets a bad reading (which typically happens a few times a flight) it will move to the wrong next position. The software is designed to be able to recover after a bad move.

The HWP angle sequence (Φ) is 0°, 45°, 67.5° and 22.5°. This sequence is designed to measure orthogonal polarization components between consecutive raster scans, allowing Stokes Q or U to be measured and avoids HWP rotations larger than 45° to minimize heating of the detectors due to motor vibrations.

2.7.5 Calibrator Lamp Control

For the 2010 flight the calibrator lamp was set to pulse for 300 ms every 15 minutes, so that the drifts in bolometer responsivity could be measured. The pulses are removed from the clean detector TOD in the data reduction pipeline (Section 4.3.2). However, the scan parameters were designed so that each raster scan took about 15 minutes. As a consequence calibrator lamp pulses often took place in the same region of a science scan.

The control software was changed for the 2012 flight so that a calibrator pulse would be triggered immediately before a HWP rotation and therefore at the edge of the map or after 20 minutes if a HWP move had not been triggered.

Chapter 3

BLASTPol Flight Performance

3.1 Chapter Overview

The BLASTPol experiment had two scientific flights, both launched from the Long Duration Balloon facility near McMurdo Station, Antarctica. The flight tracks of the two Antarctic flights are shown in 3.1.

In this Chapter I discuss the performance of BLASTPol during the two Antarctic science campaigns. The 2010 Antarctic flight had several issues including the failure of the primary azimuth pointing motor, a melted infrared blocking filter which caused additional systematics, and an additional highly correlated bolometer noise component. These issues were fixed for the 2012 Antarctic flight, though hard drive failures of both boresight star camera computers after six days will make pointing reconstruction for the second half of the flight challenging.

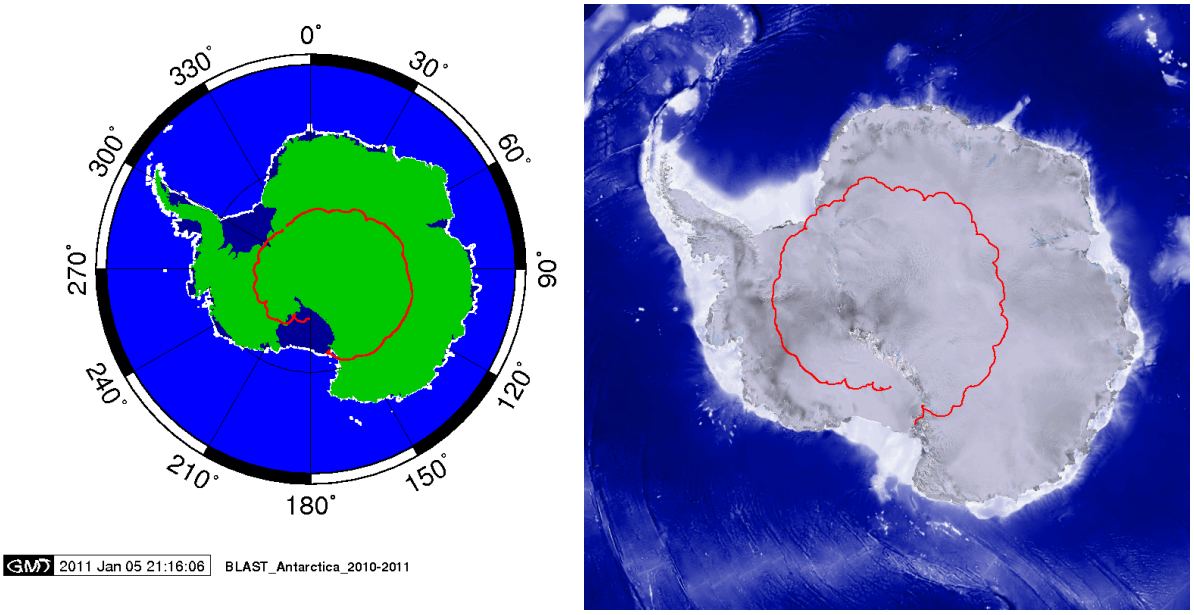

Figure 3.1: Flight paths for the BLASTPol 2010 (left) and 2012 (right) science campaigns. For both flights the telescope was launched in late December from the NASA Long Duration Balloon Facility near McMurdo Station, Antarctica and rose to a float altitude of ∼38 km, where the stratospheric winds pushed the balloon around the continent. The flights were terminated over the Ross Ice Shelf after 9.5 days for the 2010 flight and 16 days for the 2012 flight.

3.2 The 2010 BLASTPol Flight

3.2.1 Preflight Planning

BLASTPol Sensitivity Estimates

Prior to the 2010 BLASTPol science flight instrument sensitivity estimates were calculated based on map noise levels measured from the BLAST 2006 map of a 0.8 degree^2 region in the Chandra Deep Field South (Marsden et al. 2009).

The noise of BLAST (note: not BLASTPol) for a map of some defined size and total integration time is defined to be σ_I, in units of Jy/unit area. BLASTPol places polarizing grids in front of the detector arrays in an attempt to measure one of the linear Stokes parameters Q. The polarizing arrays are arranged so that every adjacent detector measures an orthogonal polarization component. Essentially half the detectors are used to make a map of I_{90} (the component of the incident radiation with polarization at 90°) and half the detectors to make a map of I_0.

The noise for the measurement of I_{90} and I_0 depends on the dominant source of noise for BLASTPol. If BLASTPol's noise is dominated by thermal fluctuations in the detectors, then $\sigma_{I90} = \sigma_{I0}$ is just $\sqrt{2\sigma_I}$ because only half the detectors were used for each map. Maps of I_{90} and I_0 can be used to generate a map of Q:

$$Q = I_0 - I_{90} \tag{3.1}$$

which then implies

$$\sigma_Q = \sqrt{\sigma_{I0}^2 + \sigma_{I90}^2} = 2\sigma_I. \tag{3.2}$$

In order to calculate the percentage polarization p and the polarization angle Φ both Stokes parameters must be measured. In order to map U ($U = I_{135} - I_{45}$), the half wave plate (HWP) must be rotated by 22.5°, which in turn rotates the polarization of the incoming light by 45°. That implies that half of the observing time is spent

mapping Q and half is spent mapping U. Thus

$$\sigma_Q = \sigma_U = 2\sqrt{2}\sigma_I. \tag{3.3}$$

It can be shown that

$$\sigma_p = \sigma_u = \sigma_q \tag{3.4}$$

where $q = Q/I$ and $u = U/I$. So *for the case where detector noise dominates:*

$$\sigma_p = \frac{2\sqrt{2}\sigma_I}{I}. \tag{3.5}$$

Now if the noise is dominated by fluctuations in the background loading the situation is different. Assuming the background loading radiation is unpolarized, then we would expect that the loading would be reduced by a factor of 2 due to the polarizing grid. That then implies that $\sigma_{I90} = \sigma_{I0} = \sqrt{2}\sigma_I/\sqrt{2} = \sigma_I$.

Propagating through this factor of $\sqrt{2}$ into equation 3.5 shows that *in the case where background loading fluctuations dominate the noise:*

$$\sigma_p = \frac{2\sigma_I}{I}. \tag{3.6}$$

For BLAST the noise was dominated by background loading fluctuations due to the telescope struts and warm optics (Pascale et al. 2008). However, for BLASTPol the loading is half that of BLAST because the polarizing grid rejects half the incoming radiation. It is possible that for BLASTPol the noise is no longer dominated by loading but instead by detector noise. The situation is further complicated by the fact that changing the detector load will also change the responsivity of the bolometers, which could lead to a reduced fractional JFET noise contribution. For flight planning purposes I assumed the pessimistic case that detector noise dominates and therefore used Equation 3.5 to convert from BLAST to BLASTPol noise levels.

To calculate BLAST noise levels instrumental noise measurements were taken from the BLAST 2006 0.8 square degree map of the Chandra Deep Field South (CDFS)

$\lambda\,(\mu m)$	250	350	500
beam FWHM ($''$)	36	42	60
σ_I (mJy/beam)	11	8.8	6.6
σ_I (MJy/Str)	0.32	0.18	0.069

Table 3.1: Instrumental noise estimates and beam sizes for the BLAST 2006 0.8 square degree Chandra Deep Field South map (Marsden et al. 2009).

region, which has much lower signal levels than any of the BLASTPol targets. The instrumental noise levels for these maps are taken from Marsden et al. (2009). In total BLAST spent 40.1 hours of telescope time on this map.

There are several advantages to using noise levels from an actual BLAST map to predict BLASTPol sensitivity instead of using theoretical BLAST detector noise levels. The CDFS map noise levels include:

- inefficiencies in the scan mapping strategy,
- non-uniformities in the scan coverage,
- time lost to cosmic rays and noise spikes in the the system,
- atmospheric loading,
- a realistic percentage of the detectors not working.

To generalize further one can scale a σ_I for a BLAST 2006 to a map of an arbitrary size and total integration time:

$$\sigma_{I06} = N \times \sqrt{\frac{map\ area}{beam\ area}} \times \frac{1}{\sqrt{t}}, \tag{3.7}$$

where t is the integration time for the map in seconds and N is noise equivalent flux density (NEFD), which is equal to 1.44, 0.97 and 0.52 MJy/Str $s^{0.5}$ at 250, 350 and 500 μm respectively.

$\lambda\,(\mu m)$	250	350	500
I_{req} (MJy/Str), t = 5hr	571	330	124
I_{req} (MJy/Str), t = 50hr	181	104	39

Table 3.2: Required source fluxes to obtain a percentage polarization 1-σ error of 0.5% for a 1 square degree BLASTPol map.

By rearranging equation 3.5 we can calculate the flux required in a map of an arbitrary size to obtain a certain percentage polarization error bar σ_p:

$$I_{req} = 2\sqrt{2}\frac{\sigma_I}{\sigma_p}. \tag{3.8}$$

Table 3.2 uses the above equation (with $\sigma_I = \sigma_{I06}$ and $\sigma_p = 0.005$) to calculate the minimum source flux needed to get a measurement of percent polarization with 1-sigma error σ_p <0.5% in a 1.0 square degree map, for total map integration times of 5 and 50 hours[1].

The uncertainty in the polarization angle (from which the field orientation is inferred) limits the ability to interpret magnetic field morphology in nearby molecular clouds. From the definition of σ_p in Equation 3.4 and using the relationship between q, u, p and Φ it can be inferred that if $\sigma_p << p$ then

$$\sigma_{2\Phi} = \frac{\sigma_q}{p} = \frac{\sigma_u}{p} = \frac{\sigma_p}{p}. \tag{3.9}$$

Equation 3.9 can be used to estimate the minimum signal-to-noise needed for a measurement of the percentage polarization p to obtain an acceptable σ_Φ in degrees:

$$\sigma_\Phi = \frac{180}{2\pi}\frac{\sigma_p}{p} = 28.6^\circ\,\frac{\sigma_p}{p}. \tag{3.10}$$

So to measure polarization with an angular uncertainty σ_Φ of 10°or less, we require a signal-to-noise ratio on the measurement of percent polarization of $p/\sigma_p > 3$.

[1]Note that the estimates in this section assume that the measurement uncertainties are dominated by statistical errors not systematic errors.

In some molecular clouds the surface brightness is known in the BLAST bands from previous BLAST or Herschel SPIRE maps. The above sensitivity relations can then be used to estimate the minimum polarization required for BLASTPol to make a three sigma detection of p for a given map size, integration time and scanning efficiency.

I wrote an IDL software routine called *sens_calc* which takes an input map and produces an output map of the minimum source polarization p_{req} for each BLASTPol beam sized pixel required to get a three sigma detection and the corresponding histogram of p_{req} for all pixels in the map. The beam sizes are assumed to be the same as those measured for BLAST in 2006 (Table 3.1).

Figure 3.2 shows the results for the BLASTPol 2010 target map of the nearby Vela C giant molecular cloud using BLAST maps from Netterfield et al. (2009) and assuming a scanning efficiency of 80%[2]. The panels on the left show p_{req} for a 1.4 square degree map of Vela C. Over most of the Vela C cloud we would expect BLASTPol to detect flux polarized at 2% to greater than 3σ. The histograms on the right show that if the cloud had a uniform p of 2%, then we would expect several thousand independent polarization detections in each of the three bands. This would be the most detailed submm polarization map of a molecular cloud to date.

In reality, as discussed in Section 1.4.3, p is expected to vary a great deal throughout the cloud. Lower density outer regions of the cloud tend to have a higher percentage polarization than the dense inner regions of the cloud.

3.2.2 Target Selection

In order to achieve the science goals for BLASTPol (see Section 1.5.4), we selected a number of molecular clouds with different properties. Priority was given to:

[2]Because of azimuth scan turnarounds and the fact that the detector array has a $13.5' \times 6.5'$ field of view some percentage of map pixel hits will be outside the requested scan region.

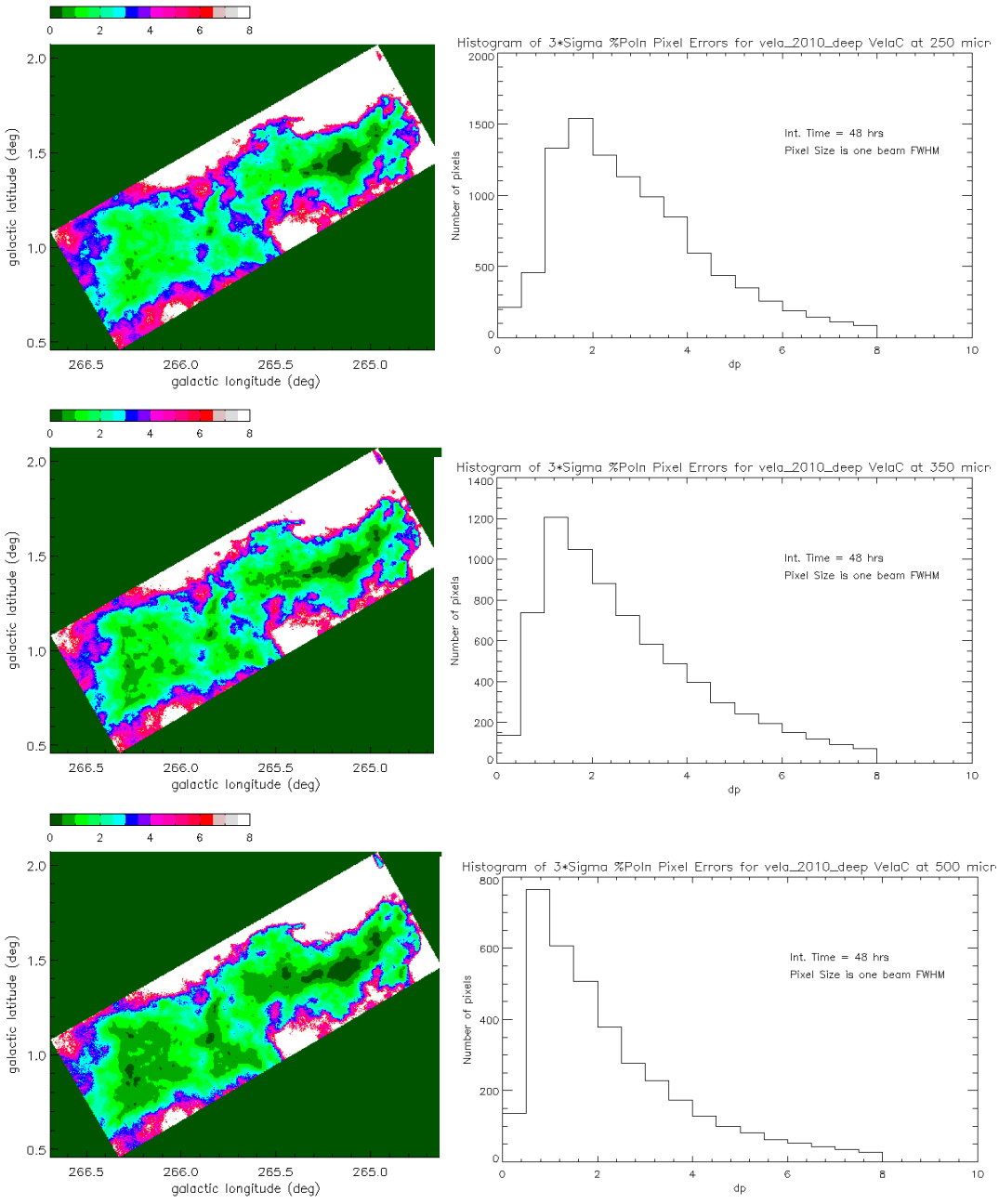

Figure 3.2: Sensitivity estimates for a 1.4 degree^2 BLASTPol 2010 map of Vela C using *sens_calc* at 500 (top), 350 (middle), and 250 (bottom) μm. The left plots show p_{req}, the minimum source percentage polarization for which BLASTPol would be able to obtain at least a 3-sigma detection in a beam sized pixel. The right plots show histograms of p_{req} over the map.

- Nearby clouds, to maximize linear resolution;
- Clouds off the Galactic plane or if on the Galactic plane clouds with ^{12}CO lines that show little evidence of multiple clouds at different distances along the line of sight;
- Relatively cold clouds or clouds where star formation is its initial stages, so as to avoid observing clouds with HII regions which may dominate the magnetic field morphology;
- Observational constraints (e.g. number of hours visible per day, scheduling conflict with high priority targets).

Our goal was to observe different types of molecular clouds, including nearby Gould's Belt Objects, Giant Molecular Clouds (GMCs) and Infrared Dark Clouds in order to create a rich dataset that can be used to investigate magnetic field morphology in different star formation environments.

Figure 3.3 gives a rough estimate of the sky available for BLASTPol to observe during an Antarctic summer flight. Target visibility depends on the drift of the telescope in latitude: as the balloon drifts further north more targets become visible. In addition, the launch date affects visibility of targets as BLASTPol can only observe over an azimuth range of 40-170° with respect to the sun. Each day the location of the sun with respect to the celestial sphere moves by $\sim$1°, so a later launch date means that targets closer to the Galactic center are easier to schedule. A detailed discussion of BLASTPol scheduling considerations can be found in T. Matthew's thesis (Matthews 2013).

The nearest star forming region visible to BLASTPol was the Lupus Clouds (Comerón 2008), consisting of a number of low mass clouds within 200 pc, with a total mass of a few $10^4\,M_\odot$. The Lupus clouds are located well off the Galactic plane, so there is little chance of confusing polarized emission from the Lupus clouds with

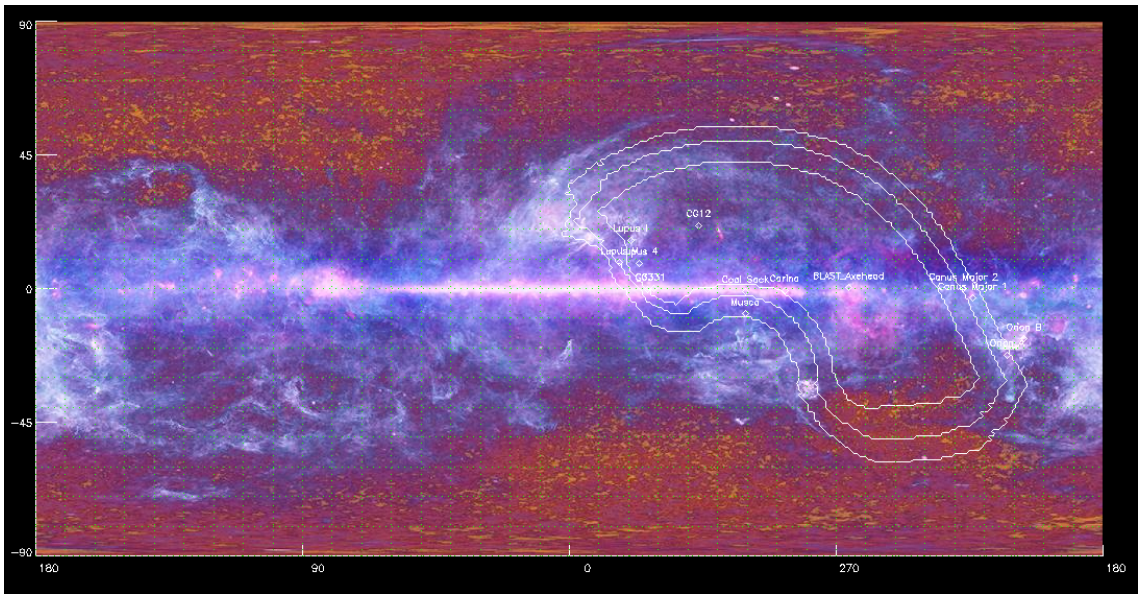

Figure 3.3: Sky visible to BLASTPol, plotted over the public release Planck all sky image. The three contours show roughly what areas of the sky could be visible for at least 3 hours of a flight (Matthews 2013). *Inner Contour:* Targets should be visible under the the most pessimistic flight assumptions (e.g. telescope drifts south, early launch), *Middle Contour*: Targets should be visible under typical flight trajectories, *Outer Contour:* Targets that might be visible if the telescope were to drift far north or launch much later than expected.

emission from more distant clouds. At 155 pc, the distance of Lupus I, BLASTPol's best resolution of 36″corresponds to a linear scale of 0.02pc, sufficient to resolve filaments and cores. In addition a dense, bright, relatively isolated clump in Lupus IV which became visible two days after Lupus I was chosen as a secondary target.

BLAST 2006 created a 48 degree^2 map of the Vela Molecular Ridge (VMR) (Netterfield et al. 2009), a massive relatively nearby (most gas thought to be at d$\sim$700 pc) star forming complex (Pettersson 2008) which was visible for approximately three quarters of the BLASTPol flight. The top priority target was Vela C, a massive[3] young star forming region which contains the ultra compact HII region RCW 36. With a map size of 1.4 deg^2, the 2010 Vela C map was the largest region targeted by BLASTPol: several thousand polarization detections were expected (Figure 3.2).

Vela Y, selected as a secondary VMR target, was discovered by BLAST (Netterfield et al. 2009) and appears to be of comparable submm brightness to the cold southern regions of the Vela C cloud, but has a much simpler morphology with emission concentrated in a single dense filament.

A high right ascension Galactic plane target was chosen in the constellation of Puppis. A series of GMCs and IRDCs were also selected from both IRAS and QUAD (Ade et al. 2008) maps (used to select relatively cold objects) and NANTEN ^{12}CO J=1-0 data cubes (Mizuno & Fukui 2004) (used to select objects with minimal line of sight contamination).

In addition several calibrators were targeted:

- Polarization Calibrators: The SPARO instrument observed both the Carina Nebula and G 331 (Li et al. 2006), two GMCs also visible to BLASTPol. Both have well characterized polarization angle structure, and the central regions of G 331 were found by SPARO to have negligible polarization $< 0.2\%$. This

[3]The dense gas mass of Vela C traced by C^{18}O is $\sim 5 \times 10^4 M_\odot$ (Yamaguchi et al. 1999)

central region was used as a check of the instrumental polarization removal in the BLASTPol 2010 reduction pipeline (Section 4.3.8).

- Beam Calibrator: The only true point source observed was the star, VY CMa in the Canis Major constellation. For the 2012 BLASTPol flight the sunshields were altered so that BLASTPol could observe Saturn, which was found to have negligible polarization in observations at 350 μm taken with the SHARP polarimeter at the Caltech Submillimeter Observatory (Srisuwananukorn 2013; Matthews 2013).

- Pointing Calibrators: As the angle between the star camera axes and submm beam varies with time, periodic maps were made of bright compact sources. BLASTPol used two primary pointing calibrators: IRAS 08470-4243 and IRAS 15100-5613, which are located near the Vela and Lupus Molecular clouds respectively.

3.2.3 Flight Overview and Performance

BLASTPol was first launched on December 27th, 2010 at 5:06PM New Zealand time from the Long Duration Balloon Facility near McMurdo Station, Antarctica. The mass of the science payload (not including NASA electronics, ballast or the balloon flight train) was 1832 kg. The trajectory of the payload is shown in Figure 3.1. BLASTPol flew for 230.8 hours, and eventually the flight was terminated over the Ross Ice Shelf, 613 km from McMurdo Station on January 6th, 2011.

The altitude over the course of the flight is shown in Figure 3.4. The payload rose over the course of six hours to a stable float altitude of approximately 39 km above sea level. For the rest of the flight telescope altitude varied between 36.5 to 40 km. The sinusoidal variation in the telescope altitude is diurnal and is caused by the change in sun elevation. Later in the flight as the telescope began to drift further south the

amplitude of this diurnal effect decreased.

3.2.4 Balloon Ascent

BLAST was launched on a 39 million cubic foot balloon manufactured by Aerostar International, Inc. of South Dakota, USA. The launch took place at December 27th 2010 at 5:06PM New Zealand time. The initial climb rate over the first 3 km of altitude gained was 5.2 m/s. The rate of climb decreased significantly as the atmospheric pressure dropped off, reaching 1.9 m/s after passing through the tropopause approximately 45 minutes after launch. Several drops of ballast were made to keep the balloon rising. Eventually, 6.0 hours after launch the telescope reached a stable altitude of 39.6 km above sea level corresponding to a pressure of $\sim$0.005 atm.

The motors were powered off before launch and the inner frame was locked at an elevation of 45°. The maximum sun elevation at the launch site (latitude $= -77.8°$) is 35.5°, so there was no chance that the sun would be in the field of view of the telescope. This was important because after launch a combination of wind and large pendulations induced by the launch meant that the motor control system did not have sufficient torque to point the telescope. As shown in Figure 3.7, the telescope acted as a torsion pendulum in azimuth, crossing the meridian of the sun several times.

At an altitude of 26.8 km 2.9 hours after launch the wind drag had decreased to the point that we were able to power the motors and point the telescope in azimuth. Then 3.3 hours after launch the lock pin holding the inner frame in place was removed and the telescope was able to point in elevation.

3.2.5 Damage to an Infrared Blocking Filter

After the recovery of the telescope it was noted that the first filter in the infrared filter stack had been damaged (see Figure 3.5). In previous BLAST flights a thicker, white

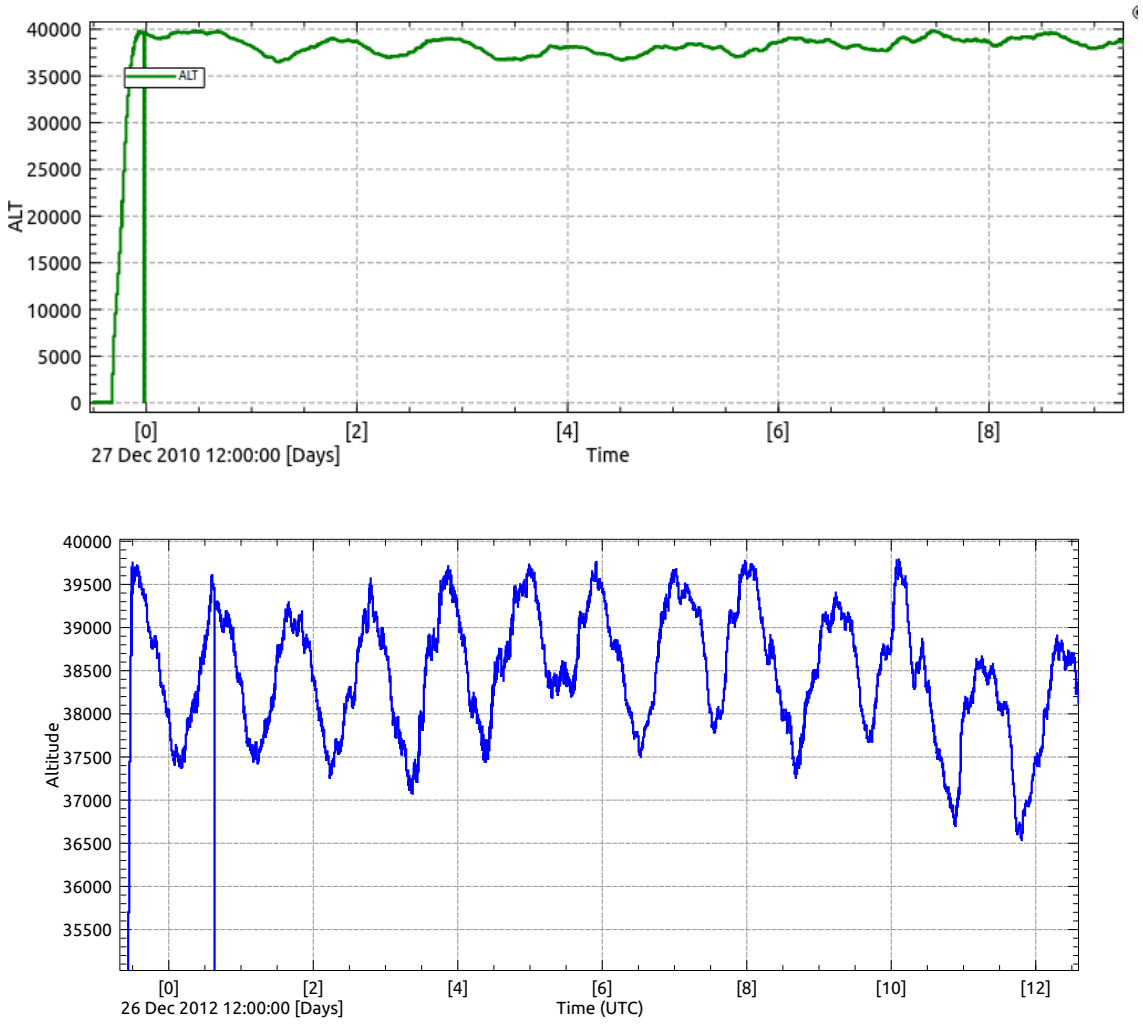

Figure 3.4: Altitude of BLASTPol during the 2010 (top) and 2012 (bottom) flights as measured by on-telescope GPS units. The plot of the 2010 altitude includes the launch and shows the rapid rise of the telescope before it settled at an altitude of ∼39.5 km. The plot of the 2012 altitude does not include the launch but instead shows in detail the altitude variations at float. The apparent sudden drop in altitude early in the flights are data interruptions caused by both flight computers rebooting at the same time.

Figure 3.5: Picture of the first infrared blocking filter in the filter stack mounted just behind the cryostat window. This filter was first flown in 2010 (previous BLAST flights used a thicker filter) and was found to have been damaged after telescope recovery. The likely cause of the damage was sunlight incident on the filter while under vacuum.

and completely opaque filter was flown, but for 2010 it was replaced with a thin filter to reduce loading on the cryostat liquid nitrogen stage.

The only optical element in the cryostat before the damaged filter is the cryostat vacuum window, which is transparent to visible and infrared light. The damaged infrared blocking filter consisted of copper printed on a substrate and so could absorb a significant fraction of optical light. Because the filter was mounted just behind the vacuum window no convective or conductive cooling via air interaction was possible. The filter is also thin and therefore a poor infrared emitter. Thus the most probable cause of the damage to the filter is that at some point sunlight shone directly on the vacuum window of the cryostat. The filter was unable to cool and consequently deformed.

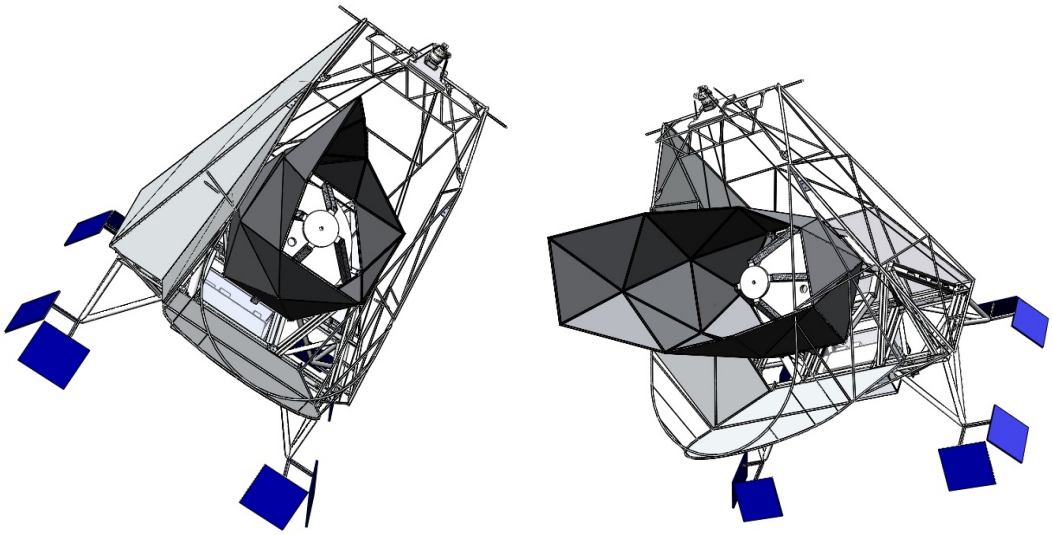

Figure 3.6: Model views of BLASTPol viewed from the altitude and azimuth of the Sun. In these figures the BLASTPol inner frame is at an elevation of 42.5°, and the Sun altitude is 31°, the altitude of the Sun at the time of the 2010 launch from Antarctica. *Left:* View of the telescope for $Az - Az_{\odot} = 10°$. *Right:* View of the telescope for $Az - Az_{\odot} = -35°$. In both cases the receiver vacuum window (directly behind the hole in the primary mirror) is visible and therefore sunlight would illuminate the IR blocking filter stack directly behind the window.

BLASTPol was launched with the inner frame housing the telescope locked at an elevation of 45°. The maximum altitude of the sun is 35.5° at a latitude of -77.85°, so the telescope could never accidentially point directly at the sun during launch. However post-flight it was realized that over a range of azimuths ($-35° < Az - Az_{\odot} < 10°$) the sun could directly illuminate the vacuum window and therefore the first IR blocking filter, as shown in Figure 3.6.

After launch the telescope spun in azimuth past the Sun several times (Figure 3.7). Assuming that the Sun illuminated the filter over the $Az - Az_{\odot}$ range of -35 to 10°, the filter was illuminated for a total of 5 minutes, with the longest continuous period of illumination ∼50 seconds. It is also possible that the telescope was pointed too close to the Sun before launch, either on the launch day or during preflight outdoor

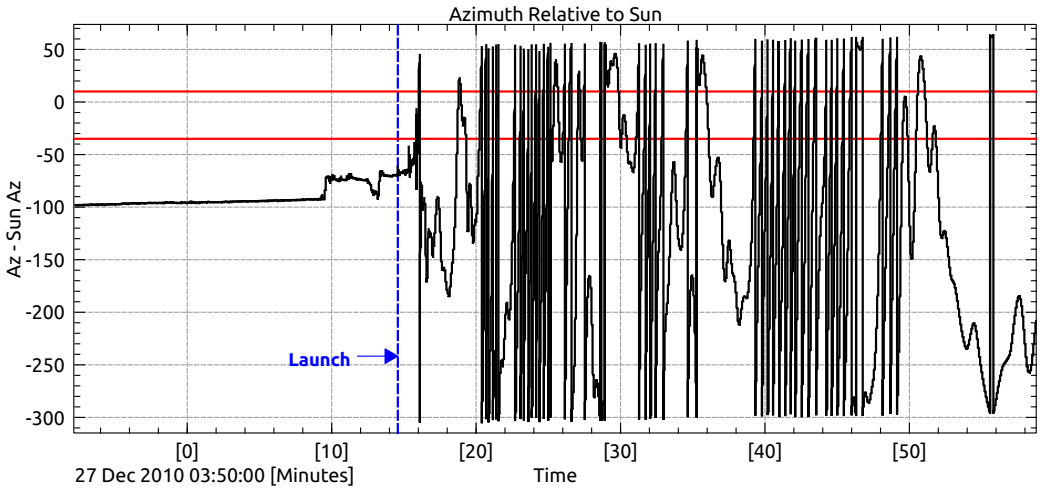

Figure 3.7: Azimuth of BLASTPol (as measured by the magnetometer) relative to the azimuth of the Sun before, during and after the launch on December 27th, 2010 vs time (UTC). The telescope spun rapidly in azimuth after launch. The two horizontal red lines show the range in azimuth over which the vacuum window was visible to the Sun.

calibrations.

The damaged filter appears to have degraded the optical performance of the telescope in terms of both the beam shape and instrumental polarization. Further discussion can be found in Section 4.2.

3.2.6 Additional Correlated Noise

During the 2010 flight the bolometer time ordered data (TOD) showed intermittent features which were highly correlated across all bolometers. These correlated features were also present in the dark channel TOD (Figure 3.8), so it is clear that they were not caused by astrophysical sources.

This correlated noise component was always present, though the amplitude varied considerably with time. It also showed a strong correlation with current spikes, in particular with spikes in the motor currents. Post-flight it was discovered that part

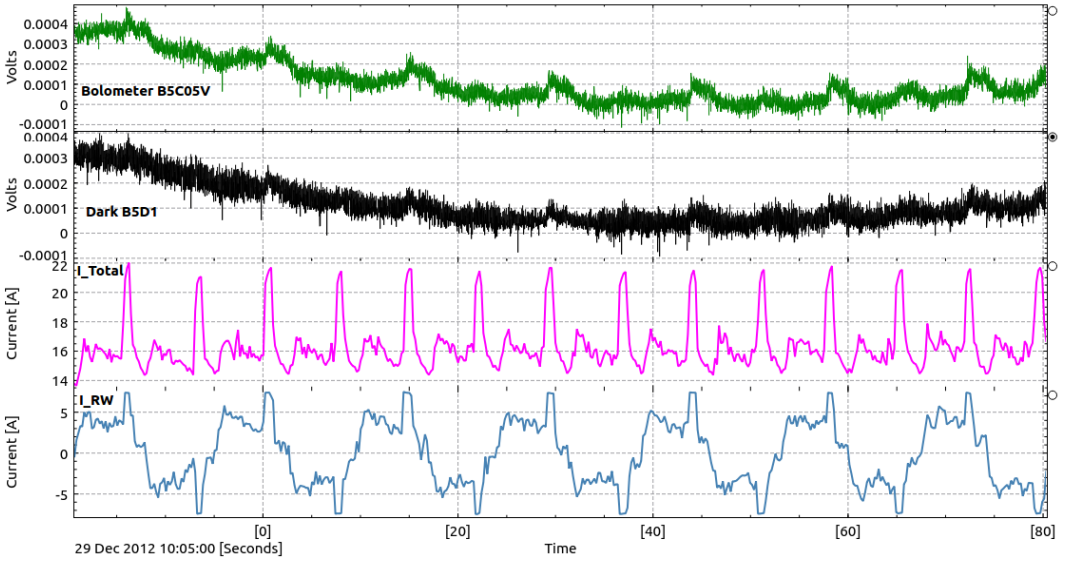

Figure 3.8: BLASTPol 2010 detector TOD showed an anomalous noise component, which was highly correlated across all the bolometer data (both science and dark bolometers). The top panel shows 500 μm bolometer B5C05V data over 1.5 minutes, while second panel shows the data over the same period for a dark bolometer. This extra noise is also highly correlated with current spikes in the power system (third panel) and in particular with the reaction wheel motor current (bottom panel).

of the noise was caused by a combination of motor current switching noise inducing radio frequency (RF) noise on the detectors and RF noise associated with TDRSS transmission (see Figure 3.12).

3.2.7 Reaction Wheel Motor Failure

The pointing motors were switched on 2.90 hours after launch. The reaction wheel motor (RW) immediately showed increased friction compared to preflight performance, and thereafter the motor performance continued to degrade.

One way to infer the level of friction in the the reaction wheel motor is to look at the average current required to keep the reaction wheel spinning at or near its velocity set point. (A thorough discussion of the reaction wheel control algorithm can be found in Section 2.6.4). Averaged over long periods of time the reaction wheel current in a frictionless system should be zero, because the pivot motor provides the long time constant angular momentum transfer.

Before launch an average current of less than 0.3 Amps was needed to keep the reaction wheel motor spinning at $50^\circ/\mathrm{s}$. After launch when the motors were powered the average current required was $\sim$0.7 Amps, and it continued to rise to $\sim$5 Amps 14 hours after launch (Figure 3.9). The reaction wheel motor controller was limited to a maximum continuous DC current of 6 Amps, so the controller could not provide sufficient current to both keep the motor spinning and apply pointing corrections. As a result BLASTPol was unable to point in azimuth.

Post-flight when the reaction wheel was recovered the motor bearing was found to have seized. There were several possibilities for the corruption of the bearing:

- *Rusted bearing:* After cold testing of the motors at the NASA balloon facility in Palestine, Texas six months before the launch the motors were exposed to ambient temperature and humidity before coming into thermal equilibrium with the room resulting in water condensation on the motor surfaces. It is possible

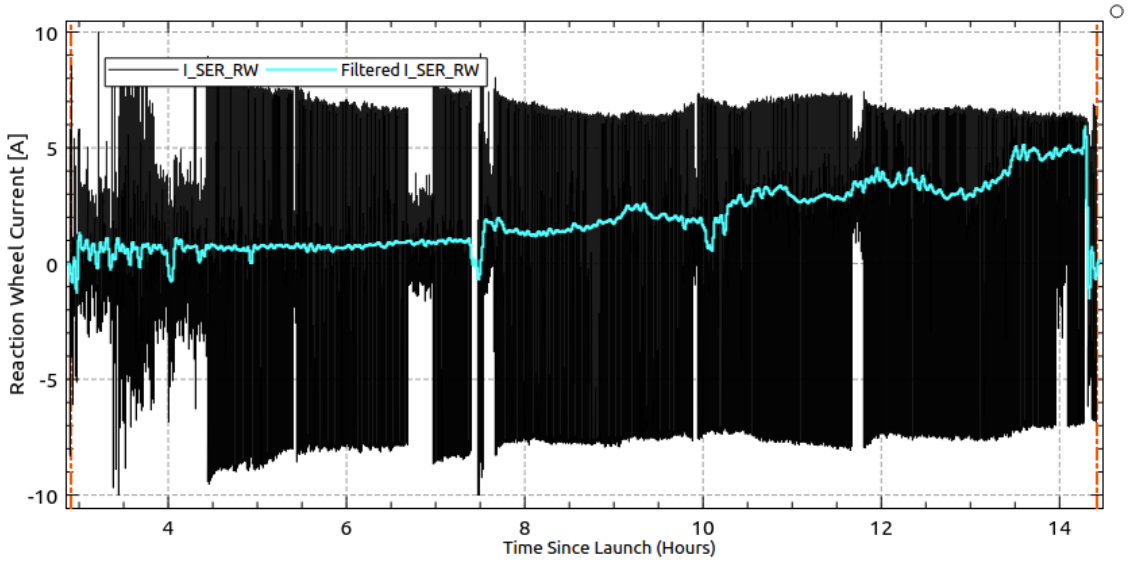

Figure 3.9: Degradation of the BLASTPol reaction wheel motor performance near the beginning of the 2010 flight. Black lines show the reaction wheel (RW) current as measured by the motor controller, while the cyan line is the RW current low-pass filtered a with cutoff frequency of 0.1 Hz. The filtered current shows a gradual rise as the current needed to keep reaction wheel spinning at an average speed of 50°/s increased. The left dashed orange marker shows when the RW motor was powered on 2.90 hours after launch and the right dashed orange line shows when the RW motor was powered off after the control loop saturated and the telescope was unable to point in azimuth.

that some humid air may have passed through the bearing seal and condensed on the bearing itself, causing rusting. But it is difficult to understand why the bearing failure would only become apparent during flight and not in the previous six months of testing.

- *Damage to the bearing during low temperature grease application:* Before having the motor shipped, the manufacturing company opened the bearing and replaced the standard bearing grease with low temperature grease. It is possible that some contaminant was accidentally added at this point, but again it is difficult to understand why the problem would only become apparent in flight.

- *Bearing damage during launch accelerations:* From previous BLAST flights it is known that the payload can experience angular accelerations of several hundred degrees per second when the telescope is released from the launch vehicle. It is possible that the bearing could have been damaged or warped during launch, and the damage worsened with usage.

Ultimately we still do not know what caused the failure of the reaction wheel motor. The motor was returned to the manufacturer for analysis but they only replaced the bearing and returned the motor without providing an explanation for the problem or any information on whether the bearing itself was warped. A different motor was purchased for the 2012 flight.

3.2.8 Pointing Control Post-Reaction Wheel Failure

As explained in Section 2.6.7, BLASTPol's motor control loops were designed to use the reaction wheel to power the azimuth scans by providing torque proportional to the velocity error (Equation 2.27). The pivot motor function was to keep the reaction wheel spinning near the commanded set point speed. In addition there is a term in the pivot control loop (Equation 2.29) which is proportional to the azimuthal velocity

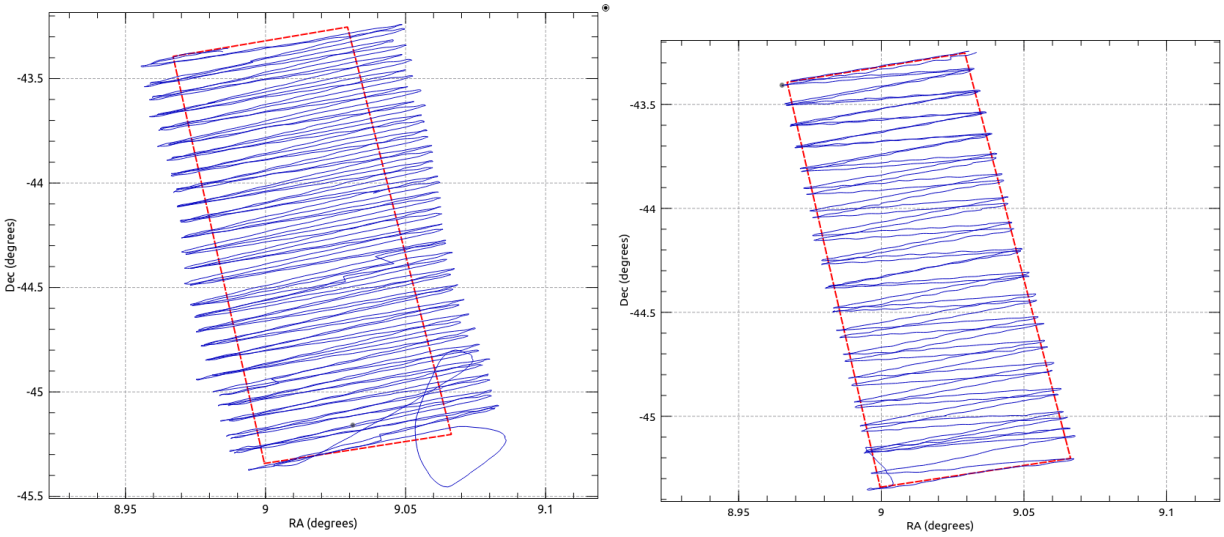

Figure 3.10: Two examples of BLASTPol scan trajectories of the Vela C Cloud after the 2010 reaction wheel motor failure. The red dashed quadrilateral shows the boundary of the requested scan region. *Left:* An early pivot only scan. *Right:* A scan with most of the torque provided by the pivot motor but with the broken reaction wheel motor also contributing.

error, in case the reaction wheel alone could not provide sufficient torque to power the azimuth scans. At the start of the flight it was thought this term would not be necessary, so the gain for this term, $g_{p\,piv}$ was set to zero. However after the reaction wheel broke, it was this term which allowed us to point the telescope and continue the BLASTPol science program.

After the reaction wheel broke, early attempts were made to scan in azimuth using just the pivot motor (Figure 3.10 left panel). The gain term $g_{p\,piv}$ was set to its maximum possible value of 32,766 and all other gain terms were set to zero. For much of the time the pivot was able to roughly scan the correct area, although not with the same precision as the more responsive reaction wheel motor. The main problems were that the pivot proportional term was saturated, and that the pivot control loop did not have an integral term to provide additional current to overcome telescope cross-winds.

Time	$g_{p\,az}$	$g_{i\,az}$	$\omega_\circ$	$g_{p\,piv}$	$g_{rw\,err\,piv}$	I_{frict}
Pre-RW Failure	4000	1000	50 °/s	0	400	0.3 A
Pivot Only Scans	0	0	0	32766	0	0
Pivot+RW Scans	3000-6000	50	-6 to +4 °/s	32766	5000	0.3 A

Table 3.3: Azimuth motor current gains for the 2010 BLASTPol flight. The gains are: $g_{p\,az}$ the reaction wheel proportional gain, $g_{i\,az}$ the reaction wheel integral gain, $\omega_\circ$ the reaction wheel set point velocity, $g_{p\,piv}$ the pivot proportional gain, $g_{rw\,err\,piv}$ the pivot reaction wheel velocity error gain, and I_{frict} the pivot friction offset. The gains and motor control loops are discussed in Section 2.6.7

Control was improved when it was discovered that the broken reaction wheel motor could still be used, albeit in a limited fashion. The reaction wheel motor could not spin faster than $\sim 15^\circ$/s, and the large friction meant that the speed would soon decay to back to zero. However the reaction wheel was still able to provide torque on short timescales, while the pivot provided torque on intermediate and long timescales.

Furthermore changing the reaction wheel set point velocity could be used to obtain additional torque from the pivot (see Equation 2.29). A larger set point velocity would cause the pivot to output additional current to try and make the reaction wheel spin faster. However the reaction wheel at this point had too much friction to spin continuously at any non-zero velocity. In essence, the reaction wheel set point was used as a commandable pivot integral term. Table 3.3 compares the motor gains used before the reaction wheel broke, during pivot motor only scans and scans using both the pivot and the damaged reaction wheel.

3.2.9 Pointing System Performance

Overall the in-flight pointing reconstruction was acceptable. The two boresight star cameras had intermittent connection problems and had to be power cycled several

times during the flight. In addition for some targets, in particular for Vela C, the star cameras had trouble finding enough stars to obtain in-flight pointing solutions.

After 7 days 1 hour and 46 minutes after launch one of the two redundant star cameras failed. Repeated power cycling of the camera could not restore a connection. Post flight inspection showed that the hard drive, a conventional magnetic recording hard disk drive, failed. However the star positions from the first seven days of the flight had been written to the flight computer hard drives as part of the BLASTPol dataset.

Coarse sensors performed more or less within required tolerances. A detailed description of the pointing performance of BLASTPol will be included in N. Gandilo's thesis.

3.2.10 Flight Computer Double Reboot

Early in the flight, 7.41 hours after launch, the in charge flight computer was rebooted by the watchdog circuit (see Section 2.5.1), most likely due to a cosmic ray upset. During the control switchover the other flight computer also crashed. Post flight it was found that a percentage of flight computer switchovers would cause a double reboot, though the frequency depended a great deal on the telescope power load.

The driver for the serial hub will not communicate with a computer which has been rebooted for a period of $\sim$5.5 minutes so the elevation encoder could not be readout and therefore returned an elevation of zero. The star cameras were not returning pointing solutions immediately after the reboot so the motor control loops applied maximum current to drive the inner frame to its maximum elevation. Motor control returned once the serial communications black-out ended.

3.2.11 BLASTPol 2010 Targets Observed

Table 3.4 lists the fourteen objects observed by BLASTPol during the 2010 flight. The observations were scheduled in more or less two blocks. First the targets far in azimuth from the Sun were observed such as Vela C, Vela Y, VYCMa, Puppis, CarinaTan, and the Carina Nebula. In the second half of the flight BLASTPol observed targets closer in azimuth to the Sun including Lupus I & IV and several inner Galaxy GMCs and IRDCs. This observing strategy was designed to minimize changes in the primary and secondary mirror temperatures which might change the focus of the telescope.

3.2.12 BLASTPol 2010 Data Quality and Lessons Learned

The 2010 dataset had serious problems in terms of the beam shape, systematics due to the melted filter, extra noise and difficulty pointing due to the damaged reaction wheel motor.

Pointing control was mostly recovered after the reaction wheel broke by using the pivot to power the scans with the reaction wheel operating in a reduced capacity for added control. A new more robust reaction wheel motor was purchased for the 2012 flight.

Approximately $\sim$50% of the bolometer data had to be rejected because of contamination by spurious TOD features that appeared in both the science and dark detectors (see Sections 4.2.1 and 4.3.5). This was especially problematic for observations of bright sources such as G331 and the Carina Nebula, where removing 50% of the data resulted in minimal coverage of at some HWP angles.

Additionally, there was a problem with our point source calibration strategy. The goal was to achieve uniform coverage at each of the four HWP angles. Science targets scans are scheduled in $\sim$1 hour blocks consisting of an up and down raster at each HWP position. Pointing calibrators are only observed every 4 to 8 hours, with an observation consisting of a single fifteen minute raster at one HWP angle. The

Target Name	RA (J2000) (HH:MM:SS)	Dec (J2000) (DD:MM:SS)	Map Area (deg^2)	Time Observed (HH:MM:SS)	Type[a]	Dist (kpc)
IRAS 08470-4243	07:22:58	-42:54:24	0.1	4:54:30	Pt	0.7
VYCMa	07:22:58	-25:46:03	0.1	1:18:00	Pt	1.2
Vela C	15:13:50	-56:24:46	1.4	56:43:00	GMC	0.7
Puppis	07:35:00	-23:30:50	0.1	23:29:00	MC	1.0
Vela Y	09:02:52.90	-46:43:04.7	0.1	7:38:00	MC	~ 0.7
Carina Nebula	10:42:35	-59:42:15	0.8	2:51:00	C, GMC	2.3
Lupus I	15:42:22	-33:50:28	0.7	48:48:30	DC	0.155
Cen A	13:25:28	-43:01:09	0.1	2:25:00	Pt, G	3800
CarinaTan	10:02:07	-57:09:02	1.5	13:28:25	GMC	2-3
IRAS 15100-5613	15:13:50	-56:24:46	0.1	1:08:00	Pt	N/A
G331	16:12:10	-51:27:51	0.2	2:51:00	C, GMC	7.5
G3219	15:19:51	-57:20:32	0.5	5:01:00	GMC	<8
Lupus IV	16:01:22	-41:57:24	0.3	13:21:30	DC	0.155
G3237	15:31:39	-56:32:43	0.2	2:56:00	IRDC	<8

Table 3.4: Regions observed during the 2010 BLASTPol Antarctic flight. Lists the target name, RA and Dec of the map center, target map area, total time spent observing the target, type of target, and distance to the target region.

[a]GMC: Giant Molecular Cloud, DC: dark cloud, MC: molecular cloud, IRDC: Infrared Dark Cloud, Pt: Pointing Calibrator, C: Polarization Calibrator, B: beam shape calibrator, G: Galaxy

calibrator rasters therefore tended to be taken at the same HWP angles. For the 2012 flight additional flight code was written to allow the starting HWP angle of the next observation to be commanded, and the number of rasters at each HWP position was carefully tracked.

Evidence collected so far indicates that the melted filter acted as a partial polarizer (at the few percent level) and a partial polarized scatterer at an unknown level. The implications for the instrumental polarization are discussed in the next chapter, but the lesson learned for the 2012 flight was that both protection for the cryostat window and a more robust first IR blocking filter were needed.

For the 2010 flight the map sizes were kept relatively compact around the source, with the goal of optimizing scan depth on each target. However, because the BLASTPol data are high-pass filtered at a frequency of 0.05 Hz in the mapmaking stage large-scale spatial modes are lost and the output I, Q and U maps have a mean of zero. The I, Q and U maps must therefore be referenced to a region or regions in the map which have very low flux. For the 2010 data, the small size of our maps meant that only small reference regions that were usually near bright cloud structures could be used.

3.3 BLAST2012 Flight Preparation

3.3.1 Reference Regions

A major problem for the 2010 analysis pipeline (see Section 4.2) was that the map making algorithm is unable to solve for low frequency spatial modes which are supressed due to the high-pass filtering of the TOD in the mapmaker. The resulting I, Q and U maps have a mean of zero, with large regions of the maps having negative flux.

To zeroth order[4] this problem can be modelled as:

$$I' = I - I_{ref} \tag{3.11}$$

where I' is the measured intensity, I is the true intensity and I_{ref} is the lost signal due to the bolometer response/mapmaking strategy. Similar equations hold for Q and U. To solve for I_{ref} it is helpful to have regions of the map where it is expected that dust emission should be minimal. It is then assumed that the true mean I, Q and U levels in these reference regions are zero. The mean (negative) flux in the reference regions is measured and subtracted from the rest of the map in an attempt to reconstruct the total flux (I, Q, and U).

For maps of Stokes I, the total intensity, it is fairly straight forward to define reference regions. We select a large area of low submm brightness (or of low extinction if submm maps are not available). However for Q and U, this becomes more difficult, partially because Q and U can be either positive or negative, but also the percentage polarization $p = \sqrt{(Q^2 + U^2)/I^2}$ tends to increase with decreasing submm brightness. Thus the constrast in polarized intensity P where

$$P = \sqrt{Q^2 + U^2} \tag{3.12}$$

between a region of low dust column and a region of high dust column is expected to be much less than the contrast between the same regions in I. It is therefore advantageous to have large reference regions, in order to average out any small scale variations in polarization direction.

In 2010, the focus was to make compact maps in order to maximize the map depth. In the post-flight analysis it was realized that uncertainty due to zero flux levels was a significant issue, particularly for the Vela C map, which has several regions of high percentage polarization but low I[5].

[4] In reality, more spatial modes than the zero mode are lost with the current BLASTPol mapmaking strategy. To properly correct for these lost modes will require the development of an optimized polarized mapmaker.

[5] This can clearly be seen in the 2012 Vela C maps shown in Section 5.4.1.

For the 2012 flight, the size of the maps was increased to include regions of low extinction. Additionally for our primary science target, Vela C, a large reference region map was made. Vela C is part of the extended Vela Molecular Ridge, as such it is surrounded by regions of significant dust column which may well be polarized. A much larger (10 $\deg^2$) region within Vela was observed as a separate reference map as shown in Figure 3.11. This reference map includes the science map, but also includes a large area above Vela C with very low dust column.

3.3.2 Elevation Scans

On long timescales the BLASTPol detector TOD are dominated by low frequency 1/f noise. As a consquence the 2010 TOD were filtered with a high-pass filter of 0.05Hz. Thus any signals on timescales longer than $\sim$20 seconds are lost. A typical map width for BLASTPol is $\sim 1^\circ$ and a typical scan speed is $0.1^\circ/s$. So the map crossing time is $\sim$10 seconds. That implies that while cloud structures along azimuth scan direction will be well constrained the structure gradients in the elevation direction may be filtered out.

To compensate I developed elevation scanning modes. For conventional scans the telescope moves primarily in the azimuth direction while the elevation changes at a much slower rate. During elevation scans the telescope scans primarily in the elevation direction while drifting at a slow azimuth speed. Elevation scans should allow the recovery of intensity gradients in the elevation direction as long as the astrophysical signals can be separated from the elevation correlated TOD features discussed in 4.3.4.

3.3.3 Experiment Upgrades for the 2012 Flight

Damaged IR Blocking Filter

The damaged filter from the 2010 flight was replaced by a new thicker filter. In addition an aluminum shutter controlled by a stepper motor was built and placed

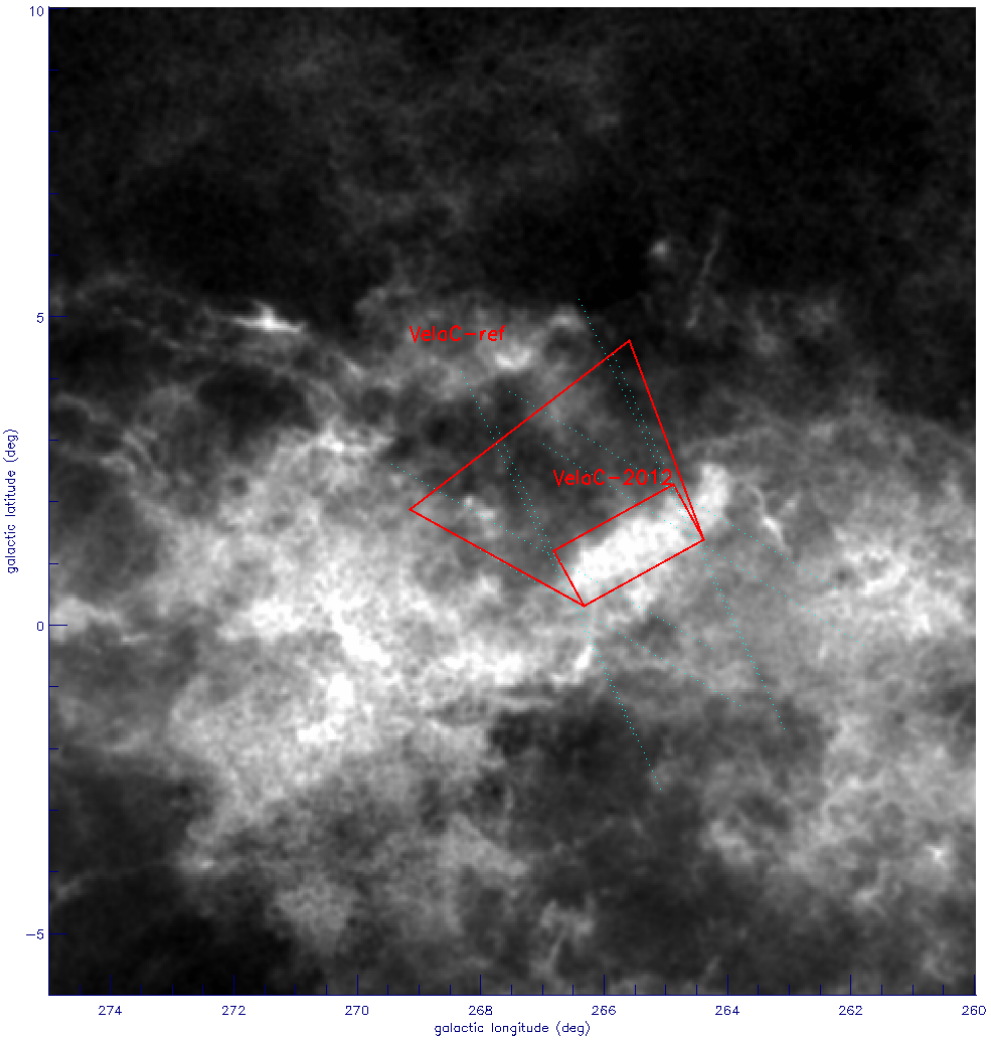

Figure 3.11: Vela C 2012 science map, and reference map areas plotted over a DSS dust extinction map (Dobashi et al. 2005). The dotted blue lines indicate the azimuth scan direction for the maximum and minimum parallactic angles at which Vela C could be observed.

in front of the optics box window. The shutter remains closed during the launch, protecting the cryostat window from sunlight and is opened once the telescope is at float altitudes and pointing.

Reaction Wheel Motor Replacement

As described in section 3.2.7 the reaction wheel appeared to have been damaged on launch and failed completely 14 hours into the 2010 flight. The entire motor was replaced with a Kollmorgen D063M motor, which has a dual bearing system (the previous D062M motor had a single bearing). Also for the new motor, we did not request that the standard bearing grease be replaced with low temperature grease, so the motor bearing seal did not have to be opened.

Pointing Sensors

Because the pinhole sun sensors (PSS) worked very well during the 2010 flight we added an additional two PSS units to the gondola for the 2012 flight, bringing the total to four units. Each of the PSS units provide coverage of 40° so we were able to get azimuth from at least one PSS over the entire range of Az-$Az_{\odot}$ allowed by the sunshields. The calibration and perfomances of the PSS units will be discussed in N. Gandilo's thesis.

In addition we did not fly a differential GPS unit during the 2012 flight, instead we read data from the DGPS unit flown as part of the NASA support electronics.

Calibration Strategy

Saturn was added as a beam calibrator for the 2012 flight. It is compact, known to have low polarization in the submm (Srisuwananukorn 2013) and is very bright. The brightness of Saturn compared to other beam calibrators, makes it an ideal target to map out telescope side lobes. However Saturn appears very low on the horizon from

Antarctica (the maximum elevation of Saturn is $<25^\circ$). Modifications were made to the ground shield so that the telescope could point down to 20° in elevation.

In the 2010 data we had poor coverage of our calibrators at some HWP angles (see Table 4.1 in Chapter 4). A command was added to the flight software program *mcp* that allowed the starting HWP angle for the next target to be commanded, and a tally was kept for each target in the Observation Log of the number of raster scans at each HWP position.

3.4 The BLASTPol 2012 Flight

The second BLASTPol launch took place on December 26th, 2012 at 6:55AM, again from the Long Duration Balloon Facility near McMurdo Station, Antarctica.

The payload trajectory is shown in the right panel of Figure 3.1. The balloon did not drift as far south as in 2010 and the circumpolar wind speeds were also much slower, so it took BLASTPol 16 days, 3 hours and 17 minutes to complete its journey around Antarctica (compared to 9.5 days for the 2010 flight). Cryogens were depleted 12 days and 12 hours into the flight, so for the last 3.5 days of the flight no science data was taken. The altitude over the course of the flight is shown in Figure 3.4.

3.4.1 TDRSS Transmitter Noise

Upon reaching float altitudes and biasing the detectors there was a large component of level shifting noise seen in the science and dark bolometers similar to the 2010 flight. This time however the detectors also saw a time varying signal, which appeared to be a bright source, except it was seen by all detectors simultaneously (Figure 3.12). Upon switching off the NASA TDRSS transmitters the level shifting noise and spurious signal dissapeared.

It is quite likely that this apparent RF noise leakage from the TDRSS was the source of much of the 2010 correlated noise. In 2010 the large synchronous TOD

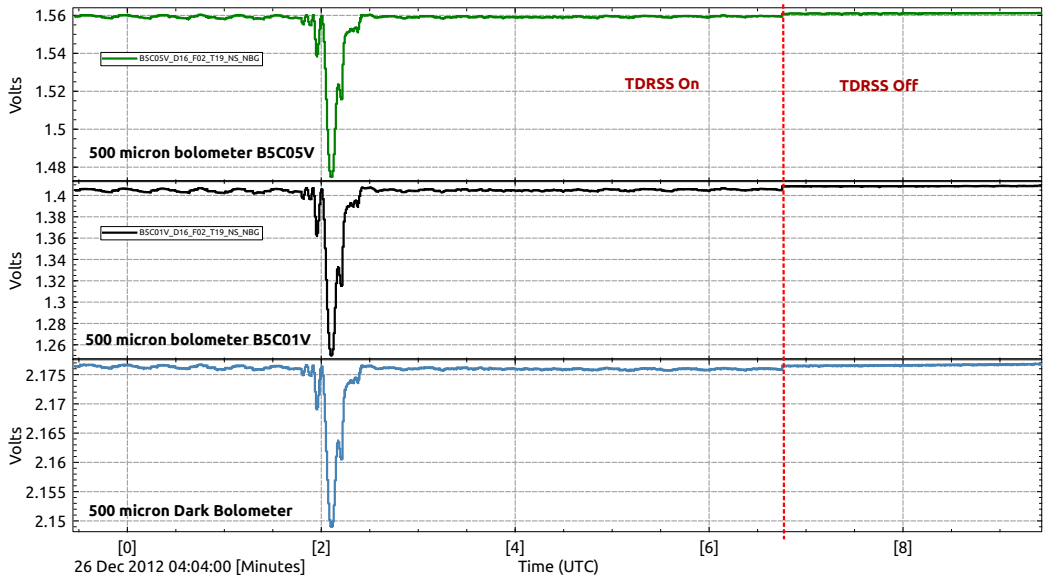

Figure 3.12: BLASTPol TOD for two science detectors: B5C05V (central 500μm bolometer) and B5C01V (500μm bolometer on the edge of the array) and a 500μm dark detector both before and after the TDRSS transmitter was turned off. TDRSS transmission appears to have been causing level shifting noise in the bolometers, as well as an occasional large TOD feature (approximately two minutes into the plot).

feature shown in Figure 3.12 was not observed, perhaps because of different mounting postions of the TDRSS antennae.

To compensate the TDRSS transmitters were powered off for the remainder of the flight. Telescope downlink was sent over the lower bandwidth Iridium platform.

3.4.2 Double Reboot Early in the Flight

At 32.3 hours after launch control of the telescope was temporarily lost when both flight computers crashed and were rebooted by the watchdog circuit. This was during the sending of a command to use a new schedule file created out of a schedule file library on board the flight computers. It is quite possible then that a software bug in the schedule file code caused the crash.

3.4.3 Star Camera Performance

The boresight star cameras did not perform optimally in 2012. There were many false 'stars' near the edge of the star camera field of view that were likely caused by dust specks on the camera CCDs. These false stars were especially problematic at low telescope elevations. The star cameras were able to get frequent solutions on fields with bright stars (such as Lupus I). For some other fields the cameras would only return a few solutions per raster scan.

For the first time in the 2012 flight the star camera computers flew solid state drives instead of conventional hard drives. Solid state hard drives can operate in near vacuum, so that even if the star camera pressure vessels leaked the computers would still be able to function. In 2010 solid state hard drives were flown as the flight computer data storage units and there were no problems.

Unfortunately the particular model flown, Intel 320, appears to have had severe problems with float conditions, likely due to the increase in cosmic ray flux in the

stratosphere. Both star camera hard drives failed: one drive failed 6.06 hours after launch and the other failed 6 days, 0.58 hours after launch.

3.4.4 BLASTPol 2012 Observing Strategy

Early observations for BLASTPol 2012 were similar to those taken in 2010. (Observations are listed in Table 5.1.) The plan for the flight was to observe mostly the same targets as in 2010 but without the systemmatics from the melted filter, with better referencing and crosslinking. The observations started with targets in the fourth Galactic quadrent (Puppis and Vela), and moved on day five to observe targets near the inner Galaxy (Lupus).

The loss of both boresight star cameras six days after launch required a change of observational strategy. Without the boresight star cameras post flight pointing reconstruction is difficult. The roll star camera on the outer frame and gyroscopes can be used to reconstruct telescope azimuth, and it was hoped that a combination of the elevation encoder, tilt information from the DGPS and inclinometers could be used to reconstruct the telescope elevation to $\sim 1'$.

After the star camera failures, mapping switched to two surveys:

- *Vela Large Polarization Survey:* The primary survey was a box of $2^\circ \times 6^\circ$centered on the Vela C cloud, with a goal of providing sensitive polarization maps of the more diffuse cloud regions around Vela C. The scan was set up so that it crossed the bright Vela C cloud on every azimuth crossing. The bright structure in the bolometer TOD can hopefully be used to further refine the telescope pointing.

- *Puppis Large Survey:* When the Vela C was not visible a very large region in the Puppis constellation (116 deg^2) was observed. Puppis is not as bright as Vela C so the bolometer TOD may not be useful to constrain the pointing, however the pointing should be good enough to produce an I map at 250, 350 and 500μm

with $\sim 2'$ resolution, which can be used to probe both the cloud structure and ISM dust properties.

3.4.5 BLAST2012 Data Quality

Overall the data quality for the BLASTPol 2012 flight is much better than the 2010. Putting the reciever electronics on a completely different power circuit than the motors and turning off the TDRSS transmitters removed the large correlated noise component.

As disscussed in Section 5.2.2 the beamshape still appears to be elongated, but so far there seems to be no evidence of significant instrumental polarization of the kind that was quite prevalent in the 2010 data. In addition, careful measurements were made of several point source calibrators with good source coverage at each HWP angle. Thus unlike for the 2010 flight data we should be able to properly characterize the telescope beam.

However, the failure of both star camera hard drives means that the pointing solution after the first six days of the flight will be limited to $\sim$1 arcmin. Using the roll star camera mounted on the outer frame, and a combination of the gyros, tilt sensors and elevation encoder plus our knowledge of where the bright structures are located in the map may be enough to produce a coarse resolution ($\sim 2'$) polarization map of Vela C and surrounding areas.

Chapter 4

BLASTPol 2010 Analysis Pipeline and Simulations

4.1 Chapter Overview

BLASTPol makes large (several deg^2) maps of linearly polarized dust emission across entire molecular clouds, and uses these maps to infer magnetic field morphology on scales ranging from cloud scale fields down to fields in dense filaments and cores. To do this BLASTPol needs to be able to create accurate maps of the polarization angle Φ.

Previous chapters have given detail on the instrument (Chapter 2), including a description of the polarimeter in Section 2.4, and flight performance (Chapter 3). The purpose of this chapter is to show that BLASTPol can be used to reconstruct polarization direction, using both simulated observations and actual data from the BLASTPol 2010 flight.

In Section 4.2 the observations and data pathologies are presented. The BLASTPol 2010 flight had several problems with the instrument which resulted in a polarized non-Gaussian beam, significant instrumental polarization and additional highly correlated bolometer noise. The data reduction pipeline and instrumental polarization correction

methods are discussed in Section 4.3. In Section 4.4 a series of internal consistency tests or "null" tests are described which are used to test which polarization pseudovectors are likely contaminated by systematics. Finally in Section 4.5 I give an overview of *simsky*, software which generates simulated BLASTPol time ordered data (TOD) that can include correlated and uncorrelated noise, instrumental polarization and effects due to a polarized non-Gaussian beam. Using *simsky* I show that the BLASTPol data pipeline can measure instrumental polarization and reconstruct input polarization maps.

The intention is that this chapter will later be adapted into a paper on the BLASTPol polarization reconstruction methodology. A more thorough description of the instrumental polarization determination and null test code can be found in T. Matthew's thesis (Matthews 2013). Some of the formalism for the polarization reference frame conversion in Section 4.5.1 was adapted from Novak (2010).

4.2 Dataset and Pathologies

The first BLASTPol science campaign took place from December 27th 2010 to January 6th 2011. BLASTPol was launched from McMurdo Station, Antarctica and traveled over continental Antarctica at an altitude $>$37km (above 99.5% of the atmosphere) before terminating over the Ross Ice Shelf. For more details on the flight see Section 3.2.

Observations from the 2010 flight are summarized in Table 4.1. The 2010 dataset had many serious issues. These include:

- Large instrumental polarization, which varies from detector to detector;
- A non-Gaussian and polarized beam shape;
- Additional noise that is highly correlated noise across all detectors;

- Poor coverage of off source regions where we might expect the sky flux to be negligible, which could be used to estimate zero point flux levels for our I, Q and U maps (Section 3.3.1).

Table 4.1 gives a comparison between the time spent observing each target and the time used in making the 2010 maps. The last four columns list the faction of the time used in the final maps at each of the four half wave plate (HWP) positions (0°, 22.5°, 45.0°, 67.5°). For the two primary BLASTPol science targets Lupus I and Vela C, a large portion of the data was rejected by the data reduction pipeline. Most of the flagged data was rejected because of severe anomalous correlated noise described in the next subsection. For Vela C, which was observed early in the flight, a number of scans were rejected because of poor telescope pointing control resulting in the telescope executing large loop-like patterns on the sky. The rapid elevation changes in the these scans caused extra features in the TOD which were problematic for the mapmaker.

The pointing calibration sources were scheduled in single raster scans at one HWP position every four to eight hours. As a consequence, the HWP angle was often the same each time the calibrator was observed. This means that these calibrators cannot be used to reconstruct the polarized telescope beam.

4.2.1 Additional Correlated Noise

During the 2010 flight it was noticed that there were large features in the TOD that were correlated across the entire array and therefore not related to astrophysical signal. These sharp features were also present in the unilluminated "dark" bolometers. The amplitude of the noise varied a great deal, but could always be seen in the correlation between dark and science bolometers. Approximately 50% of the detector samples were judged to have been so contaminated by this noise that they could not be used to make science maps.

Target Name	Type[a]	Map Area (deg^2)	Time Obs. (hrs)	Time Used (hrs)	f_0	$f_{22.5}$	f_{45}	$f_{67.5}$
Vela C	GMC	1.4	56:43:00	18.70	0.249	0.224	0.251	0.276
Lupus I	DC	0.7	48:48:30	24.98	0.254	0.250	0.243	0.253
Lupus IV	DC	0.3	13:21:30	8.86	0.258	0.225	0.269	0.249
Vela Y	MC	0.1	7:38:00	0.00	N/A	N/A	N/A	N/A
Puppis	MC	0.1	23:29:00	2.44	0.225	0.224	0.243	0.310
CarinaNeb	C, GMC	0.8	2:51:00	1.22	0.185	0.187	0.388	0.241
G331	C, GMC	0.2	2:51:00	1.94	0.220	0.261	0.219	0.299
CarinaTan[b]	GMC	1.5	13:28:25	9.54	0.260	0.250	0.274	0.185
G3219	GMC	0.5	5:01:00	4.39	0.222	0.233	0.265	0.279
G3237	IRDC	0.2	2:56:00	2.21	0.332	0.221	0.223	0.223
IRAS 08470-4243	Pt	0.1	4:54:30	2.71	0.592	0.000	0.274	0.134
VYCMa	Pt, B	0.1	1:18:00	0.33	0.000	0.000	0.000	1.000
IRAS 15100-5613	Pt	0.1	1:08:00	0.67	0.505	0.000	0.000	0.495
Cen A	Pt, G	0.1	2:25:00	0.46	0.000	0.699	0.000	0.301

Table 4.1: Information on targets observed during the 2010 BLASTPol Antarctic flight, which includes the total time spent observing each target (Time Obs.) and the amount of data which was unflagged and passed to the mapmaker (Time Used). The final four columns give the percentage of time used at each of the four HWP positions as calculated for the 500 μm bolometer B5C05V.

[a] GMC: Giant Molecular Cloud, DC: dark cloud, MC: molecular cloud, IRDC: Infrared Dark Cloud, Pt: Pointing Calibrator, C: Polarization Calibrator, B: beam shape calibrator, G: Galaxy

[b] For one scan of the Carina Tangent region an error in the HWP potentiometer readout caused the HWP to rotate to an angle that was not one of the standard positions, so for this source $f_0 + f_{22.5} + f_{45} + f_{67.5} \neq 1.0$.

Postflight two likely causes were found for this extra noise:

- The detector readout circuit and gondola were both powered by the same batteries and so shared a common ground. A clear correlation can be seen between jumps in the detector levels in the science and dark bolometers and gondola current drawn from the battery (see Figure 3.8). It appears that having the detectors and motors on the same power system led to motor switching noise leaking into the detector readout circuitry.

- During the 2012 flight it was noticed that when the TDRSS transmitter was powered a highly correlated "level shifting" noise was seen in the TOD (see Section 3.4.1). TDRSS transmission is part of the NASA telemetry system and used to transmit data to the ground station. The TDRSS transmitter was powered for the entire BLASTPol 2010 flight.

4.2.2 Beam Shape

During post-flight analysis it was noticed that the telescope response pattern, or beam shape, was highly non-Gaussian and varied both from detector to detector and with waveplate position. To reconstuct the beam shape high signal-to-noise maps of a point source are needed. Unfortunately of the observations of VY CMa, the red hypergiant star observed for this purpose, only $\sim$20 minutes of data was not rejected by the data reduction pipeline.

Instead observations of the bright compact source IRAS 08470-4243 in the Vela Molecular Ridge have been used to probe the beam shape[1]. Table 4.1 shows that the distribution in coverage of IRAS 08470-4243 at the four HWP positions is not uniform. Only the observations at HWP angles 0°and 67.5° have sufficient coverage to produce high signal-to-noise maps.

[1]Note that IRAS 08470-4243 is not really a point source. The size of IRAS 08470-4243 was found by BLAST to be approximately 40″ (Netterfield, private communication).

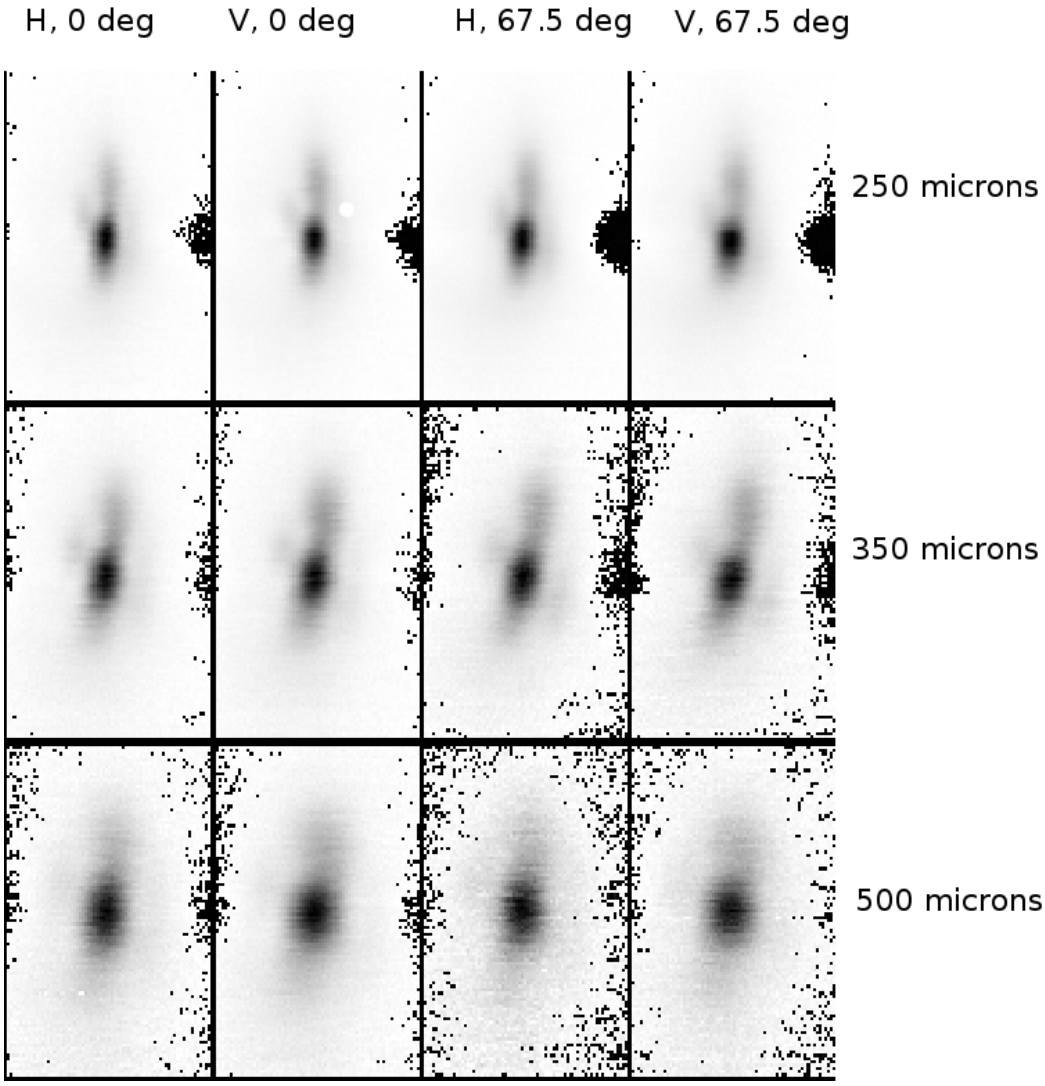

Figure 4.1: Maps of IRAS 08470-4243 at 250 (top), 350 (middle) and 500 μm (bottom). Maps are made for bolometers with horizontal (H) and vertical (V) polarizing grid orientations and for HWP angles of 0° and 67.5°. If the optics were operating as designed the sources should be round and compact. Instead a significant part of the beam power is found in an elongated halo around the main (also elongated) beam core. The shape of the beam also changes slightly between H and V bolometers and between the two HWP angles, which could imply that the beam itself has polarization structure.

Total intensity maps of IRAS 08470-4243 are shown in Figure 4.1. Four maps are presented for each BLAST band: all bolometers with horizontal (H) polarizing grid orientations and HWP angle $\Phi = 0^\circ$, vertical grid orientation (V) bolometers with $\Phi = 0^\circ$, H bolometers with with $\Phi = 67.5^\circ$and V bolometers with $\Phi = 67.5^\circ$. If the optics were operating as designed the maps should be compact and round. Instead the beam appears to have a slightly elongated core, with a highly elongated halo in the elevation direction and additional side lobes in the cross-elevation direction.

Figure 4.1 also shows that the beam varies between the two HWP positions and between the H and V bolometer orientations, which could imply that the telescope beam response itself is polarized[2].

In addition, the beam shape changes from bolometer to bolometer. Figure 4.2 shows single bolometer maps of IRAS 08470-4243 using all available HWP angle observations. The power in the main beam compared to the elongated halo varies across the array, as does the power in the cross elevation sidelobes.

In summary, for the BLAST 2010 dataset there is insufficient data to properly characterize the beam shape and polarization structure. Instead all the output maps have been convolved with a $2.5'$ FWHM Gaussian in an attempt to smooth out most of the beam structure shown in Figures 4.1 and 4.2.

4.2.3 Instrumental Polarization

The damaged IR blocking filter acted both as a partial polarizer (at the few percent level) and a partial polarized scatterer, resulting in both a polarized beam shape, and optical efficiency which depends on the polarization of the incident photon. Preflight measurements of instrumental polarization (IP), the polarization measured when

[2]The source polarization of IRAS 08470-4243 is unknown though expected to be low as bright compact sources typically show low p relative to their more diffuse surroundings (Section 1.4.3). So some of the Φ dependent structure could be due to polarization structure in IRAS 08470-4243, particularly at 250μm where the source should be resolved.

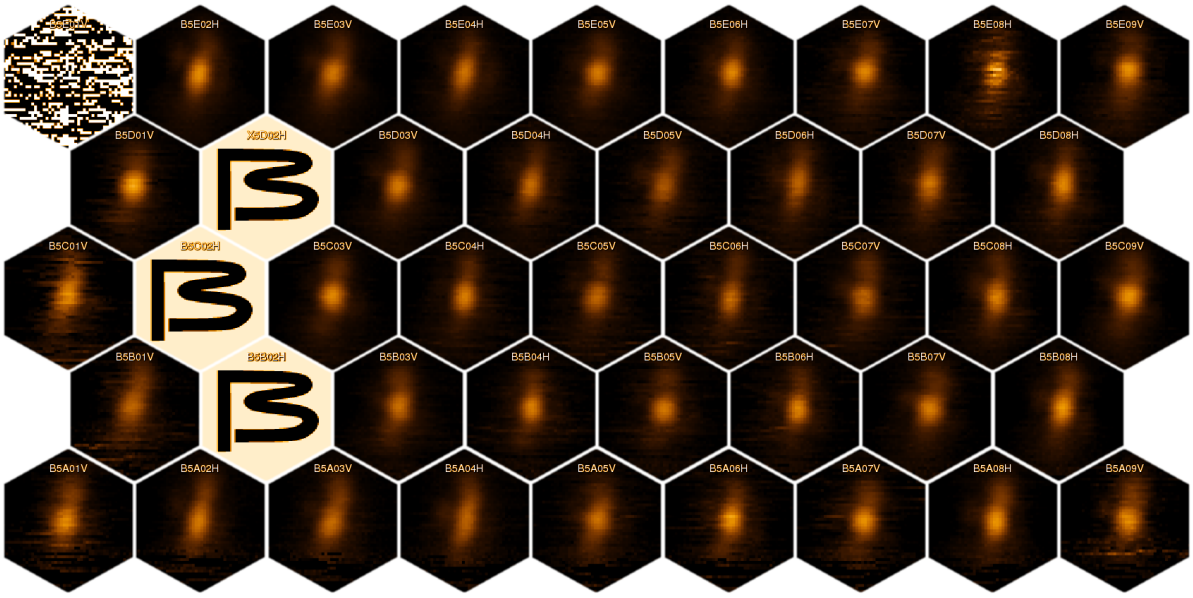

Figure 4.2: Images of the compact source IRAS 08470-4243 for every bolometer in the 500μm bolometer array. Cells marked with a *B* are broken bolometers.

observing an unpolarized source, were very small (∼0.2%). However the damage to the filter during the 2010 balloon ascent resulted in a mean IP of 5.8%, 6.0% and 6.8% for the 500, 350 and 250μm detectors respectively. Methods for identifying and removing instrumental polarization are discussed in Sections 4.3.8 and 4.3.7.

4.3 Data Reduction Pipeline

A great deal of processing is required to convert raw detector TOD into polarization pseudovectors. The TOD must be cleaned of glitches, cosmic rays and large low frequency drifts, deconvolved and correlated with sky position. The instrumental polarization must also be characterized and removed, and a mapmaker must be used to convert the processed bolometer TOD into output maps of the Q, U and I Stokes parameters.

The data reduction pipeline is summarized in Figure 4.3. Many components of the reduction pipeline have been discussed in greater detail elsewhere and are referenced

where appropriate.

TOD are organized into *dirfiles*. Each TOD, whether a raw detector, or the elevation calculated by the pointing solution software, is saved as an individual file, with a common starting and ending time. In this way both raw data and data products can easily be viewed, compared and processed simultaneously.

4.3.1 Data Merger

An almost complete set of flight data is recorded on each of the two redundant flight computers *north* and *south*. Gaps in the dataset correspond to when a computer was in the process of rebooting.

The first task of the data reduction is to take the separate datasets and create a merged canonical dataset which can be used as a reference for all subsequent steps in the data reduction process. When both computers are running in nominal configuration and recording data there should be no difference whatsoever in the TOD. This has been spot checked by plotting the same bolometer TOD recorded on both computers as a function of time, subtracting the difference and looking for a residual. For every check made the residual was identically equal to zero.

To merge the datasets, dirfiles files were created for the data on each flight computer. Then a merged dataset was created by appending the individual dirfile channels together to create a continuous dataset, using the data from the in charge flight computer. For the 2010 dataset there is a 30 second gap in the merged dataset when both flight computers rebooted at the same time. (This event is discussed further in Section 3.2.10).

Once the dataset was merged a detailed annotated observation log was created. Data index ranges for scans of individual targets were identified, these were later used to choose the data used to make the science maps.

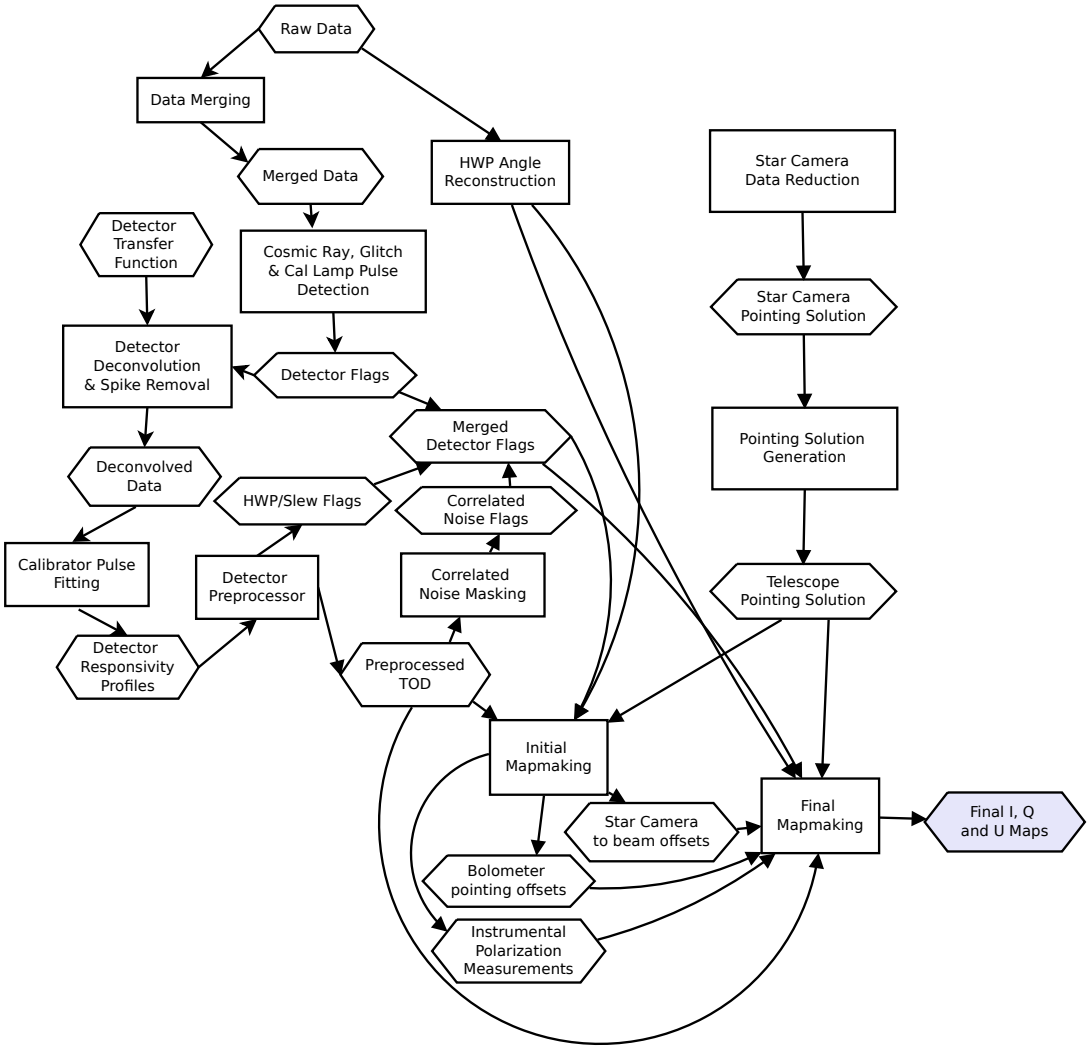

Figure 4.3: Block-level diagram of the BLASTPol 2010 data reduction pipeline. Rectangles represent data reduction operations, hexagons represent data products.

4.3.2 Despiking and Deconvolution

The next step in the data reduction is the identification of short term corruptions in the data which may be caused by:

- *Cosmic rays*, which deposit power on the bolometers;
- *Glitches* arising from the errors data acquisition system readout;
- *Pulses from the calibrator lamp*;
- *Features from rotation of the HWP*.

First glitches are identified and removed. Glitches are typically only one sample ($\sim$0.01 s) long, and are found by calculating the difference between consecutive detector samples. If the difference is $>$0.0005 V the sample is flagged. For most bolometers no glitches were found. Only 10 bolometers had more than ten glitches for the 2010 flight.

Cosmic rays spikes are caused by cosmic rays either hitting a detector (single) or striking somewhere on the 300 mK stage and causing the detectors to heat temporarily (multiple). Multiple cosmic ray spikes are more common than single cosmic ray spikes. The spikes are found by high-pass filtering the detector TOD to remove all signal associated with the telescope scanning of astrophysical signal, and masking out anything four times larger than the TOD noise level.

For the 2010 flight an average of 153 minutes of data was identified as cosmic ray contaminated. Because some cosmic rays that affect all bolometers may be masked by noise features in the data the despiking code also keeps a count for each 0.01 s sample of how many bolometers were flagged as cosmic rays. If a particular sample was flagged for more than 10% of the detectors the sample is flagged for all detectors in that frequency band.

Pulses from the calibrator lamp are used to correct for the changing responsivity of the detectors but should be removed from the science bolometer TOD. The calibrator lamp pulses for 300 ms every ∼15 minutes. In total 26 minutes of data was flagged as calibration pulses over the 2010 flight.

Once a set of flags has been produced for each detector, the bolometers can be despiked and deconvolved. The deconvolver takes as input a set of flags and a bolometer transfer function determined by the makeup of the readout electronics. First, the glitches are removed so that they do not cause ringing in later stages when the data is Fourier transformed. The corrupted data sample is replaced by an average of the adjacent detector samples. Next the data is deconvolved by dividing the Fourier transform of the data with the bolometer transfer function. Then finally the flagged data are removed and the gap is filled with a combination of a linear interpolation between the adjacent unflagged data, and white noise characteristic of the bolometer being cleaned. This process is described in more detail in Angile (2013). Examples of cosmic ray removal (top panel) and calibrator lamp pulse removal (bottom panel) from bolometer TOD are shown in Figure 4.4

4.3.3 Calibrator Pulse Corrections

The responsivity of the detectors changes over the course of the flight. To correct for this the calibration lamp (Section 2.3.2) is flashed approximately every 15 minutes for 300 ms. The power outputted by the calibration source is essentially constant, so the variation in the amplitude of the calibrator pulse measured by the bolometers is a linear measure of the bolometer responsivity.

Figure 4.5 shows the amplitude fit to a template pulse profile for every calibrator lamp pulse in the BLASTPol 2010 flight. The fitting procedure is discussed in detail in Angile (2013). There is a systematic offset between the pulse amplitude at different HWP positions, most notably a ∼3% difference between the amplitude at $\Phi = 0^\circ$

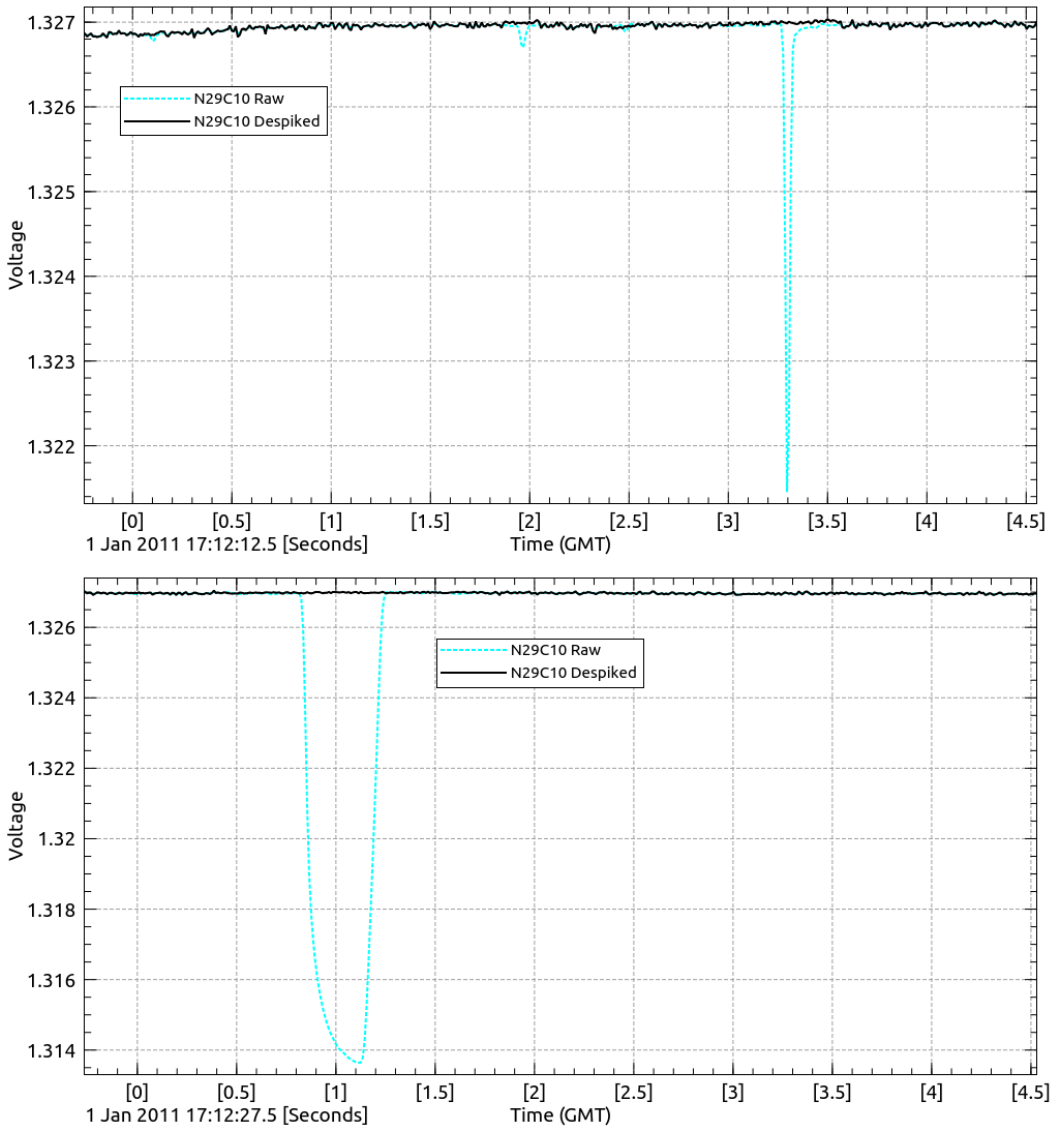

Figure 4.4: Example of cosmic ray removal (top) and calibration lamp pulse removal (bottom) for the detector N29C10. The ”raw” detector TOD are shown with dashed cyan lines and the deconvolved and despiked data are shown with solid black lines.

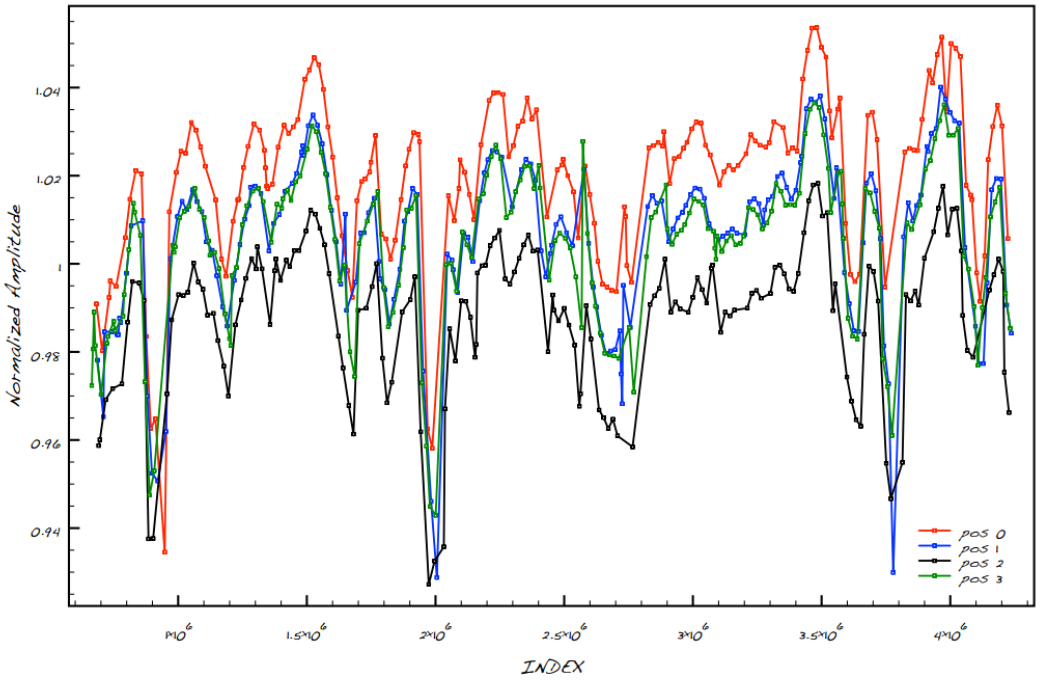

Figure 4.5: Amplitude fit to each of the calibrator lamp pulses, tracing the change in responsivity of the detectors over the 2010 flight (Angilè 2011). One data index corresponds to 0.2 seconds. Four lines are plotted, one for each HWP position (red: $\Phi = 0°$, blue: $\Phi = 22.5°$, black: $\Phi = 45°$, green: $\Phi = 67.5°$).

and $\Phi = 45°$. Given the observed levels of instrumental polarization it is expected that the fraction of light transmitted by the damaged infrared blocking filter depends on the polarization of the incident radiation. Figure 4.5 would then imply that the changes in transmission are large enough to affect the loading of the detectors, which in turn affects the responsivity of the detectors as measured by the calibrator lamp.

4.3.4 Preprocessing TOD

Before the map making stage the detectors are preprocessed. The goal of the preprocessor is to remove long timescale drifts, reduce spurious signals associated with rapid changes in telescope elevation and produce a set of approved frame ranges for each scan which exclude data contaminated by telescope slews and HWP rotation.

First the data is divided up into data "chunks", which consist of a complete raster scan up and down with the HWP postion fixed at one of a set of four positions. Typically the scan parameters were set so that a single data chunk corresponds to approximately 15 minutes worth of data. The data chunk beginning and end points are defined by either a telescope slew to a new target or a stepping of the HWP. Both telescope slews and HWP movement cause heating of the detectors which results in large features in the bolometer TOD, so an additional 10 seconds of data after a slew and 46 seconds after a HWP move are removed from the data chunks. After preprocessing 13% of the data was flagged, mostly due to HWP moves.

One property of the bolometer TOD is that there is a clear correlation between telescope elevation and TOD features. This is particularly visible during elevation turnarounds which can clearly be seen in many cases in the bolometer TOD (for an example see the left panels of Figure 4.7). This elevation correlated signal is likely partially due to variations in atmospheric column with telescope elevation, however it is also known that sudden changes in elevation cause heating of the detectors (even with the telescope closed to light) so a part of the elevation correlated signal may be due to the motions of cryogens.

For every chunk and for each individual bolometer, a function was fit to six seconds of data around the elevation direction change at the top of the raster scan[3]:

$$D(t) = a_i + b_i\, t + c_i\, (\epsilon(t) - \epsilon_\circ) \tag{4.1}$$

where ϵ is the elevation of the telescope, and $\epsilon_\circ$ is the elevation at the start of the data range being fit.

The c_i coefficients vary considerably from bolometer to bolometer and also as a function of elevation. Figure 4.6 shows the coefficients for several bolometers (black X

[3]During the 2010 flight the pointing was not always stable due to the reaction wheel not functioning properly, so there are number of occasions where the telescope would scan well off the target. To compensate I only fit data chunks with one elevation turnaround.

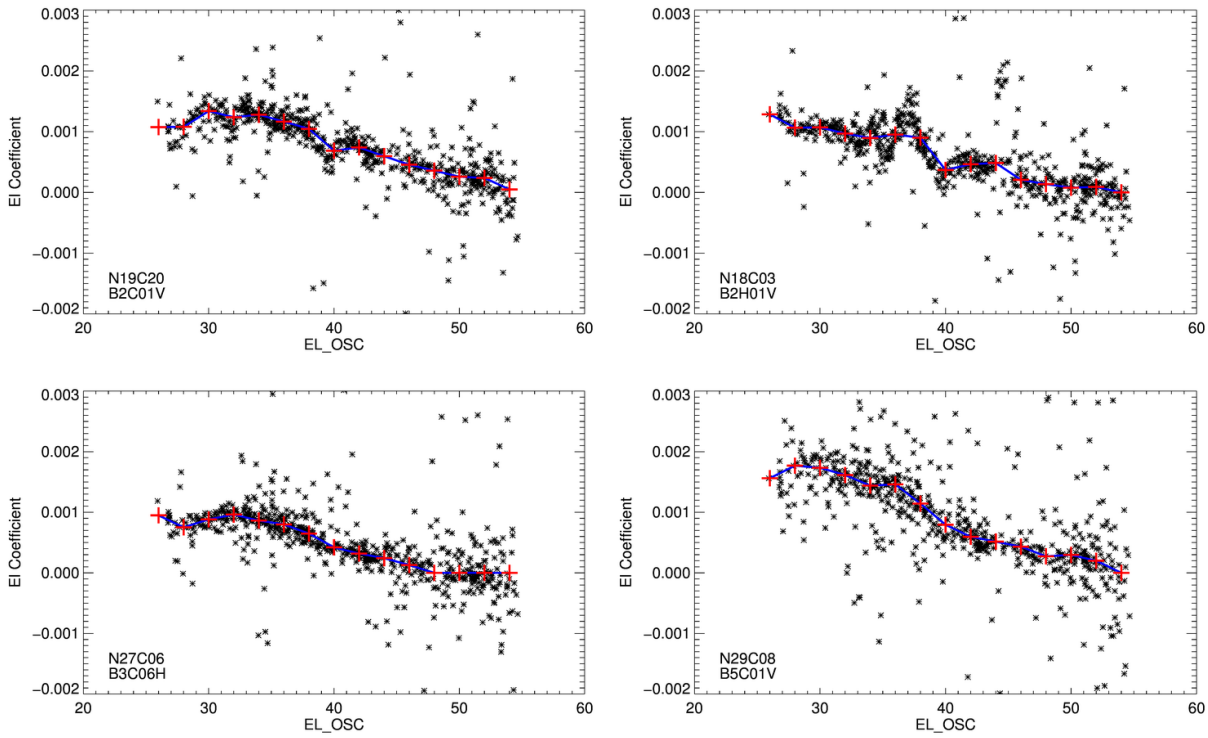

Figure 4.6: Elevation correlation coefficients (c_i) for 250 μm detectors B2C01V (top left), B2H01V (top right), 350 μm detector B3C06H (bottom left) and 500 μm detector B5C01V (bottom right). Black 'X's are individual c_i coefficients fit to each data chunk. Red plus signs are the median of all c_i coefficients c_m within two degree bins, and blue shows the linear interpolation between c_m coefficients.

symbols) as a function of elevation. The elevation coefficients were divided into two degree bins of elevation and a median coefficient c_m was found for each bin (red plus signs in Figure 4.6). The preprocessor then subtracts the following function from each data chunk:

$$D'(t) \;=\; D(t) \;-\; c(\epsilon)\;(\epsilon(t) - \epsilon_\circ) \tag{4.2}$$

where $D(t)$ is the orginal TOD, $D'(t)$ is the elevation corrected TOD, $\epsilon_\circ$ is the elevation at the beginning of the data chunk, and $c(\epsilon)$ is a linear interpolation between the median elevation coefficients (blue lines in Figure 4.6).

Long timescale drifts can cause leakage into other Fourier modes. To remove these

low order modes a least-squares 7th order polynomial was fit and then subtracted from $D'(t)$ for every data chunk in each bolometer. The end points of the preprocessed data chunk are constrained to be zero by subtracting a line fit between the average of the first 0.5 seconds of the data chunk and the last 0.5 seconds of the data chunk.

Figure 4.7 shows the preprocessed TOD both without (black) and with (colour) subtraction of an elevation correlated term for three different bolometers.

4.3.5 TOD Inspection and Additional Flagging

As discussed in Section 4.2 an additonal source of noise was seen in the bolometer TOD characterized by rapid jumps in bolometer DC level. This noise was likely due to motor switching noise and radio frequency noise pickup from the NASA TDRSS transmitters which are used to communicate with the telescope.

To identify this level-shifting noise each bolometer was correlated with a dark bolometer on the same array. The dark bolometers are blocked from recieving light but are read out identically to the other bolometers. The level shifting noise is highly correlated across all bolometers (both science and dark) (see Figure 3.8). Data chunks with particularly high dark/science bolometer correlations were flagged as bad (Matthews 2013). After flagging for correlated noise, 44% of the 2010 data was marked unusable.

The correlated noise component was present over the entire flight, but the severity of the noise varied. Some targets were more affected: for example all of the 7.6 hours of Vela Y data were flagged (Table 4.1). It is noticable that many of the smaller maps, where time between scan turnarounds and therefore motor current spikes is small, had most of their data flagged due to correlated noise. It is also possible that there were several telescope orientations for which the reflection of TDRSS transmissions off the inner frame sunshield to the cryostat window was optimal.

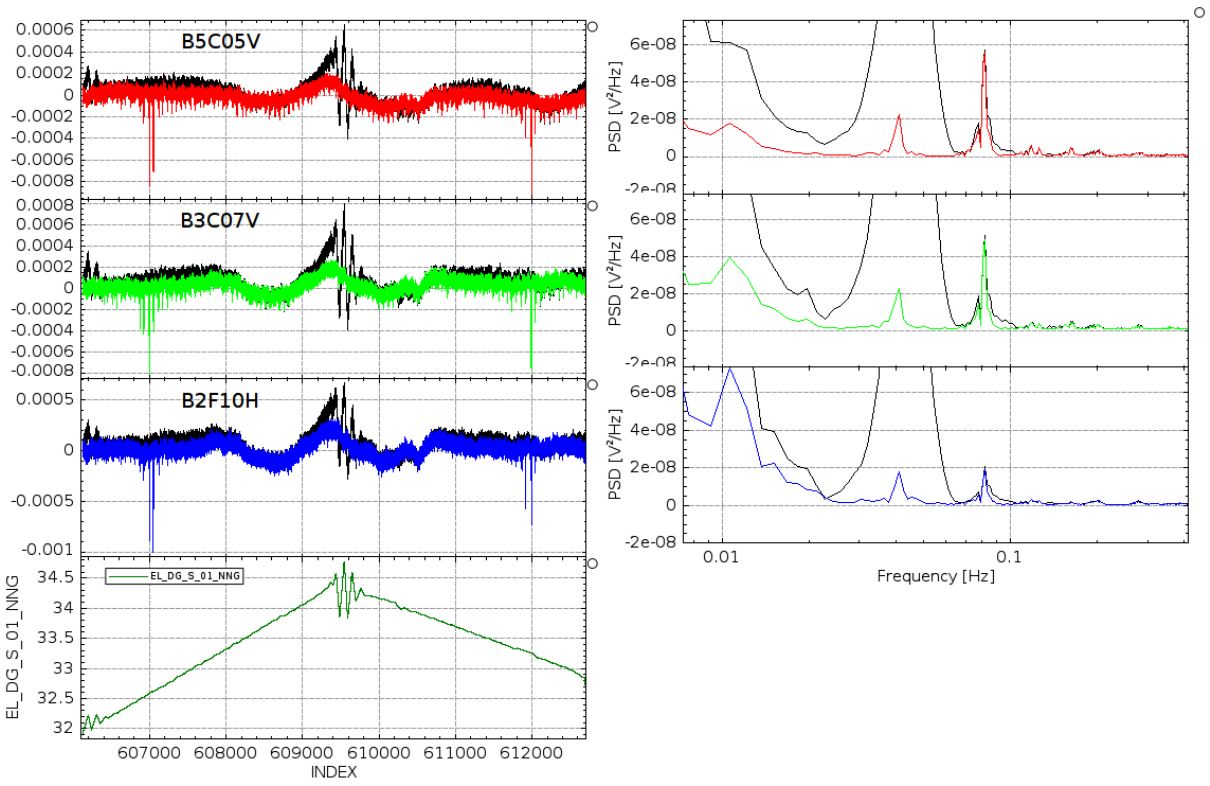

Figure 4.7: Examples of preprocessor subtraction for three different bolometers. *Left:* Examples of preprocessed TOD for a 250μm bolometer (blue), a 350μm bolometer (green) and a 500μm bolometer (red). The black curve in each plot shows the preprocessed TOD if an elevation correlated term is not subtracted, and the coloured curves show the preprocessed TOD including subtraction of elevation correlated terms. The bottom plot shows the telescope elevation for comparison. *Right:* Power spectra for the preprocessed TOD in the corresponding left panels.

In addition single bolometer I maps were made for each data chunk. The maps with signficantly higher than average noise were rejected.

4.3.6 Pointing Solution

In order to make science maps a high quality telscope pointing reconstruction with errors $<5''$ is required. During the 2010 flight the in-flight pointing solution was generally good to $30''$ (Angilè in press).

Post-flight pointing reconstructions were made iteratively, using previous star camera solutions and gyroscope data to obtain additional star camera solutions. The reconstruction algorithm is described in detail in (Pascale et al. 2008). The offset between the star cameras and the submm telescope was measured by repeated observations of compact structures with known sky coordinates throughout the flight. The location of the submm beam relative to the star camera axis is known to be a function of elevation, requiring corrections to pitch and yaw spanning $\sim 120''$ and $\sim 190''$ respectively. Post-flight absolute pointing accuracy using this system is typically $< 2''$, with random pointing errors of $< 3''$ rms (Pascale et al. 2008).

4.3.7 Mapmaking

The BLASTPol mapmaker *naivepol* takes in time ordered data including preprocessed detector TOD, the post-flight pointing reconstructed from gryoscope and star camera data, the HWP angle measured from the shaft encoder, and a set of data flags and produces estimates for the sky signal in I, Q and U for each pixel in a map.

Details of *naivepol* are discussed in (Moncelsi et al. 2012). In brief the mapmaker assumes that the noise properties of the detectors are uncorrelated and white, at least on the timescale of the scans. It then performs a weighted binning of the data TOD into map pixels, with the weighting given by the inverse of the the timeline variance measured from the white noise floor.

Because the BLASTPol detectors have a significant low frequency (1/f) noise component, the input TOD were high-pass filtered with a frequency of 0.05 Hz in order to "whiten" the noise spectra. This means that any cloud features on scales larger than

$$\theta = \frac{\omega_{scan}}{0.05\,Hz} \tag{4.3}$$

(where ω_{scan} is the scanning speed) were filtered out of the TOD. During the 2010 flight the scan speed was typically $0.05\,^{\circ}/s$, so any signal on scales larger than a degree is not present in the output maps. (Typical map sizes are of order a degree in width). The filtering also causes the maps to have a zero net mean and can cause large sections of the map to have negative features. This is problematic for the reconstruction of polarization pseudovectors, so for calculations of the percentage polarization p and the polarization angle Φ I, Q and U values have been made relative to defined reference regions so that $I = I_{map} - I_{ref}$, $Q = Q_{map} - Q_{ref}$ and $U = U_{map} - U_{ref}$. Essentially this fixes the flux zeropoint of the maps to the mean of the reference region.

Reference regions are chosen to have good map coverage and little dust column (inferred from previous submm observations, or dust extinction maps). To avoid including pseudovectors for which the uncertainty in reference region flux could significantly affect the I, Q and U photometry an intensity cut is applied to all pseudovectors requiring the unreferenced flux $I_{map} > 0.2 I_{ref}$.

The reference region method doesn't allow the reconstruction of any other large scale modes lost due to filtering. A more sophisticated mapmaker which accounts for correlated noise is under development and will be used in the BLASTPol 2012 data analysis.

To be sure that there is even coverage of all polarization angle components, an equal number of bolometers with horizontal polarizing grid angles (H) and vertical grid angles (V) are used to make *naivepol* maps. Since there were more functioning V bolometers than H bolometers, several V bolometers at the edge of the array were not

used in making maps. In total 124, 74 and 36 bolometers were used at 250, 350 and 500 μm respectively.

4.3.8 Instrumental Polarization Determination

Instrumental polarization was measured using sky rotation. The source, and therefore the source polarization angle, rotates relative to the telescope reference frame as it rises and sets while the instrumental polarization stays fixed in the telescope reference frame. Observations of Vela C, a bright molecular cloud with excellent map coverage, were used to calculate the IP. The Vela C observations were divided into two parallactic angle bins with a mean angle between the two bins of 8.5°. A source aperture was defined around the brightest pixels in the I map (as shown in green contours in Figure 4.8a). For each bolometer mean values of $q = Q/I$, $u = U/I$ were calculated for the source aperture from the data in each parallactic angle bin. The I, Q and U maps require a low flux reference region which is covered by all bolometers (red contours in 4.8a).

Green crosses in Figure 4.8b show the measurements of q and u in the Vela C source aperture for each detector in the 500μm array. Each pair of measurements from the two parallactic angle bins are connected with a red line segment. If BLASTPol had no instrumental polarization the q and u measurements would lie on q_{sky}, u_{sky}. Instead the q and u values include a significant IP term, which rotates about a circle centered on q_{sky}, u_{sky}. From this data both the instrumental polarization terms and the mean source polarization q_{sky}, u_{sky} can be reconstructed. The q_{ip} and u_{ip} terms for each bolometer are plotted in Figure 4.8c and the mean instrumental polarization levels $\bar{q}_{ip}$, $\bar{u}_{ip}$ and $\bar{p}_{ip}$ calculated for each band are given in Table 4.2.

As an additional consistency check the post IP subtraction BLASTPol maps of G331.5-01 and the Carina Nebula were compared to previous observations made by the SPARO telescope (Li et al. 2006). Direct comparisons between BLASTPol and SPARO

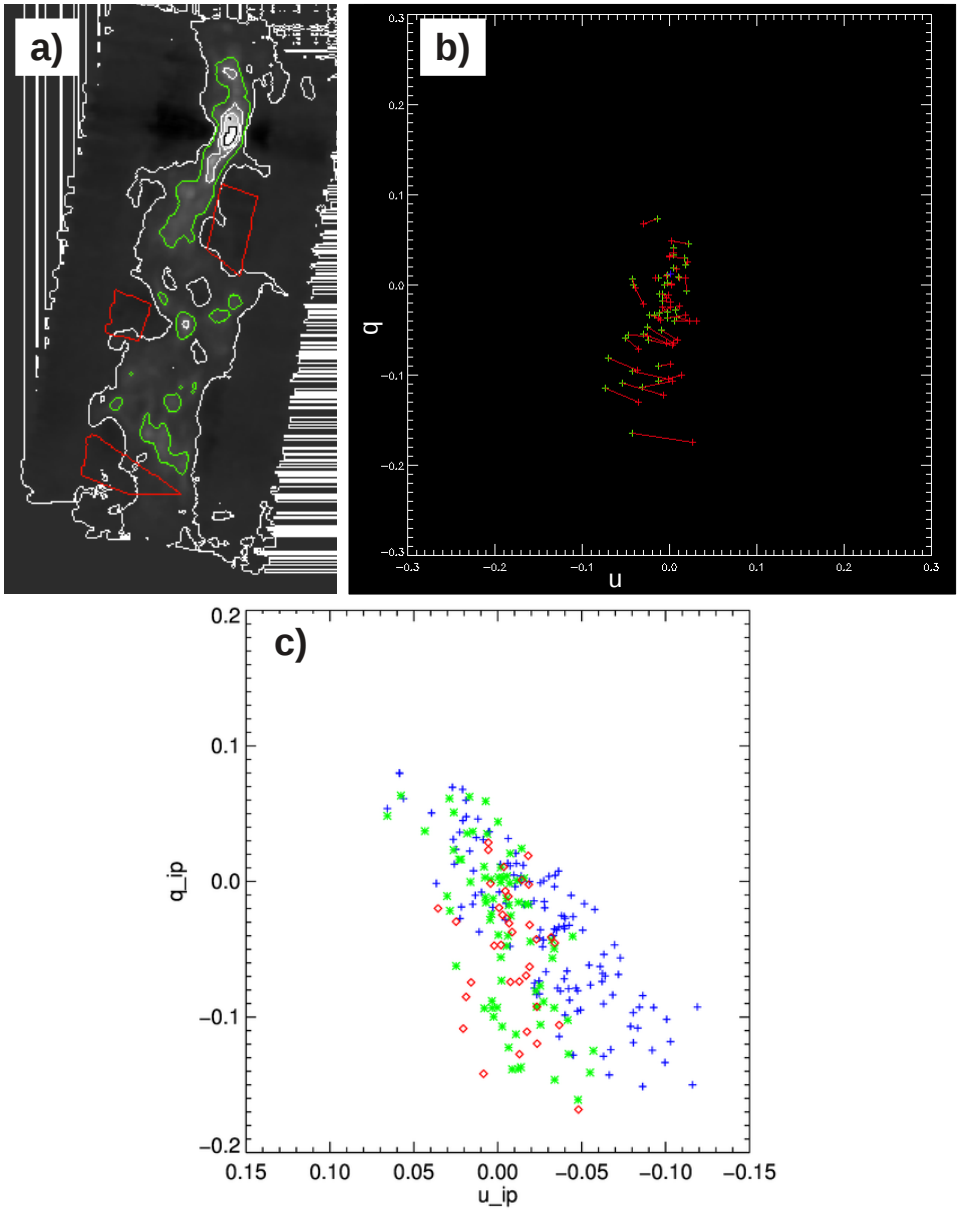

Figure 4.8: Instrumental polarization of the 500 μm detectors as measured using sky rotation of the polarization of the Vela C molecular cloud. *a)* An intensity map of Vela C smoothed with a 2.5′ FWHM Gaussian. The source apertures are marked with green contours and reference regions used in the IP determination are marked in red. *b)* q and u calculated for the Vela C data divided into bins based on parallactic angle (green + signs) for each 500 μm bolometer. The measured polarization rotates about the mean source polarization (blue + sign). *c)* q_{IP} and u_{IP} terms for all bolometers (red diamonds= 500 μm, green x=350 μm, blue + =250 μm).

Wavelength	$\bar{q}_{ip}$	$\bar{u}_{ip}$	$\bar{p}_{ip}$	N_{bol}
250 μm	-0.034	-0.028	0.068	124
350 μm	-0.036	-0.004	0.060	74
500 μm	-0.050	-0.008	0.058	36

Table 4.2: Mean instrumental polarization calculated from sky rotation of Vela C for each of the three BLASTPol bands. The last column lists N_{bol}, the number of bolometers used by the mapmaker in each band.

maps are complicated because SPARO is a chopped experiment which measures polarization relative to a chop throw of $\pm 1^{\circ}$ in the right ascension direction. BLASTPol measures polarization relative to selected reference regions, but the BLASTPol 2010 maps were not large enough to use the SPARO chop throw regions as reference regions. Even so the BLASTPol polarization pseudovectors in the Carina Nebula match the orientation of the SPARO vectors very well. Figure 4.9 taken from Matthews (2013) shows the inferred magnetic field direction derived from 2010 observations of the Carina Nebula, compared to similar measurements from SPARO.

IP reconstruction was tested using simulated BLASTPol observations as discussed in Section 4.5. The simulations were able to reconstruct IP to $\sim$0.5%. For this reason we only report pseudovectors which have $p > 1.5\%$. For G331.5-01 SPARO measured a polarization percentage in the brightest part of the cloud of $<$0.3%. The BLASTPol 2010 map of the cloud gives a percentage polarization of 0.8%, which is consistent with the uncertainty in the instrumental polarization (Matthews 2013).

4.4 Null Tests

As discussed in Section 4.2 the BLASTPol observations are marred by solar damage to an infrared blocking filter during launch. The damaged filter acted as both a partial

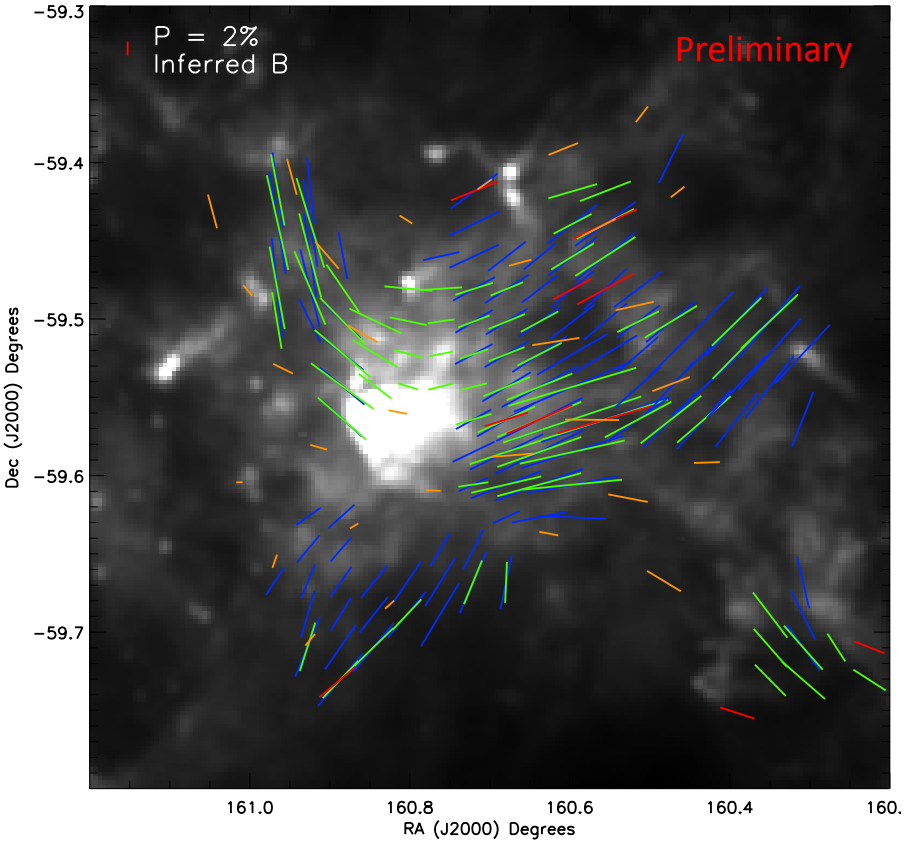

Figure 4.9: BLASTPol 2010 observations of the Carina Nebula smoothed to a resolution of 2.5′ plotted over a grayscale Herschel 350 μm map, with a pseudovector spacing of 2.5′. The pseudovector orientation gives the inferred direction of the magnetic field projected on the plane of the sky. Only pseudovectors which pass the null tests described in Section 4.4 are shown. The BLASTPol observations at 250 μm (blue), 350 μm (green) and 500 μm (red) show good agreement with the field direction measured by the SPARO telescope (orange lines) (Li et al. 2006). From Matthews (2013).

polarizer and a partial polarized scatterer. Under these circumstances errors are more likely to by dominated by systematics due to instrumental polarization, polarized sidelobes, or a polarized beam shape than statistical errors.

In order to characterize which polarization measurements are robust and repeatable the data was put through a series of internal consistency checks referred to as *null tests*. For each test, the data was divided into two groups with an equal number of samples in each group. A set of I, Q, and U maps were then generated for both groups. From these residual maps Q_{res} and U_{res} were calculated:

$$Q_{res} = Q_a - \frac{Q_a + Q_b}{2} = \frac{Q_a - Q_b}{2}, \tag{4.4}$$

$$U_{res} = U_a - \frac{U_a + U_b}{2} = \frac{U_a - U_b}{2}. \tag{4.5}$$

If there are no systematic differences between the data in groups a and b, then the difference maps should show only noise. If however, there are systematic differences in the data in groups a and b then structure may be visible in the residual maps.

An individual pseudovector only passes a null test if the magnitude of the polarized flux in the residual maps is less than a third the magnitude of the combined polarized flux in Q and U maps made with all the data:

$$\sqrt{Q^2 + U^2} > 3\sqrt{Q_{res}^2 + U_{res}^2}. \tag{4.6}$$

For each science target the pseudovectors with $p > 1.5\%$ and $I > 1.2 I_{ref}$ were put through a series of six null tests. The results of these tests are summarized in Table 4.3 and Figures 4.10 and 4.11 show the pseudovectors which passed each null test for the 350 and 500 μm arrays respectively for BLASTPol observations of the Lupus I dark cloud (Matthews et al. 2013).

To be used in the final science map a pseudovector must pass all six null tests. Note that none the 250 μm polarization pseudovectors passed all six null tests. However a total of 29 pseudovectors at 500 μm and 25 pseudovectors at 350 μm pass all six consistency tests.

Test Name	Type	N_{pass} 500	N_{pass} 350	N_{pass}250
Parallactic Angle	Temporal	42	49	17
Early/Late	Temporal	55	65	69
High/Low Elevation	Temporal	65	70	68
Top/Bottom bolometers	Spatial	36	54	26
Left/Right bolometers	Spatial	33	41	14
High/Low IP bolometers	Spatial	57	57	14
Total	Combined	29	25	0
H/V bolometers[a]	Spatial	13	11	19

Table 4.3: Results of the null tests for observations of Lupus I. The tests were performed for all pseudovectors with $p > 1.5\%$. Only pseudovectors that pass all six null tests were used in scientific analysis.

[a] Pseudovectors are not required to pass the H/V bolometer consistency test.

It is important to note that pseudovectors may fail these tests for reasons other than experiment systematics. Noise peaks which happen to add constructively in equations 4.4 and 4.5 can lead to a pseudovector failing a null test. Similarly it is possible for pseudovectors which are contaminated by beam systematics to pass a null test if noise spikes lower Q_{res} or U_{res}. By requiring that the vectors pass a large number of tests it is hoped that the latter case will be caught.

4.4.1 Temporal Null Test Results

Parallactic Angle: Changing the parallactic angle rotates the sky signal relative to telescope coordinate system. Thus this test is sensitive to systematics introduced by polarized structure in the beam including polarized side lobes. For the Lupus I and Vela C maps the median difference between the parallactic angle in the two bins was 8.5°.

Elevation: The data was divided into high/low telescope elevation bins. It is known from previous BLAST flights that the angle between the central bolometer in the bolometer detector arrays and the boresight star camera axes changes as a function of elevation. A pointing offset correction is calculated after every ∼15 minute scan. However, the elevation null test can be used to look for spurious polarization introduced from changes in the beam as a function of elevation, or polarized sidelobes from the ground or telescope outer frame. Figures 4.10c and 4.11c shows that almost all of the pseudovectors pass this test.

Early Flight/Late Flight: Here the first half of the data is differenced with the second half of the data taken. If the beam shape degraded over time this test should reject a number of pseudovectors. However, Figures 4.10b and 4.11b show that very few pseudovectors were rejected.

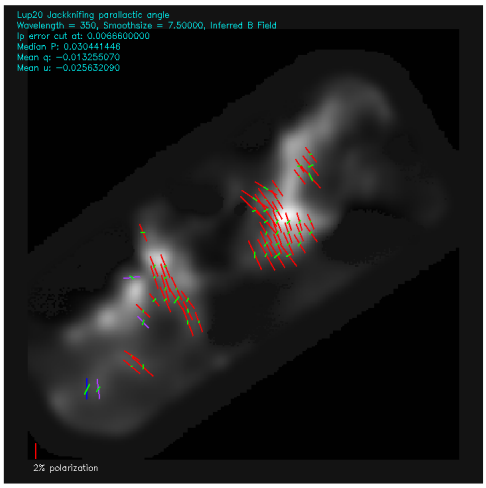

(a) Parallactic Angle

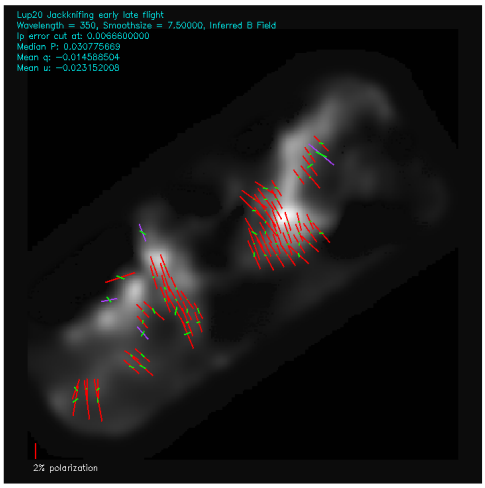

(b) Early/Late Flight

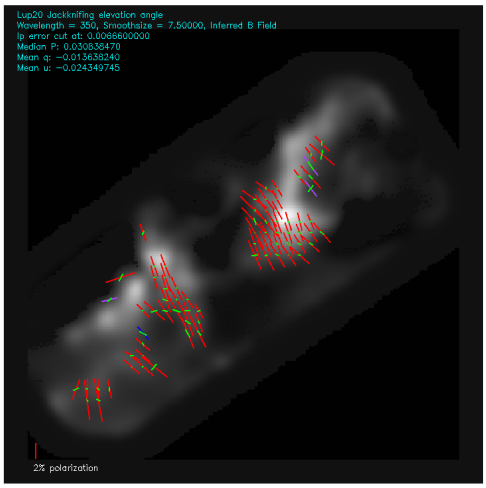

(c) High/Low Elevation

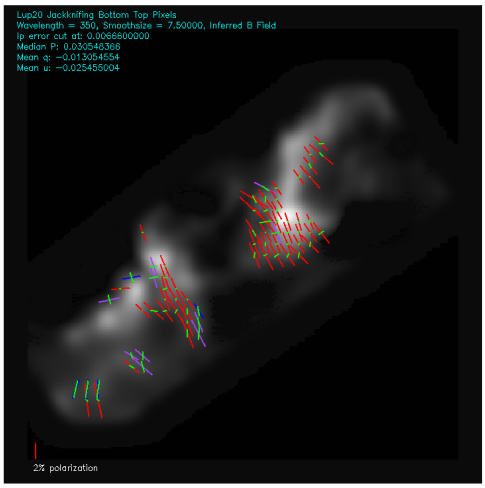

(d) Top/Bottom Bolometers

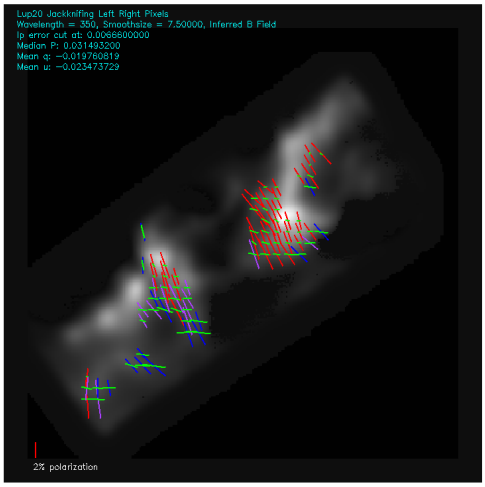

(e) Left/Right Bolometers

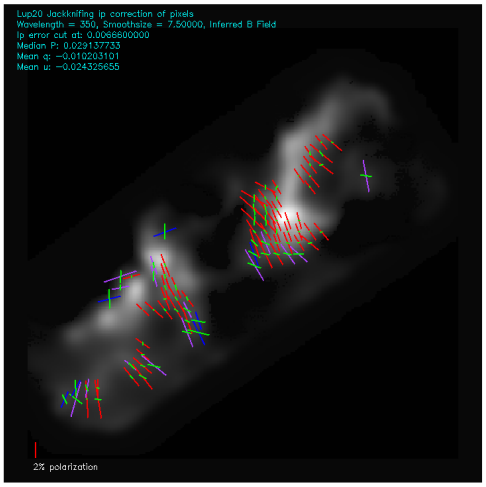

(f) High/Low IP Bolometers

Figure 4.10: Results from each 350 μm null test for the BLASTPol 2010 observations of Lupus I. Pseudovector colours represent the ratio of the amplitude of the polarization residual (shown in green) to polarized signal (length of the line). For red pseudovectors $p_{res} < p/3$, purple: $p/2 < p_{res} < p/3$, blue: $p_{res} > p/2$. The pseudovector orientation shows the polarization angle rotated by 90° to show the inferred orientation of the magnetic field. Only pseudovectors where $p_{res} < p/3$ (red) pass the null test.

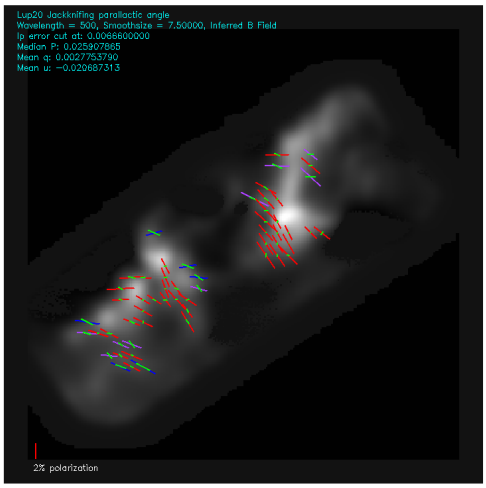

(a) Parallactic Angle

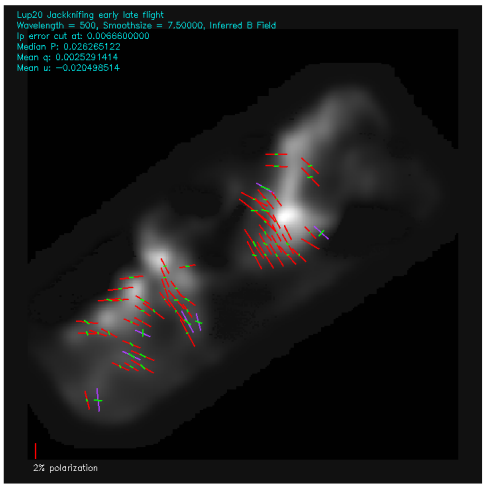

(b) Early/Late Flight

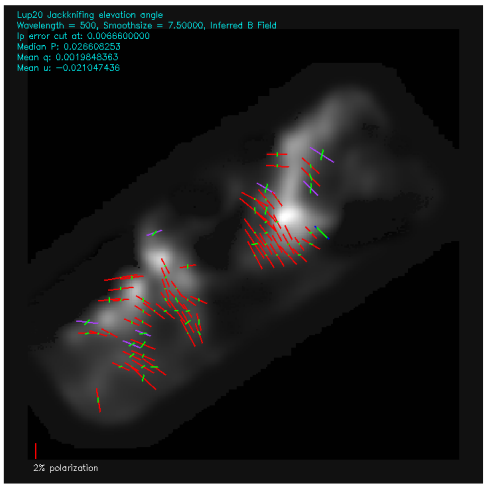

(c) High/Low Elevation

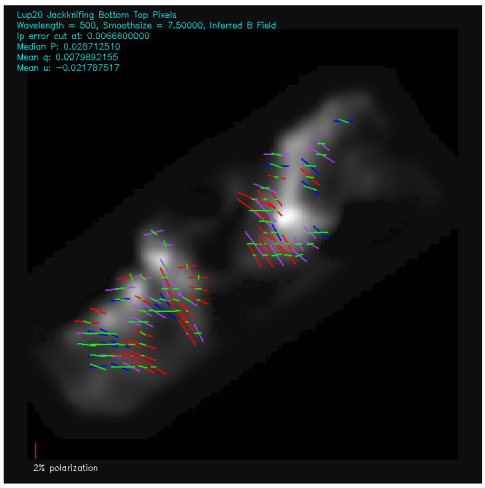

(d) Top/Bottom Bolometers

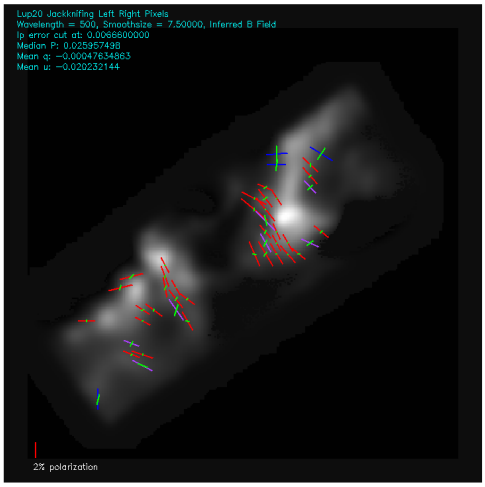

(e) Left/Right Bolometers

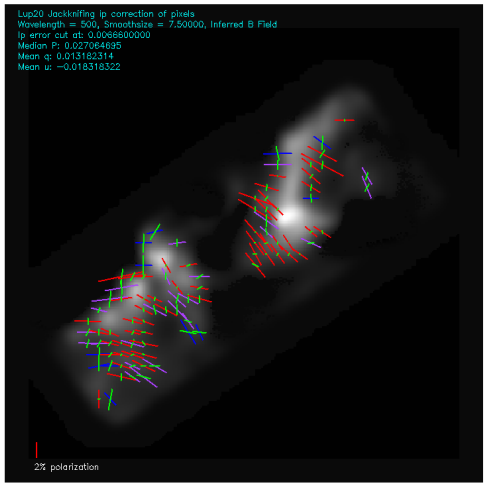

(f) High/Low IP Bolometers

Figure 4.11: Results from each 500 μm null test for the BLASTPol 2010 observations of Lupus I. Pseudovector colours represent the ratio of the amplitude of the polarization residual (shown in green) to polarized signal (length of the line). For red pseudovectors $p_{res} < p/3$, purple: $p/2 < p_{res} < p/3$, blue: $p_{res} > p/2$. The pseudovector orientation shows the polarization angle rotated by 90° to show the inferred orientation of the magnetic field. Only pseudovectors where $p_{res} < p/3$ (red) pass the null test.

4.4.2 Bolometer Null Tests

Additionally we required that all pseudovectors pass three null tests where instead of dividing the data in time, maps were made using half the detectors (keeping an equal number of H and V bolometers in each group). Overall these bolometer null tests rejected far more pseudovectors than the temporal null tests (Table 4.3), suggesting that the differences in beam shape and polarization across the array are more problematic than any change in beam shape with time.

Instrumental Polarization: As discussed in section 4.3.8 the instrumental polarization (IP) varies considerably from bolometer to bolometer. A consistency test was performed between the bolometers with the highest IP and the lowest IP.

Top/Bottom and Left/Right: There are also significant beam shape gradients across the bolometer array (Figure 4.2). Consistency tests between the left and right half of the array and tests between the top and bottom half of the array reject a significant fraction of the pseudovectors.

4.4.3 Grid Angle Null Test

As a final check, a null test was run between the detectors with horizontal grid angle orientations (H bolometers) and detectors with vertical grid angle orientations (V bolometers). Very few pseudovectors survived the test, but this is not surprising given that our polarimetry reconstruction method relies on differencing between adjacent H and V detectors in order to calculate Stokes parameters at sampling frequencies above the $1/f$ knee of the detectors. (This was discussed previously in Section 2.4). The failure of this null test is a reminder of the importance of the patterned polarizing grid for the successful operation of BLASTPol.

4.5 Simulations

4.5.1 Background

In order to create simulated TOD it is necessary to understand how the raw BLASTPol detector measurements relate to on-the-sky polarization.

To begin we define for vertically polarized bolometers:

$$q_{raw} \propto D(\theta = 0^\circ) - D(\theta = 45^\circ) \tag{4.7}$$

$$u_{raw} \propto D(\theta = 22.5^\circ) - D(\theta = 67.5^\circ) \tag{4.8}$$

where θ is the HWP angle and D is the signal level of the detector. The goal then is to relate q_{raw} and u_{raw} to q_{sky} and u_{sky}.

For horizontally polarized bolometers:

$$q_{raw} \propto -(D(\theta = 0^\circ) - D(\theta = 45^\circ)) \tag{4.9}$$

$$u_{raw} \propto -(D(\theta = 22.5^\circ) - D(\theta = 67.5^\circ)). \tag{4.10}$$

The conversion from raw polarization angles to sky polarization is defined by a number of rotation angles:

Raw to Telescope Coordinates: χ is the HWP angle as measured by the HWP encoder which maximizes signal in a vertically polarized pixel.

$$\begin{bmatrix} q_{raw} \\ u_{raw} \end{bmatrix} = \begin{bmatrix} cos(4\chi) & -sin(4\chi) \\ sin(4\chi) & cos(4\chi) \end{bmatrix} \begin{bmatrix} q_G \\ u_G \end{bmatrix}. \tag{4.11}$$

Telescope to Sky Coordinates: In astronomy position angles are measured with North at zero, and the angle increasing towards the East. The telescope measures polarization with respect to the gondola frame Φ_G, which we define to be in the positive elevation direction. To convert from the gondola reference frame to

the sky reference frame it is necessary to know the angle between the positive elevation direction in the gondola and north ρ. Then

$$\Phi = \Phi_G - \rho \tag{4.12}$$

where Φ is the polarization defined in the sky reference frame.

These equations can be used convert between Stokes parameters in the gondola and sky reference frames:

$$\begin{bmatrix} q_G \\ u_G \end{bmatrix} = \begin{bmatrix} cos(2\rho) & -sin(2\rho) \\ -sin(2\rho) & cos(2\rho) \end{bmatrix} \begin{bmatrix} q_{sky} \\ u_{sky} \end{bmatrix}. \tag{4.13}$$

$$q_{sky} = Q_{sky}/I = p\,cos(2\Phi), \tag{4.14}$$

$$u_{sky} = U_{sky}/I = p\,sin(2\Phi), \tag{4.15}$$

where $p \equiv \sqrt{Q_{sky}^2 + U_{sky}^2/I^2}$ is the fraction of the emission which is linearly polarized.

Combining all these equations we can then solve for the signal in a bolometer:

$$D = \frac{I}{2}\left(1 + \eta\left(q\cos\beta + u\sin\beta + q_{IP}\cos\beta_{IP} + u_{IP}\sin\beta_{IP}\right)\right) \tag{4.16}$$

where

$$\beta = 4\theta - 4\chi - 2\rho + 2\alpha \tag{4.17}$$

is the phase angle and

$$\beta_{IP} = 4\theta - 4\chi + 2\alpha \tag{4.18}$$

is the equivalent phase angle for the instrumental polarization, which has no dependence on the sky rotation angle ρ, and α is the grid angle ($\alpha = 0^\circ$ for horizontal bolometers and 90° for vertical bolometers).

4.5.2 *simsky*

The software package which produces simulated TOD is *simsky*. This code was originally developed for the BLAST 2006 analysis to investigate the impact of various mapmaker pipelines on the output intensity structures. *simsky* has since been modified to produce TOD using Equation 4.16. It was also modified to accept beam profiles for each HWP angle (in order to simulate a polarized beam) and instrumental polarization terms q_{IP} and u_{IP}.

The inputs to *simsky* are:

- Maps of the Stokes I, Q and U parameters to be "observed" with the simulator.
- A list of data ranges over which the simulated TOD should be calculated.
- Time ordered pointing information for raster scans used to "observe" the input maps. Typically this data is taken from post-flight pointing reconstructions (Section 4.3.6) of actual BLASTPol science scans.
- Ancillary pointing information for the three BLAST bolometer arrays including the pointing offset of each bolometer with respect to the central bolometer, and corrections to the angle between the star camera axes with respect to the central bolometer as a function of time.
- Amplitude spectra representing the uncorrelated component of each detector's noise.
- Amplitude spectra for the correlated component of the detector noise.
- Time ordered data giving θ the angle of the HWP as a function of time.
- Optionally a beam map or series of beam maps which are given in telescope coordinates. The program can accept a single map representing the beam for

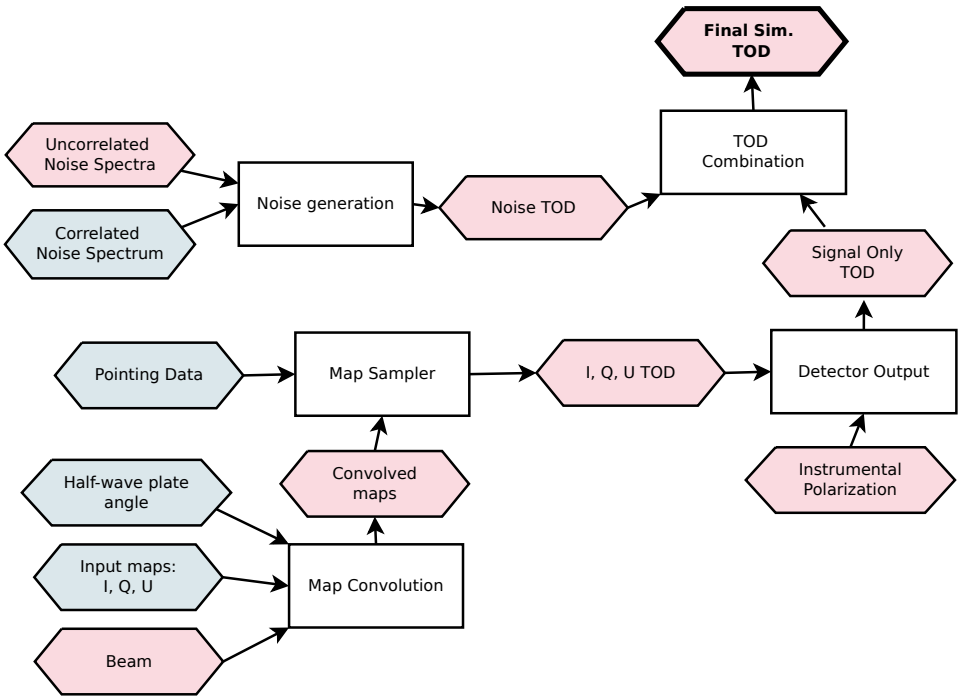

Figure 4.12: A block-level diagram of the *simsky* program showing the steps to produce simulated bolometer time ordered data (TOD). Data are indicated with hexagons, software processes with rectangles. Blue indicates data which are the same for all bolometers, pink data which may be different for each bolometer.

all bolometers and all HWP angles, or multiple maps representing the beam for individual bolometers as a function of HWP position.

Figure 4.12 shows a block-level diagram of the the *simsky* program run on each individual data chunk (approximately 15 minutes of data).

4.5.3 Vela C Simulations: Nominal Case

Source polarization and instrumental polarization reconstruction fidelity were tested with simulated observations of the Vela C molecular cloud. Vela C is both very bright, and has a great deal of structure, including a very bright region around RCW 36 which could be expected to show artifacts from the mapmaker. Simulations were made for all bolometers in the 500 μm array.

Figure 4.13 shows the input intensity map, obtained from the Herschel Science Archive[4] and described in Hill et al. (2011). At 500 μm the Herschel SPIRE beam has a FWHM of 36.3″, which is much smaller the diffraction limited BLAST beam FWHM of 60″. The SPIRE map has a pixel size of 14″. Stokes Q and U maps were generated assuming a constant polarization fraction: $Q = qI$ and $U = uI$, where q and u are constant across the map.

Signal only TOD were generated using pointing and HWP angles from ∼19 hours of Vela C scans, with roughly equal coverage at each HWP position (Table 4.1). These pointings correspond to the same data ranges used to calculate the instrumental polarization for BLASTPol 2010.

Noise TOD were generated and added to the signal TOD. The noise TOD consist of both a noise component that is uncorrelated between the detectors and a correlated noise component meant to represent the low frequency 1/f noise. Noise levels were based on individual bolometer fits to amplitude spectral density plots derived from 18.33 minutes of BLASTPol 2010 data where the telescope was not scanning (Soler 2013). The uncorrelated component consisted of white noise, with the white noise levels taken from the fit for each bolometer. Correlated noise levels were generated

[4] `http://herschel.esac.esa.int/Science_Archive.shtml`. Herschel is an ESA space observatory with science instruments provided by European-led Principal Investigator consortia and with important participation from NASA.

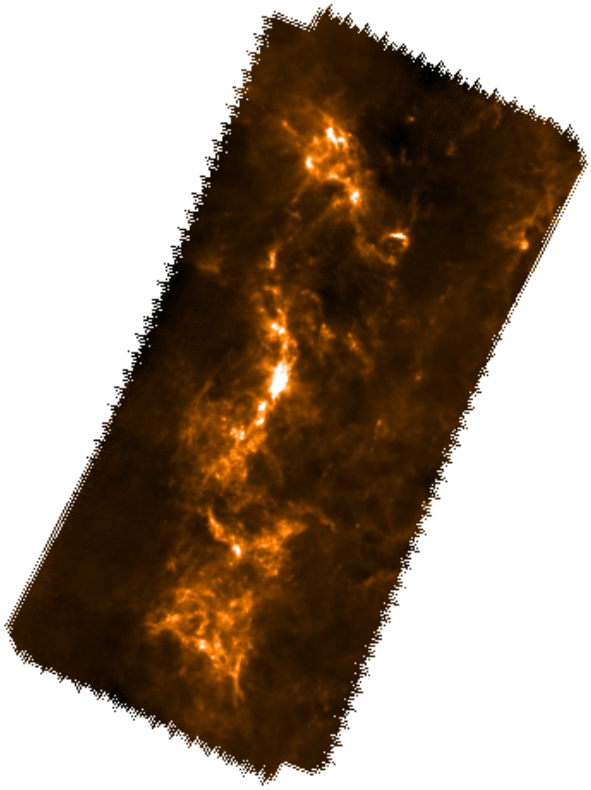

Figure 4.13: Herschel SPIRE 500 μm map of the Vela C molecular cloud, which was used as an input to the simulations discussed in this section.

from an input power spectrum of the form:

$$PSD_{corr} = W\frac{f_0}{f} \tag{4.19}$$

where W is the median white noise level of all 500 μm bolometers, f_0 is the median $1/f$ knee, and f is the frequency. For the 500 μm bolometers W= 3.8×10^{-6} V Hz$^{-1/2}$ and $f_0 = 0.214$ Hz.

As a first test the Vela simulations were run using an unpolarized Gaussian beam with a FWHM of 60″. This beam was used for all bolometers at all HWP positions. No instrumental polarization was included in the simulation.

Once the simulated TOD were created they were fed back into the mapmaker in order to create output maps. The results from a simulation with $u = 0$ and $q = 0.02$ are shown in Figure 4.14. The mapmaker reproduces the intensity structure, with no visible I to U or Q to U mixing. Artifacts can be seen in the map associated with the scan strategy and filtering. In particular near the brightest source in the map RCW 36 large negative "bowls" can be seen. Removing these effects requires an optimal mapmaker, which will be the subject of future work.

Next, the TOD were run through the full analysis pipeline described in Section 4.3.8. Instrumental polarization values were calculated for every bolometer; they range from 0 to 1%, with a median IP of 0.48%. The full null test pipeline was run after correcting the maps for IP found by sky rotation.

In total 178 pseudovectors passed both the intensity cut and the null tests. The derived polarization vectors (rotated by 90 degrees to show inferred field direction) are shown in the left panel of Figure 4.16, with histograms in Figure 4.17 showing the distribution of percentage polarization p (4.17a) and polarization angle Φ (4.17b).

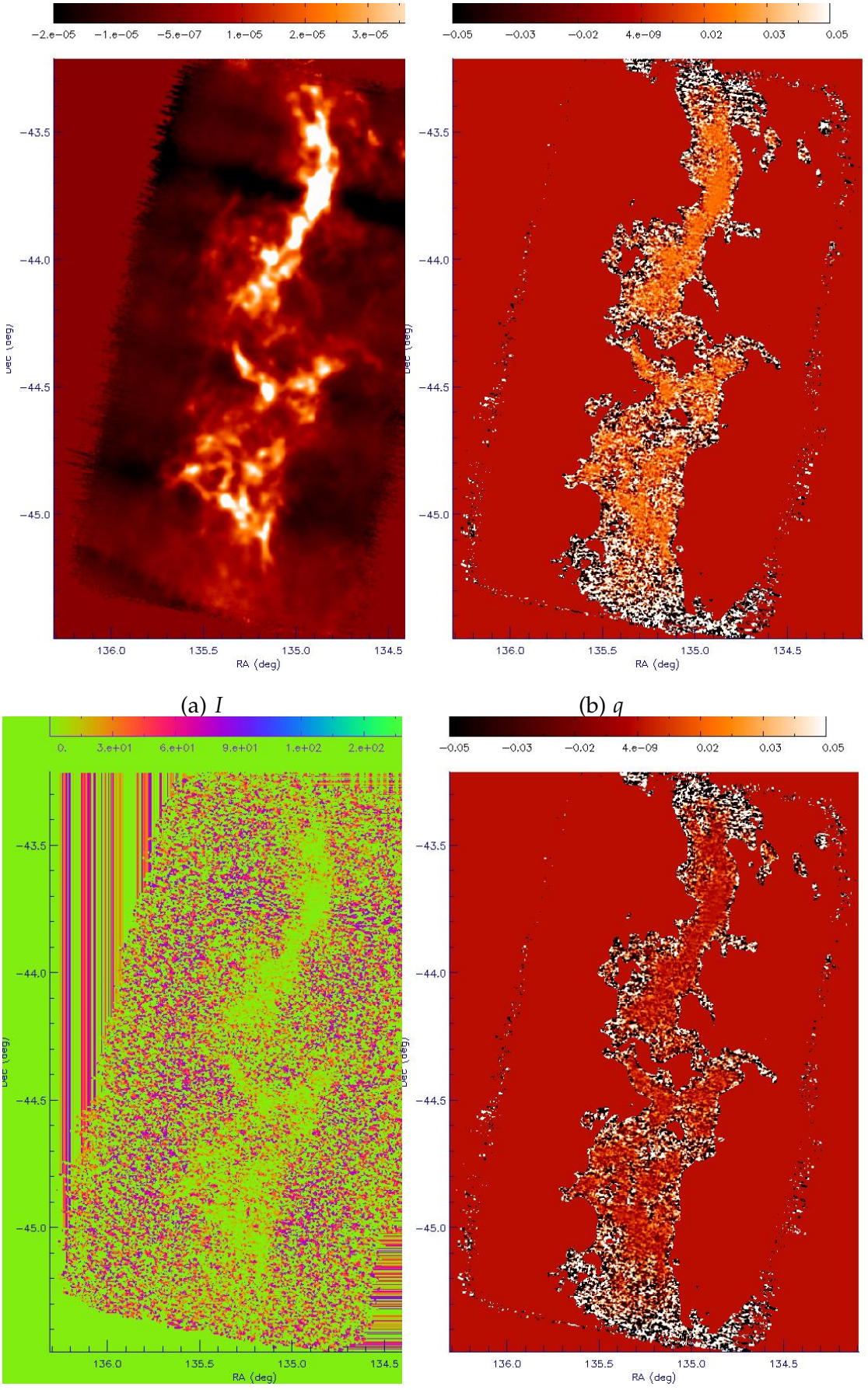

(a) I (b) q

(c) Φ (d) u

Figure 4.14: Output maps from a 500 μm Vela C simulation made with a round 60″ FWHM Gaussian beam and no input instrumental polarization.

4.5.4 Vela C Simulations With Polarized Beams and Instrumental Polarization

An additional simulation was created with non-Gaussian, asymmetric beams, and significant instrumental polarization for each bolometer. The shape of the beam varied both with polarizing grid angle (H and V bolometers) and with HWP position. The goal of this simulation was to test whether our data reduction pipeline could reconstruct polarization for an instrument with similar limitations to BLASTPol in 2010.

The beam shapes are based on a least squares fit of 3 two-dimensional Gaussians to maps of the source IRAS 08470-4243, a compact and bright object in the Vela Molecular Ridge. Maps of this IRAS source were made separately for all H and V bolometers, and for the two waveplate positions with sufficient coverage to produce high signal-to-noise maps: $\theta = 0$ and 67.5°. For the other two HWP positions angles the beam for $\theta = 22.5^\circ$ was made to be identical to the beam for $\theta = 0^\circ$, and the beam for $\theta = 45^\circ$ was made to be identical to the beam for $\theta = 67.5^\circ$. All beams were normalized to have the same total flux, thus difference between any two beams averaged over a large aperture is zero and the net instrumental polarization over the simulation beam is zero.

The beam fits are shown in Figure 4.15, with red showing the H bolometer fits, and green showing the fit for V bolometers. The H bolometer fits are slightly more elongated compared to the V bolometer fits, and also the H bolometers seem to have more power in the left most sidelobe. IRAS 08470-4243 is not a point source, so the beam shape derived from these fits likely has more extended structure than the actual BLASTPol beam.

Instrumental polarization terms q_{ip} and u_{ip} from Equation 4.16 were generated for each bolometer:

$$q_{ip,j} = -0.040 + \gamma_j\, 0.070, \tag{4.20}$$

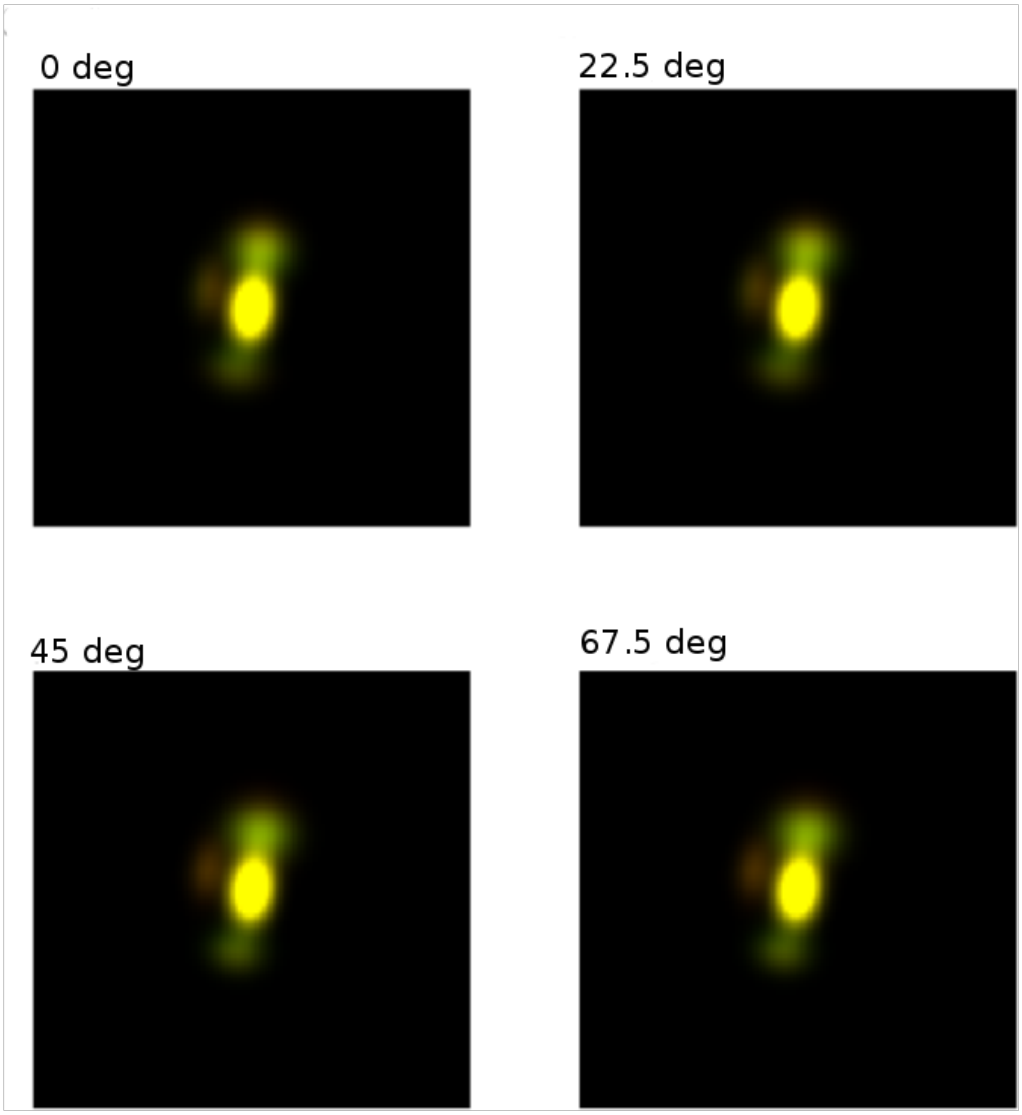

Figure 4.15: Polarized beams based on fits to IRAS 08470-4243. Red in these images corresponds to the beam for H bolometers, green for V bolometers.

$$u_{ip,k} = 0.020 + \gamma_k\, 0.030, \tag{4.21}$$

where γ_j and γ_k are random numbers selected from a normal distribution.

The right panel of Figure 4.16 shows pseudovectors for the polarization systematics simulation. In total 201 pseudovectors passed the intensity cut, polarization cut and null tests.

Figure 4.17 shows the histograms of p and Φ for both the ideal polarimeter (no IP) simulations, and the large IP polarized beam simulations. The large IP simulations span a much larger range of Φ angles and polarization percentage values p. Still the large IP/polarized beam simulation was able to reproduce the mean polarization direction of the input maps to $\sim$5%.

Interestingly, in both simulations the peak of the Φ histogram is offset from the input polarization angle (marked with a dashed vertical line in Figures 4.17b and d) by 4 or 5°. This may be an effect of high-pass filtering of the TOD in *naivepol*, or it could be caused by an uncertainty in measuring the IP.

4.5.5 Point Source Reconstruction Simulations

For BLASTPol 2010 the beam is known to be polarized and non-Gaussian. Therefore in the 2010 science analysis the maps were convolved with a 2.5′ FWHM Gaussian to try to smooth out all structure on beam scales. Even then a polarized point spread function can cause significant deviations from the true polarization angle (as shown in Figure 4.17). As such for the 2010 data analysis we interpret only the large scale field direction not individual pseudovectors (Matthews et al. 2013). For the 2012 data these restrictions will hopefully not be necessary, so it is important to understand the effects of the mapmaker on point source observations.

One aspect of the mapmaking pipeline that required simulations is the pixelization residuals. Mixing of Stokes I into Q and U is the result of the assumption in the

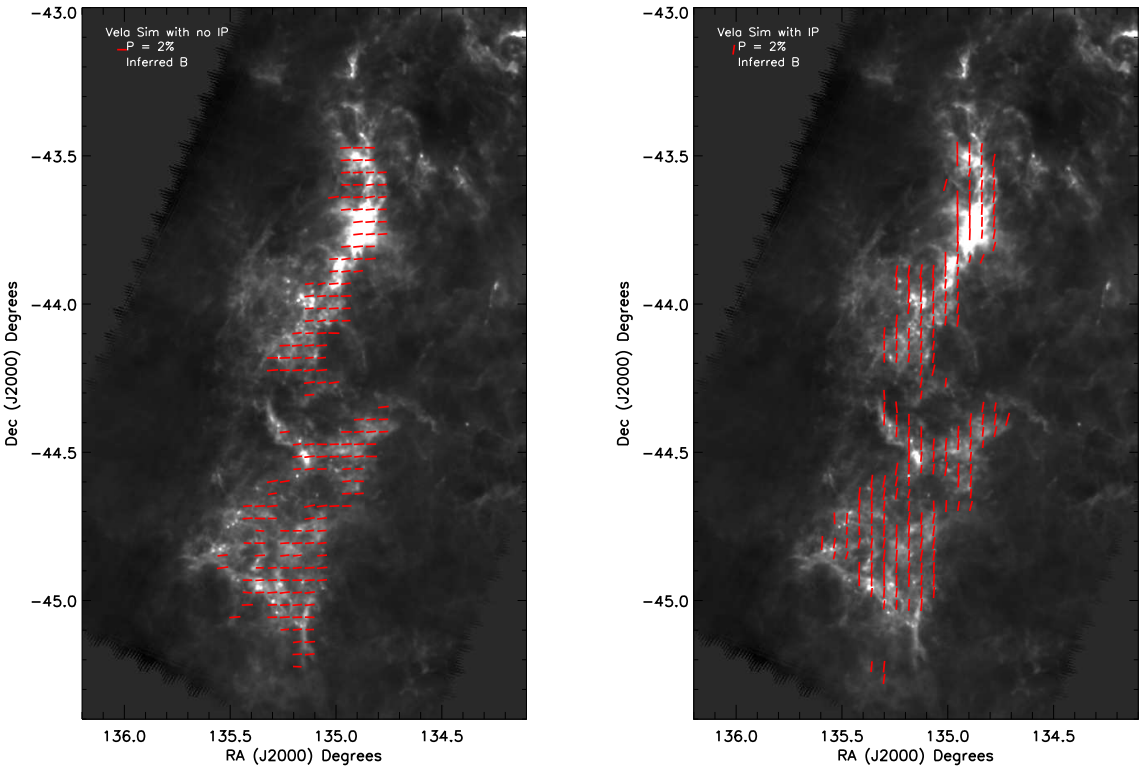

Figure 4.16: 500 μm pseudovectors made by passing simulated TOD through the entire mapmaking/IP correction pipeline. The pseudovectors have been rotated by 90° to show the inferred field direction. The pseudovector in the legend shows the direction of the polarization (rotated by 90°) in the input simulation maps. *Left panel:* Unpolarized 60″ FWHM beam with no input instrumental polarization. Input polarization maps were Q=0.02I and U=0.00I. *Right Panel:* Instrumental polarization as described in Equations 4.20 and 4.21, and beams were based on fits to IRAS 08470-4243 for H and V bolometers at different HWP positions. Input polarization maps were Q=-0.018I and U=0.005I.

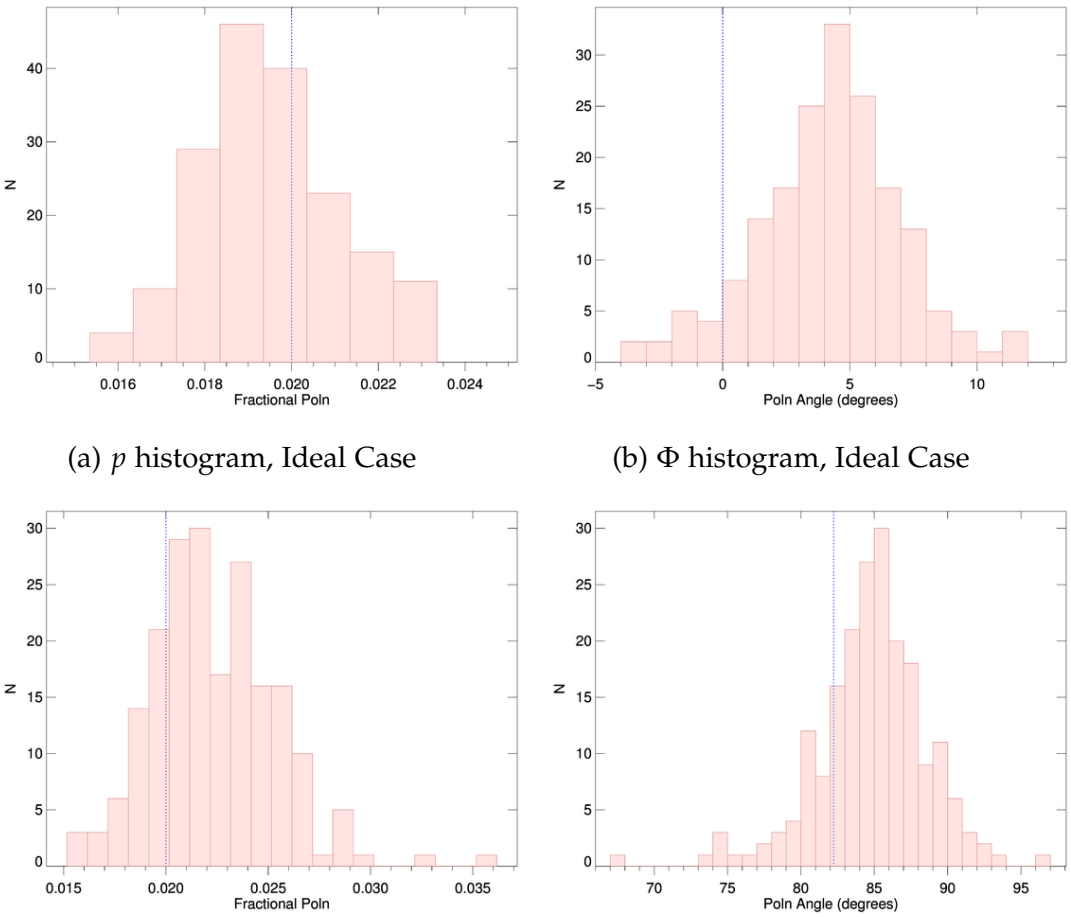

(a) p histogram, Ideal Case

(b) Φ histogram, Ideal Case

(c) p histogram, with IP + polarized beam

(d) Φ histogram, with IP + polarized beam

Figure 4.17: Histograms of percentage polarization p and polarization angle Φ for Vela C simulated observations. The vertical blue dashed line in each figure shows the simulation input.

Type	Ideal Instrument	With Poln Systematics
Input q	0.020	-0.018
Input u	0.000	0.005
Input q_{ip}	0.000	-0.040±0.070
Input u_{ip}	0.000	0.020±0.030
Input Φ	0°	82.2°
$\bar{q_{out}}$	0.019	-0.017
$\bar{u_{out}}$	0.004	0.001
Median $q_{ip,out}$	0.0020±0.0033	-0.040±0.051
Median $u_{ip,out}$	-0.0036±0.0021	0.019±0.019

Table 4.4: Results from the simulations of Vela C for *left:* An ideal instrument (no input IP, a round unpolarized beam), *right:* Instrument with significant instrumental polarization, and a beam shape that is non-Gaussian and varies with HWP angle.

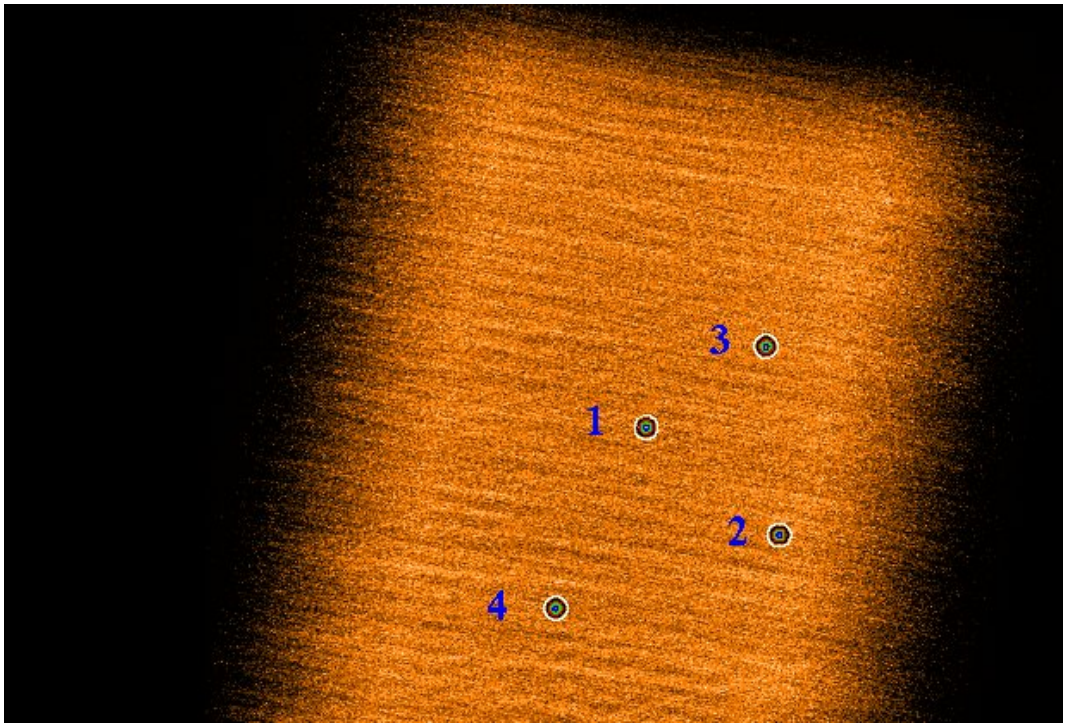

Figure 4.18: Map of the number of hits per pixel for the point source simulation, with contours from the output map of Stokes I showing the locations of the four Gaussian "sources". Sampling of the input maps was made using the pointing solution derived for 80 scans of the Vela C molecular cloud from 2010 BLASTPol flight.

mapmaker that the source flux does not vary across a map pixel. That assumption is reasonable if the pixel size is much smaller than the FWHM of the telescope beam, but it is not a good assumption if the pixel size is only a few times the beam FWHM.

Simulations were made for the 500 μm array. Input maps consisted of four identical 60″ FWHM Gaussians with no polarization ($Q = U = 0$ for the input maps), with a pixel size of 1″. These input maps were then observed with *simsky* using the pointing reconstructed for 80 scans of Vela C from the BLASTPol 2010 flight. Figure 4.18 shows the hits per pixel for the output map, with intensity contours showing the locations of the four simulated sources.

The mapmaker *naivepol* was then used to make output polarization maps (I,Q and U) from the simulated TOD. Since the goal of the simulations was to look for I

to Q and U leakage from pixelization, only the signal+white noise TOD were used (no correlated noise component or 1/f noise, instrumental polarization or additional beam convolutions were used), and thus the TOD did not require high-pass filtering. The signal-to-noise of the point source simulation was set to be very large, $\sim$8000, so that the polarization residuals in the output maps can be attributed to I to Q and U leakage rather than TOD noise.

Output polarization maps were produced with a variety of pixel sizes: 20, 10, 5, 2 and 1″. Pixels of 20″ correspond to three pixels per source FWHM. The output maps were then convolved with a 60″ Gaussian to obtain the photometry of the source and smooth out pixel-to-pixel map noise.

The thumbnail images of the each of the sources in Figures 4.19 to 4.22 show the results of the simulation. I to Q/U mixing can be seen in all the output maps, but the residuals are larger for maps made with a coarse pixel size. With 20″ map pixels the residuals are small compared to the flux of the point source in I (q, u <0.3%), and with 10″ map pixels the residuals are even smaller q, u <0.1%.

Figure 4.23 shows the q, u and p values measured for each source as a function of pixel size. The Q, U and I photometry was calculated by convolving the sources with a normalized Gaussian of 60″ FWHM, which gives a weighted average of the surrounding pixels. The calculated p_{res} values tend to increase with increasing pixel size, but even with 20″ pixels the p_{res} values are all below 0.5%, which is our 1-σ uncertainty limit on the instrumental polarization reconstruction from the Vela C simulations.

It would appear that the polarization of an isolated point source recovered from aperture photometry would not be contaminated by I to Q and U mixing due to pixelization residuals. The limiting error remains the uncertainty of the instrumental polarization of 0.5%.

The other concern is that I to Q and U mixing could create spurious polarization that would contaminate the pseudovectors in nearby lower flux regions. Consider a

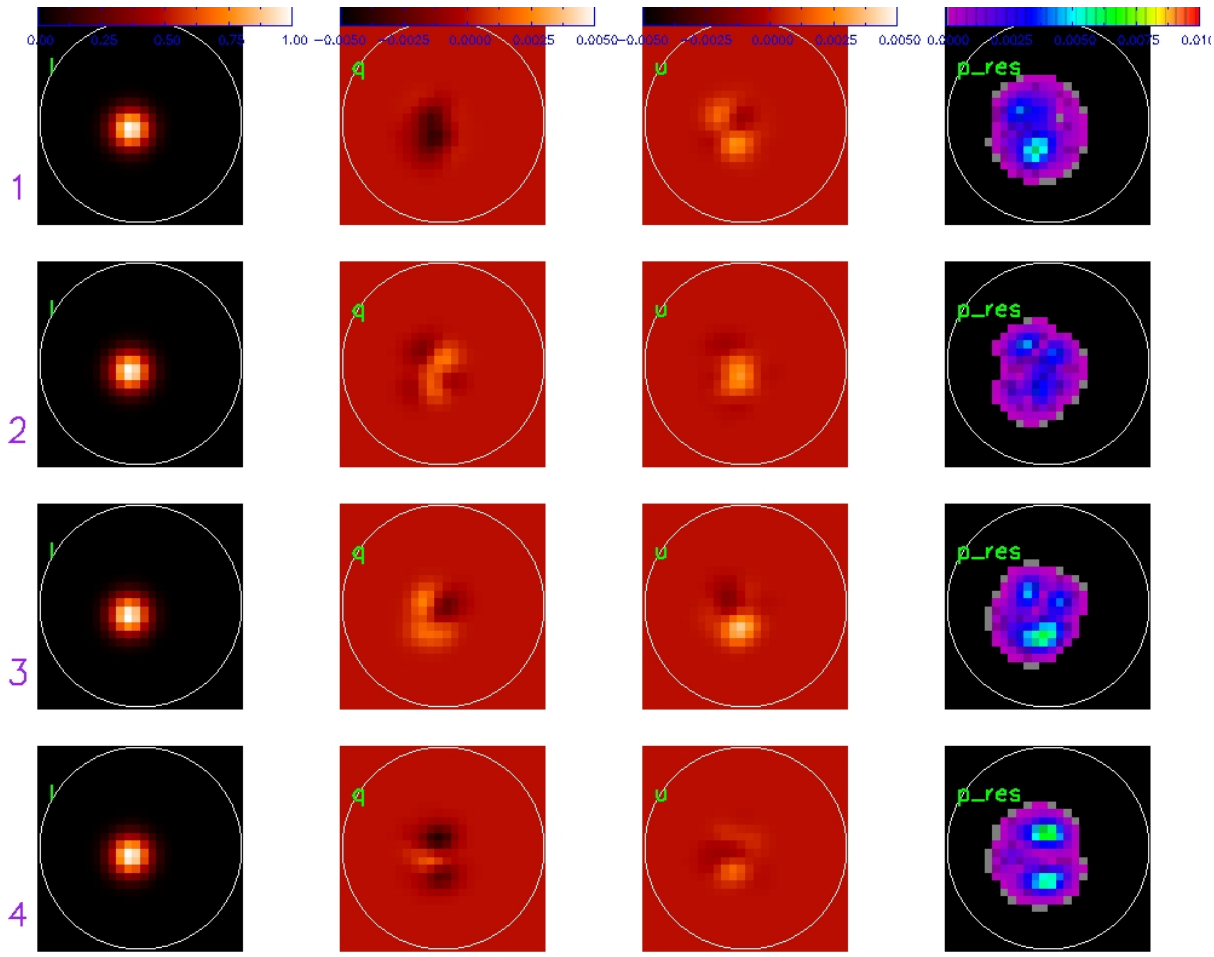

Figure 4.19: Output simulation maps made with 20″ pixels of four point sources mapped with the Vela C scan strategy from BLASTPol 2010. The first three columns show I, Q and U simulation output maps smoothed by convolving with a 60″ FWHM Gaussian. The Q and U maps have been normalized to the brightest pixel in the I map (I_{max}). The right most column shows the spurious polarization p' that would be observed if this source was embedded in an extended feature with intensity $=0.2\times\ I_{max}$.

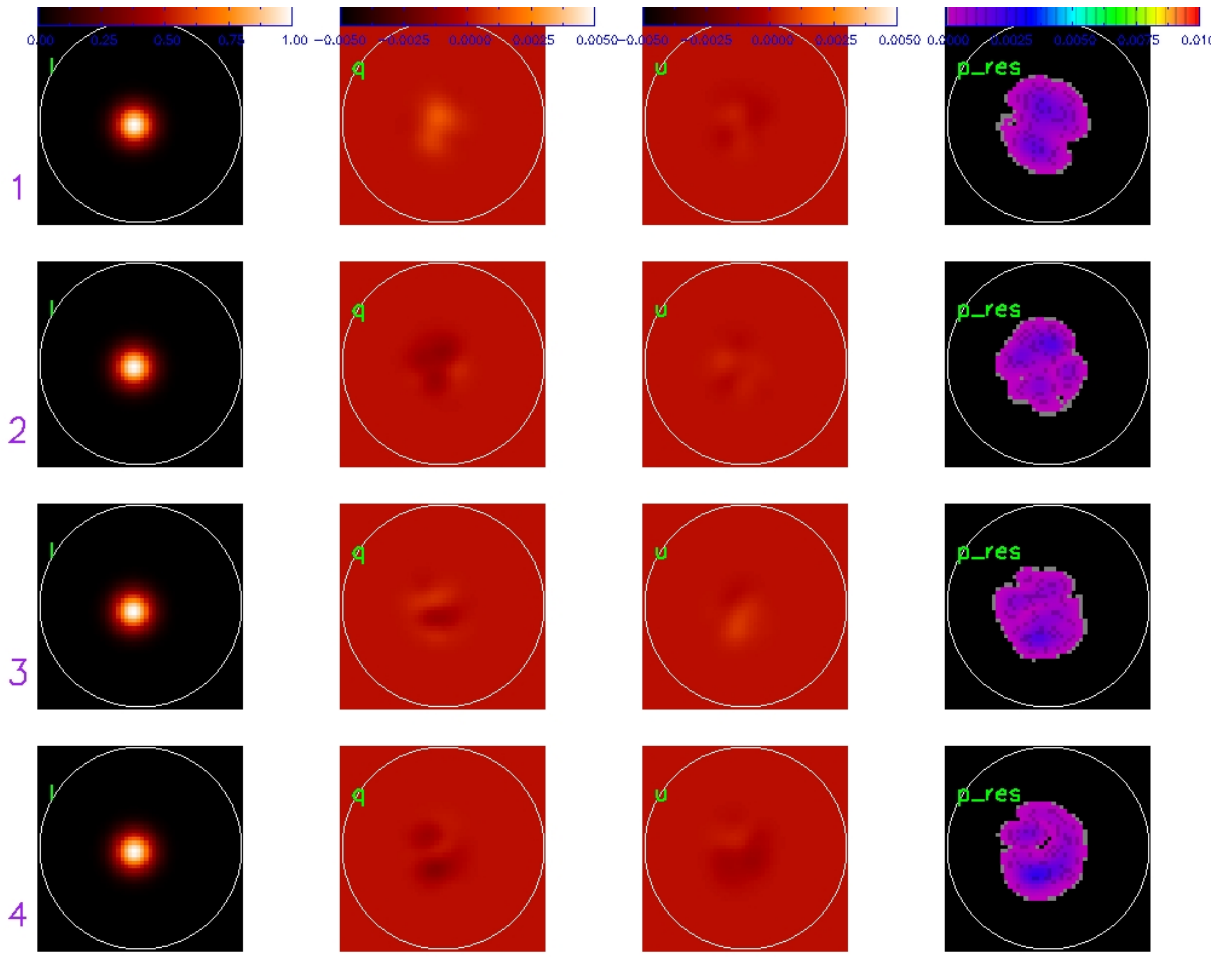

Figure 4.20: Output simulation maps made with 10″ pixels of four point sources mapped with the Vela C scan strategy from BLASTPol 2010. The first three columns show I, Q and U simulation output maps smoothed by convolving with a 60″ FWHM Gaussian. The Q and U maps have been normalized to the brightest pixel in the I map (I_{max}). The right most column shows the spurious polarization p' that would be observed if this source was embedded in an extended feature with intensity $=0.2\times\ I_{max}$.

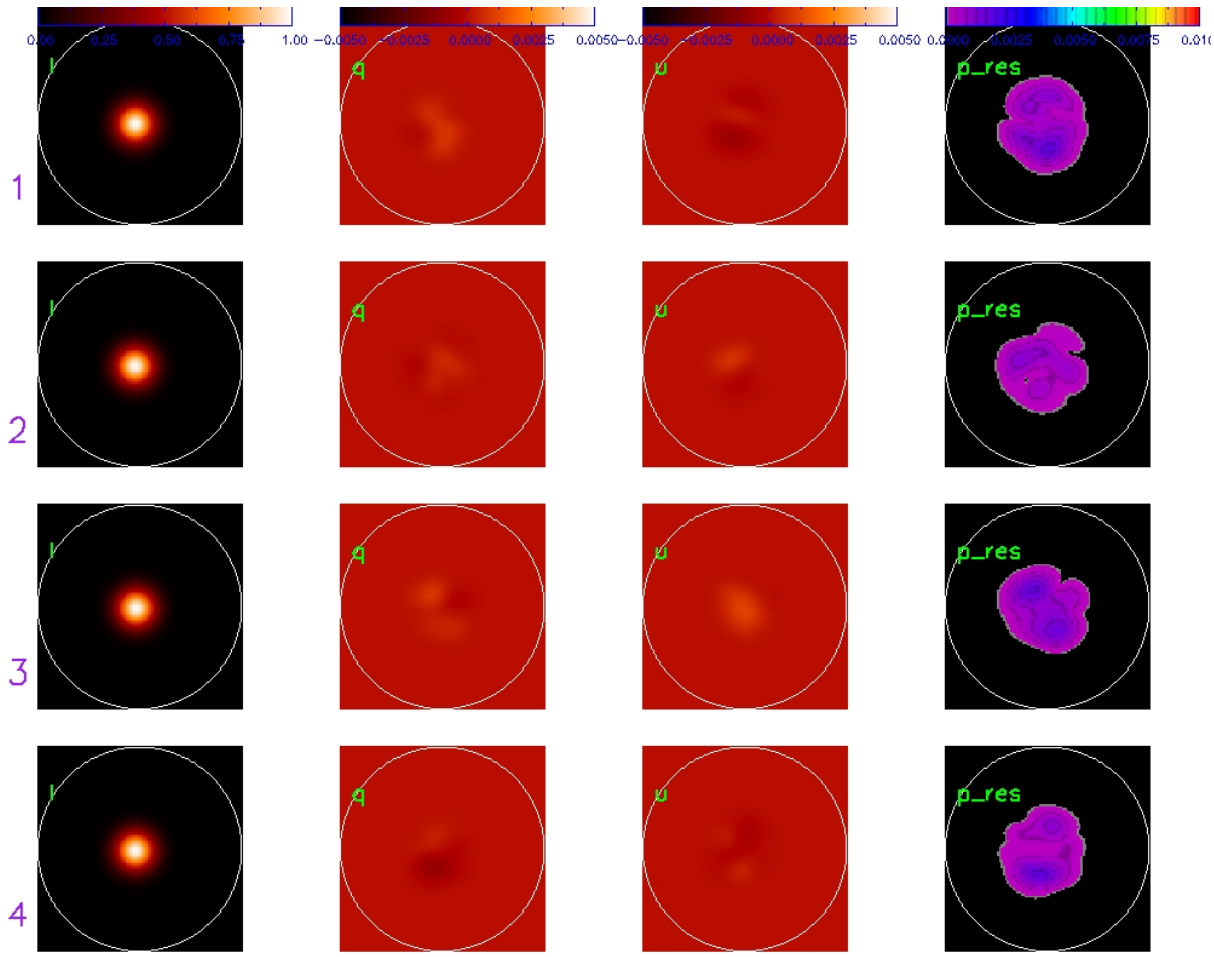

Figure 4.21: Output simulation maps made with 5″ pixels of four point sources mapped with the Vela C scan strategy from BLASTPol 2010. The first three columns show I, Q and U simulation output maps smoothed by convolving with a 60″ FWHM Gaussian. The Q and U maps have been normalized to the brightest pixel in the I map (I_{max}). The right most column shows the spurious polarization p' that would be observed if this source was embedded in an extended feature with intensity $=0.2\times\ I_{max}$.

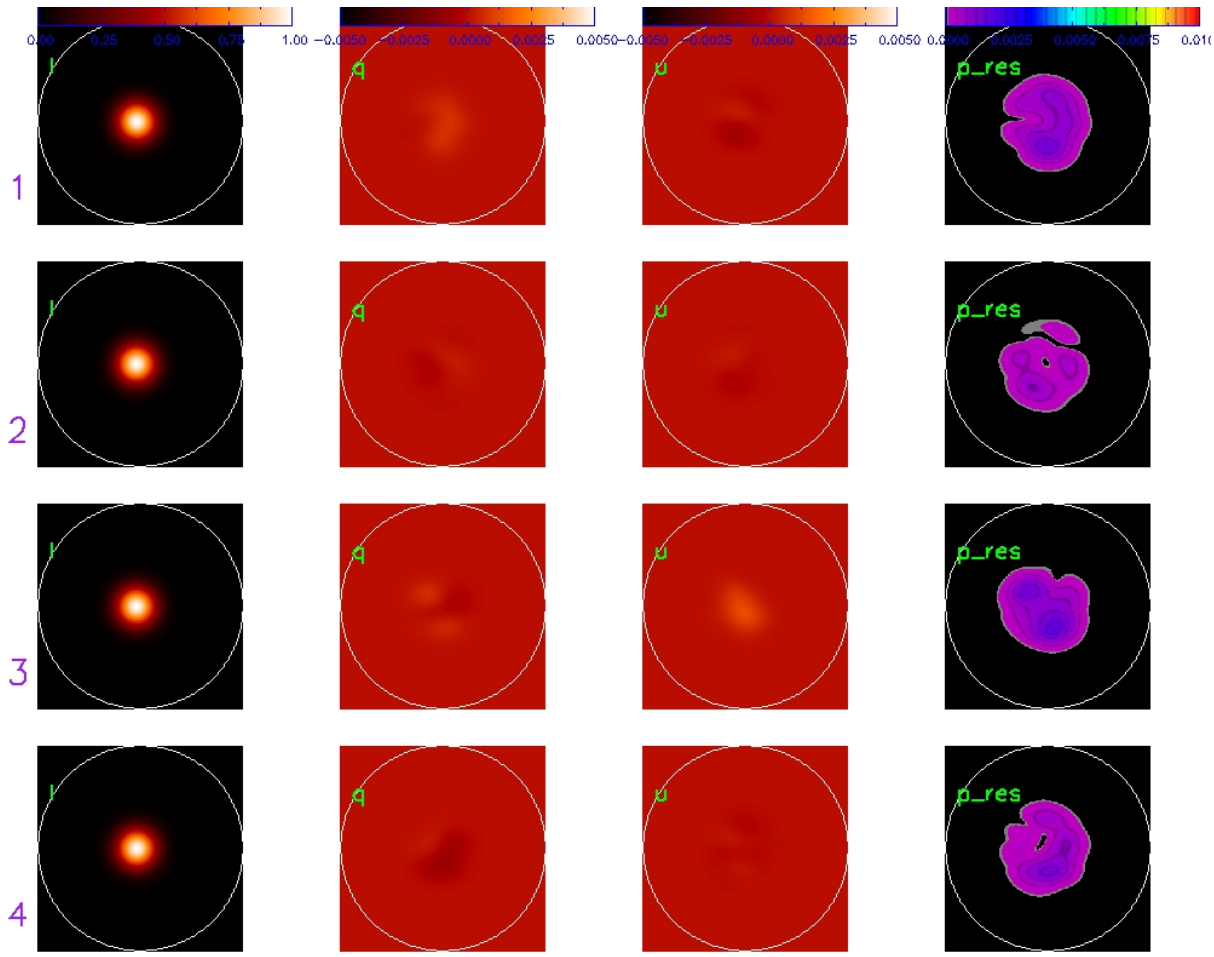

Figure 4.22: Output simulation maps made with 2″ pixels of four point sources mapped with the Vela C scan strategy from BLASTPol 2010. The first three columns show I, Q and U simulation output maps smoothed by convolving with a 60″ FWHM Gaussian. The Q and U maps have been normalized to the brightest pixel in the I map (I_{max}). The right most column shows the spurious polarization p' that would be observed if this source was embedded in an extended feature with intensity $=0.2\times\ I_{max}$.

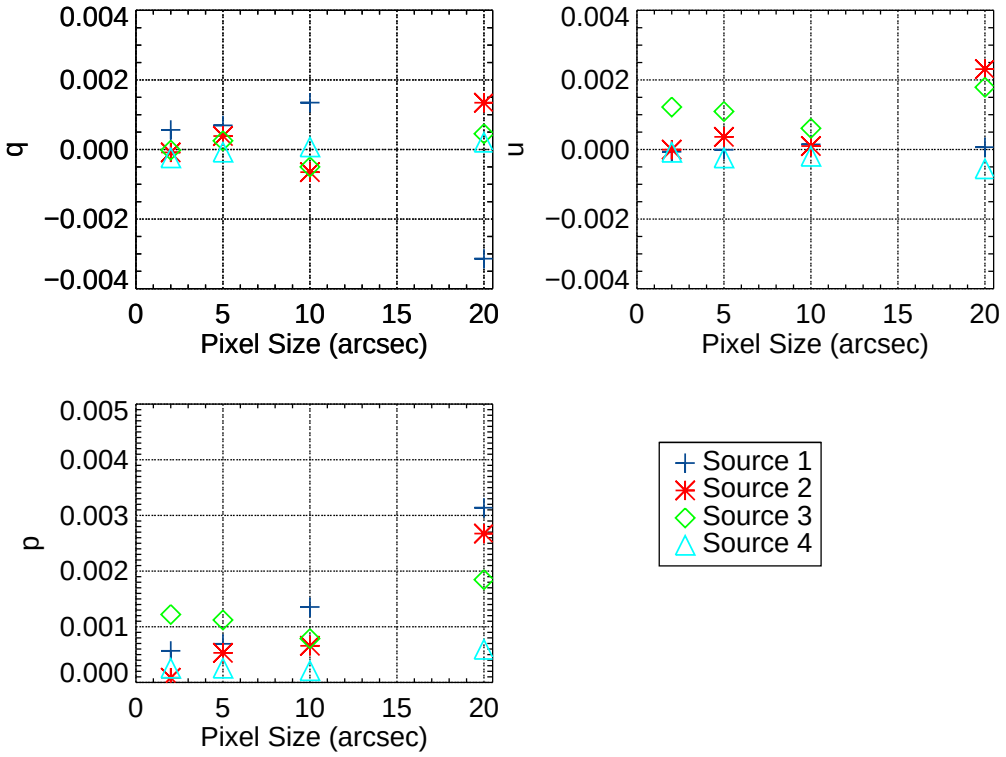

Figure 4.23: Polarization measured from BLASTPol simulated observations of four unpolarized point sources, scanned with the BLASTPol 2010 pointing reconstruction for scans of the Vela C molecular cloud.

point source (A) embedded in a fainter extended flux feature (B). To avoid contamination from the point source we would want to exclude any map pixels with a spurious polarization $p' > 0.5\%$. For each simulated source we can calculate how many map pixels would need to be excluded assuming a ratio between the peak flux of the point source $I_{A,Max}$ and I_B of ζ:

$$p'(x,y) = I_A(x,y) + \zeta I_{A,Max}. \tag{4.22}$$

The rightmost panels of Figures 4.19 to 4.22 show p' assuming $\zeta = 5$. For the case of $20''$ pixels a few map pixels would have p' above 0.5%, but for smaller pixel sizes p' was always less than 0.5%. This experiment was repeated for different values of ζ: 2, 5, 10 and 20[5]. Only the maps made with a pixel size of $20''$ had p' above 0.5%. From this study it seems that using a pixel size of 1/6 the beam FWHM or smaller is enough to ensure that the source photometry is not contaminated by spurious polarization due to I to Q or U mixing from map pixelization.

4.6 Summary

In this chapter I have outlined the observations made with BLASTPol during the 2010 flight and discussed the various pathologies of the dataset. The 2010 flight had severe systematics introduced by the damaged infrared blocking filter, which caused large instrumental polarization which varied from bolometer to bolometer.

I describe in Section 4.3 the data reduction pipeline used for the 2010 data, which consisted of cleaning the detector TOD, reconstructing telescope pointing, determining the instrumental polarization through sky rotation, making maps with the polarized mapmaker *naivepol* and finding suitable reference regions in the maps to set a zeropoint for the I, Q, and U maps.

[5]In the BLAST 2006 maps of Vela C the largest ζ value found was around the brightest point of RCW 36 in the 250μm map, where the ratio between the brightest pixel in RCW 36 and a pixel three beam FWHM away was 13. For most compact sources in Vela C ζ is a factor of 2-5.

In section 4.4 I looked at a series of null tests of the 2010 flight data. These various null tests were chosen to be sensitive to sidelobes (parallactic angle, elevation angle) or beam shape differences (high IP/low IP). In the case of the Lupus I cloud a number of pseudovectors pass all the null tests.

I have shown using instrument simulations that the BLASTPol instrument can be used to reconstruct polarization angles and percentage polarizations. Even with a polarized non-Gaussian beam and large instrumental polarization the output simulated maps showed the same global polarization direction as the input maps.

The simulations also show that average instrumental polarization can be reconstructed to within 0.5%. The instrumental polarization was then removed in the mapmaker. In addition after correcting for the IP the BLASTPol maps of Carina Nebula and G 331.5-01 showed similar polarization angles to the observations made by the SPARO instrument at 450μm (Li et al. 2006).

Chapter 5

Preliminary Polarization Maps From the BLASTPol 2012 Flight

5.1 Chapter Overview

This chapter provides a brief overview of the BLASTPol 2012 data quality and presents preliminary maps of several BLASTPol targets produced using the 2010 data reduction pipeline presented in Chapter 4. More work needs to be done on the data reduction before these maps will be ready for science interpretation, but even the preliminary maps show the potential of this dataset.

5.2 2012 Data

5.2.1 2012 Observations Overview

Table 5.1 shows a summary of the BLASTPol observations taken during the 2012-2013 BLASTPol flight. The table gives the target name and type as well as the total time spent observing each target compared to the total amount of unflagged data used in making the output science maps shown later in this section. The fraction of time spent at each half wave plate (HWP) position (f_0, $f_{22.5}$, f_{45}, $f_{67.5}$) is also listed.

Comparing the BLASTPol 2012 and 2010 observations (Table 4.1) there are a few obvious differences. Less data was flagged in the BLASTPol 2012 flight because the anomalous correlated noise seen in 2010 was fixed (see Section 4.2.1). Also fewer science targets were observed in 2012 because both boresight star cameras had failed after six days. After the star cameras failed we switched to observing a $\sim$12 deg^2 region around Vela C. Vela C contains many bright sources for which the corresponding features in the bolometer TOD can hopefully be used to refine the pointing solution. A very large map of Puppis was observed when Vela was not visible. The Puppis data will be used to create Stokes I maps in order to investigate the submm properties of dust near the Galactic plane.

An additional column f_{other} has been added to Table 5.1. f_{other} is the fraction of time spent observing the source with a HWP angle greater than 3.0°away from one of the four nominal HWP positions (0°, 22.5°, 45°, 67.5°). The preliminary HWP angles are based on the HWP potentiometer readout, which occasionally are bad readings. f_{other} should decrease with a better calibration of the HWP angle based on the shaft encoder. There were several cases over the flight where the HWP potentiometer gave a bad reading which caused the stepper motor to rotate the HWP to the wrong position. These incorrect moves probably also account for some of f_{other}.

Finally the science map sizes for the BLASTPol 2012 flight are generally larger than maps made during the BLASTPol 2010 flight, in order to allow better coverage of low flux regions that can be used for referencing the I, Q and U zero points (Section 3.3.1). For our primary science target Vela C, the time observed listed in Table 5.1 includes 43 hours of science scans, 11 hours observing a much larger reference region, and 4 hours of elevation scans which will be used to obtain better cross-linking. Reference and elevation scans were also planned for Lupus I. Unfortunately the second star camera failed before the Lupus I observations could be completed (Section 3.4.3).

The quality of the 2012 data is much better than the quality of the 2010 data. In

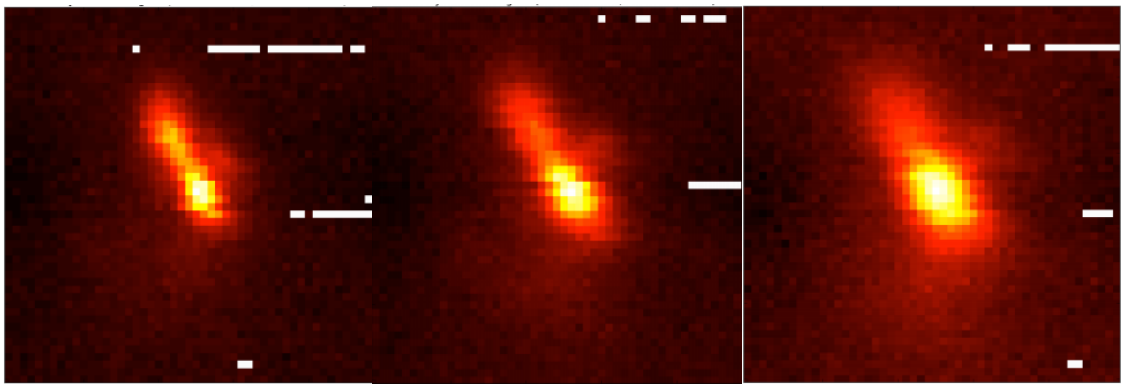

(a) 250 μm (b) 350 μm (c) 500 μm

Figure 5.1: Preliminary BLASTPol 2012 I maps of compact source IRAS 08470-4243 made using 38 minutes of data (Shariff, private communication), showing the elongation of the 2012 telescope beam. The white streaks visible in the maps show where there was insufficient pixel coverage to solve for I.

particular the instrumental polarization (IP) is far less than the 2010 IP, and for most targets there is more data and better HWP angle coverage because of the absence of the correlated noise seen in 2010.

5.2.2 2012 Beam Shape

While the analysis is still preliminary it appears that the BLASTPol 2012 telescope beam is non-Gaussian and non-symmetric. See Figure 5.1 for preliminary I maps made with 38 minutes of data. This could suggest that not all of the elongation of the 2010 beam was due to the damaged IR blocking filter, but that some was due to a deformation in the BLASTPol optics that was not present during the BLAST 2006 flight. BLASTPol uses a different primary mirror than BLAST. The abnormal beam shape may also be due to a deformation in one of the re-imaging optics elements.

So far there is no evidence that the 2012 beam shape varies with half-wave plate angle, unlike the 2010 beam. Observations were made of several compact source (IRAS 08470-4243, Saturn) or point source (VY CMa) calibrators so it should be possible

Target Name	Type[a]	Map Area (deg^2)	Time Obs (hrs)	Time Used (hrs)	f_0	$f_{22.5}$	f_{45}	$f_{67.5}$	f_{other}
Vela C[b]	GMC	3.1	61.30	57.41	0.238	0.247	0.240	0.244	0.031
Carina Nebula	GMC,C	2.0	4.62	4.33	0.226	0.248	0.252	0.254	0.021
G 331	GMC,C	2.0	4.52	4.05	0.219	0.218	0.274	0.269	0.020
Lupus I	DC	1.0	17.00	15.27	0.262	0.216	0.247	0.255	0.020
IRAS 08470-4243	Pt	0.1	2.58	2.46	0.318	0.183	0.268	0.217	0.014
Puppis	MC	0.4	13.73	12.86	0.243	0.262	0.230	0.247	0.018
VYCMa	S,Pt	0.1	5.60	4.76	0.194	0.203	0.242	0.303	0.058
Saturn	C	1	4.17	3.61	0.227	0.212	0.204	0.232	0.125
CG 12	DC	0.1	2.05	1.94	0.340	0.111	0.330	0.204	0.014
IRAS 15100-5613	Pt	0.1	1.01	0.41	0.248	0.218	0.094	0.381	0.058
Vela Y	MC	0.4	0.96	0.91	0.247	0.251	0.241	0.246	0.014
Vela Large[c]	GMC	12	99.95	90.71	0.236	0.233	0.2620	0.2466	0.0222
Puppis Large[c]		113	45.32	37.74	0.246	0.504	0.0838	0.165	0.0005

Table 5.1: Targets observed during the 2012 BLASTPol Antarctic Flight. Time used refers to all unflagged data (including pointing, bolometer and TDRSS flags) as calculated for the 500μm bolometer B5C05V. The final five columns give the fraction of the time used at each of the four HWP angles and f_{other}, the fraction of time the HWP angle was more than 3° away from one of the four nominal HWP angles.

[a] GMC: Giant Molecular Cloud, DC: dark cloud, MC: molecular cloud, IRDC: Infrared Dark Cloud, Pt: Pointing Calibrator, C: Polarization Calibrator, B: beam shape calibrator, G: Galaxy

[b] The time observed listed for Vela C includes 43 hours of science scans, 11 hours observing a much larger reference region, and 4 hours of elevation scans.

[c] Vela Large and Puppis Large were the science targets observed after both star cameras hard drives had failed.

to reconstruct and characterize the beam shape of BLASTPol from the 2012 data.

5.3 Changes to the Data Reduction Pipeline for 2012

The data reduction pipeline used to make the preliminary 2012 maps is almost the same pipeline used for the BLASTPol 2010 analysis and described in Chapter 4 with the following exceptions:

- *Preprocessor:* There were several changes made to the elevation correlation coefficient fitting pipeline described in Section 4.3.4:
  - Elevation correlation coefficients were fit to every elevation turn around, not just raster scans with one elevation direction change. Consequently there are lots of c_i fits at very low elevations ($El < 26^\circ$), from the Saturn elevation scans.
  - The median of c_i coefficients, c_m, was calculated for one degree bins in elevation, rather than the two degree bins used in 2010.
  - There were very few scans made at low to intermediate telescope elevations (26-31°) due difficulty operating the star cameras at low elevations, so median coefficients c_m were not calculated for these bins.

  Figure 5.2 shows a comparison between the elevation coefficients fit in 2010 (a) and 2012 (b) for a 500 μm bolometer.

- *TDRSS Flagging:* All bolometer data taken when the TDRSS transmitter was powered on (see Section 3.4.1) was flagged as bad. This corresponds to approximately 10% of the flight.

- *Correlated Noise Flagging:* Correlated noise between the science and dark detectors was not seen during the 2012 flight when the TDRSS transmitter was powered off, so additional noise flagging was not necessary.

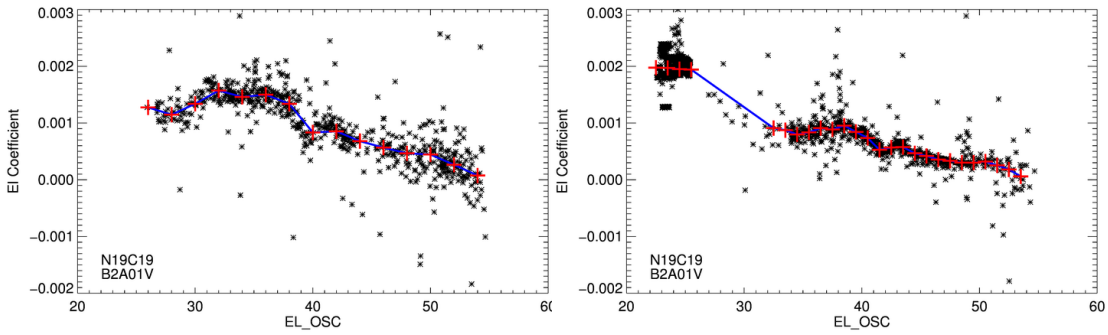

(a) 2010 (b) 2012

Figure 5.2: Elevation correlation coefficient fits for the same 250 μm bolometer B2A01V in 2010 vs 2012 . Black 'X's are individual c_i coefficients fit to each data chunk. Red plus signs are the median of all c_i coefficients c_m (within two degree bins in 2010 and one degree bins in 2012), and blue shows the linear interpolation between c_m coefficients used to subtract elevation correlated features from the bolometer TOD (see Section 4.3.4).

5.4 2012 Data Preliminary Run Through the Data Reduction Pipeline

In the next section I present preliminary polarization maps from the 2012 flight. The 2012 data was put through the 2010 pipeline (see Section 4.3) modified as described in Section 5.3. However several of the data reduction products are preliminary:

- *Pointing Solution:* The maps use an early version of the reconstructed pointing solution.

- *Bolometer Pointing Offsets:* The pointing offsets for each bolometer relative to the central bolometer are based on the offsets between the brightest pixels in single bolometer maps of the pointing calibrator IRAS 08470-4243 convolved with a 2′ FWHM Gaussian (Matthews, private communication). For the final dataset multi-Gaussian fits will be used to calculate beam centroids.

- *Star Camera Pointing Offsets:* Offsets between the boresight star camera axis and the telescope beam were only calculated for observations of the pointing calibrator IRAS 08470-4243. For the final dataset there will be an offset calculated for each data chunk for every BLASTPol target.

- *HWP Angles:* HWP angles were calculated using the potentiometer voltage (Section 2.7.4). However it is known from preflight tests that the HWP angle measurements from the potentiometer often have errors of 2-3 degrees and occasionally may have errors of tens of degrees.

- *Flatfielding:* No corrections for bolometer responsivity variation with time or flat fielding corrections have been applied to the input TOD.

Maps were made by running early versions of the 2012 data through the 2010 pipeline (preliminary mapmaking, IP determination, null test vector selection, final vector determination). The IP determined by the pipeline was very small, $<1\%$, and consistent with pre-flight measurements of $\sim 0.2\%$ (Matthews, private communication). As of the time of writing there is no evidence that the telescope beam shape varies with HWP angle. Reference regions used to define the I, Q and U flux zero points were larger and further from the bright cloud regions for the 2012 maps than for the 2010 maps.

To compensate for both the uncertainty in bolometer to bolometer pointing offsets (of order tens of arcseconds) and pointing offsets between the submm telescope beam and the star cameras, the maps were convolved with a Gaussian to reduce the resolution. The largest pointing uncertainty is probably due to the small number of measurements of the star camera axis to submm beam pointing offsets. In 2010 the difference between the maximum and minimum star camera offset was $2.0'$ in pitch and $3.0'$ in yaw (with a standard deviation of $0.48'$ and $0.75'$respectively). The range in offsets was less for targets that were observed over short periods of time

Target	$FWHM_{smooth}$ ($''$)	N_{vec}
Vela C	120	8253
Lupus I	150	217
Carina Nebula	60	3551

Table 5.2: List of preliminary BLASTPol 2012 maps shown in this chapter. $FWHM_{smooth}$ is the FWHM of the Gaussian used to smooth the I, Q and U maps, and N_{vec} is the total number of pseudovectors at 250, 350 and 500 μm which pass all six null tests and have $p >$1.5%, $I > 1.2\, I_{ref}$.

such as the Carina Nebula, which was observed in less than three hours and had star camera to beam offset variations of less than 30$''$peak-to-peak. The range in offsets was largest for Lupus I, which was observed fairly near the sun resulting in larger telescope thermal variations. The peak-to-peak differences in star camera pointing offsets for the 2010 observations of Lupus I were 1.76$'$ and 2.01$'$ in pitch and yaw respectively. Table 5.2 gives $FWHM_{smooth}$, which is both the FWHM of the Gaussian used to smooth the maps and the spacing between pseudovectors in each preliminary map.

No attempt has been made to assign statistical error bars to the vectors. Instead pseudovectors which pass all six null tests (see Section 4.4), as well as the same cuts applied to the 2010 pseudovectors ($p >$1.5%, $I > 1.2\, I_{ref}$) are shown. Table 5.2 lists the total number of pseudovectors shown for each map.

5.4.1 Preliminary BLASTPol 2012 Maps

Figures 5.3, 5.4 and 5.5 show preliminary maps from the 2012 flight. The smoothing FWHM and the number of pseudovectors displayed in each map can be found in Table 5.2. These maps are extremely preliminary and need several months of work before before they will be ready for rigorous scientific analysis. Nevertheless I will

finish the chapter with a few comments on the potential of these maps.

The 2012 data is a huge improvement over the 2010 data. In 2010 half the data had to be thrown away because of large correlated signals associated with motor switching and TDRSS transmission. Also BLASTPol had large instrumental polarization and a beam shape which varied with HWP angle.

These maps represent the most detailed look at magnetic field morphology in star forming regions to date, covering scales ranging from $\sim$50 pc (Carina) to the size scales associated with dense filaments ($3'$ corresponds to 0.14 pc at 155 pc, the distance to Lupus I). Once the 2012 pointing solution, and in particular the star camera to submm beam corrections, are improved the linear resolution of the BLASTPol 2012 maps will increase. In order to resolve structures on scales smaller than $\sim 1'$ a new map maker which can correct for the non-symmetric nature of the BLASTPol beam will be required.

As was the case for the 2010 data the map of the Carina Nebula (Figure 4.9) the BLASTPol 2012 pseudovectors show excellent agreement with the measurements made previously with the SPARO telescope (white lines). The 2012 data shows many changes in field direction, likely caused by the interaction between the magnetic field and the ionized gas associated with the many ionizing star clusters in this region.

The Vela C map (Figure 5.3) with over 8,000 pseudovectors shows a particularly detailed map of the magnetic field morphology of a young massive molecular cloud. In this view the field appears to be ordered on medium scales but is by no means uniform throughout the cloud. Indeed the direction of the field appears to change across the cloud. On the high right ascension side of the cloud the field direction appears closer to parallel to the cloud elongation direction, while on the other side the field appears closer to perpendicular to the cloud field direction.

Another interesting observation from Figure 5.3 is that the polarization is very strong in some areas which contribute little to the total submm flux of the cloud, but is very weak in some areas of the cloud that are submm bright such as the ”Southern

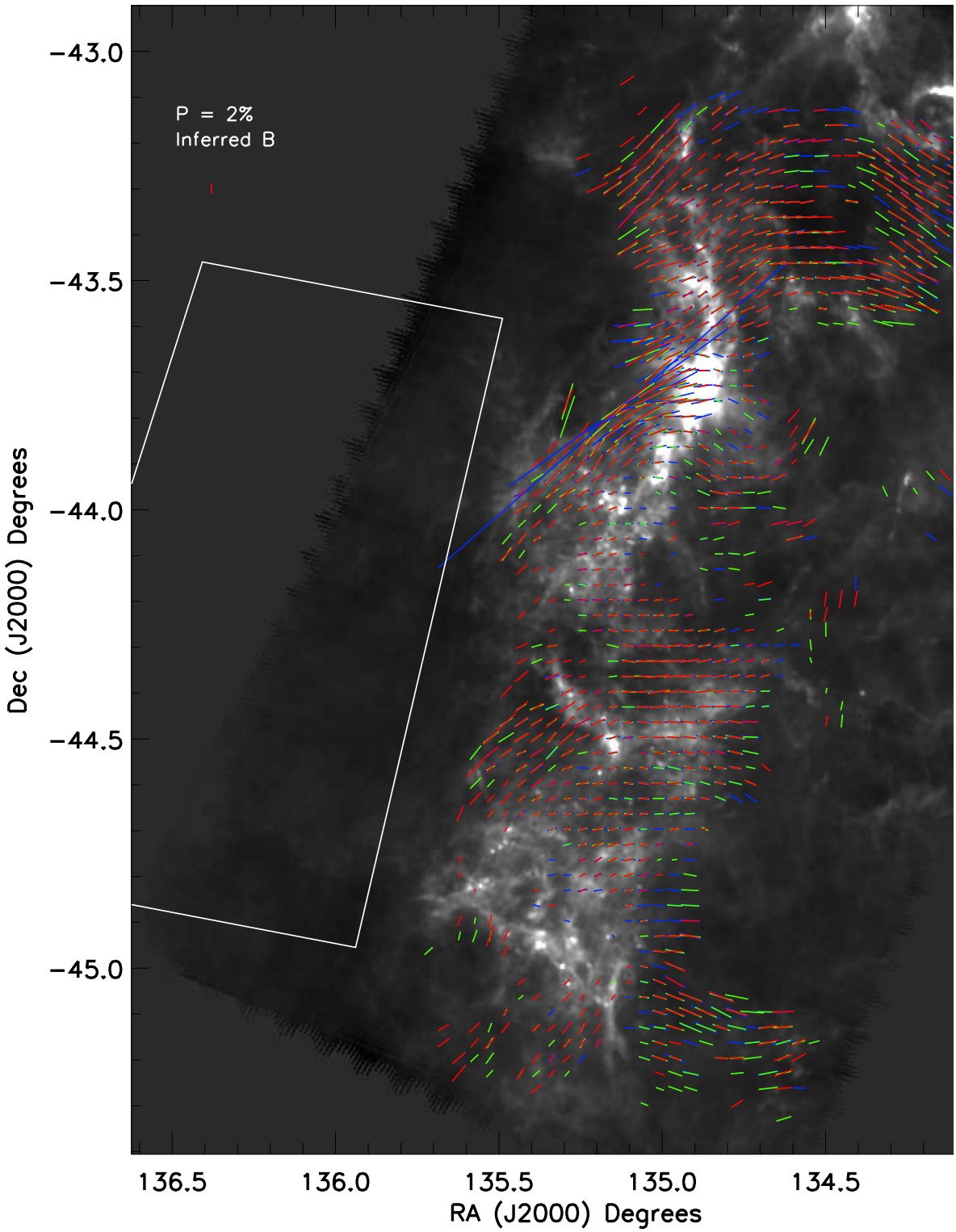

Figure 5.3: Preliminary BLASTPol 2012 Vela C map. The grayscale map is the Herschel SPIRE 350μm map of Vela C. Line segments represent polarization pseudovectors at 250μm (blue), 350μm (green) and 500μm (red) rotated by 90° to show the inferred direction of the magnetic field projected on the plane of the sky. The reference region used is outlined in white.

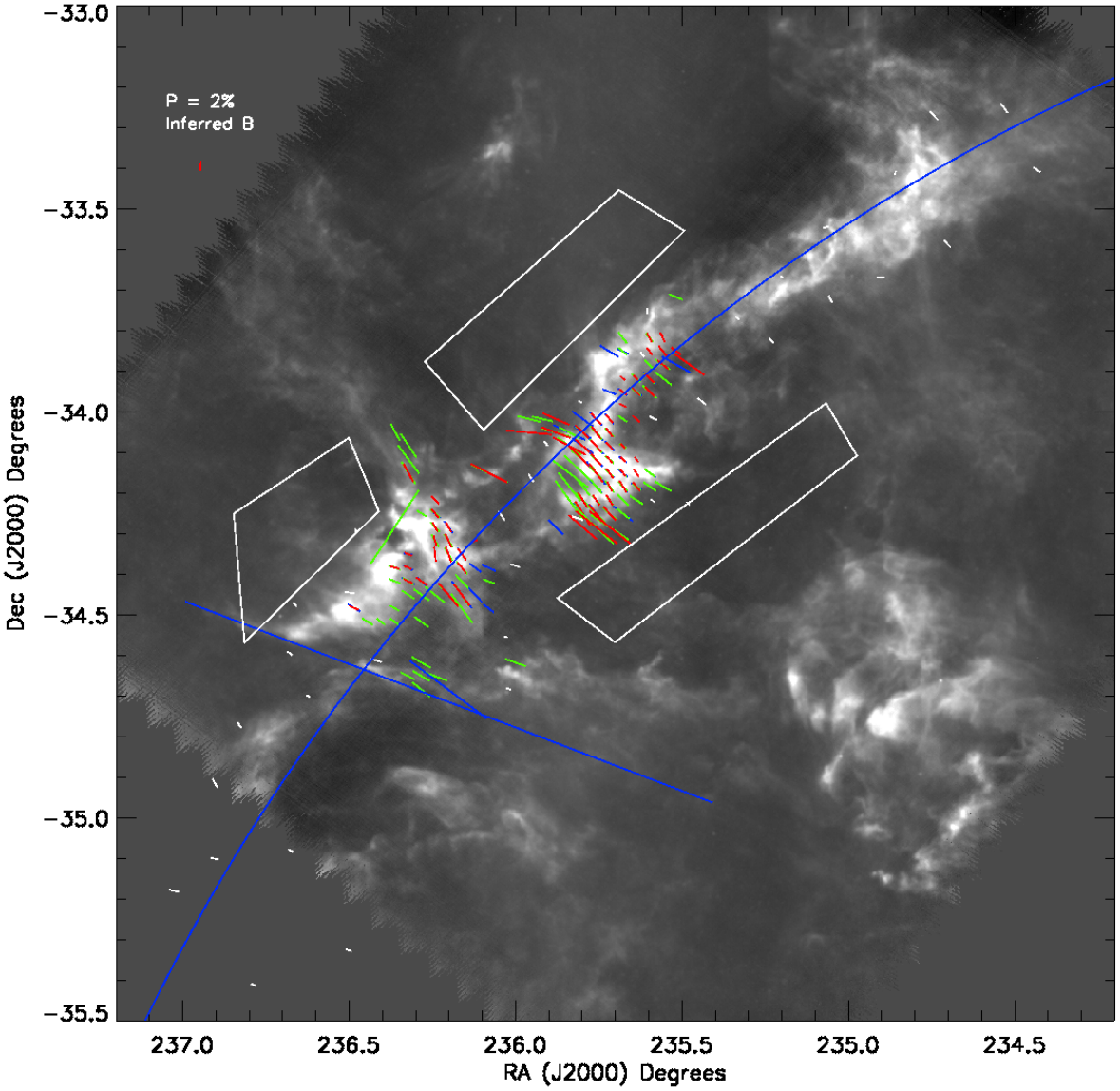

Figure 5.4: Preliminary BLASTPol 2012 Lupus I map. The grayscale map is the Herschel SPIRE 350μm map. Line segments represent polarization pseudovectors at 250μm (blue), 350μm (green) and 500μm (red) rotated by 90° to show the inferred direction of the magnetic field projected on the plane of the sky. White lines are optical polarimetry measurements from Rizzo et al. (1998). The reference regions used are outlined in white.

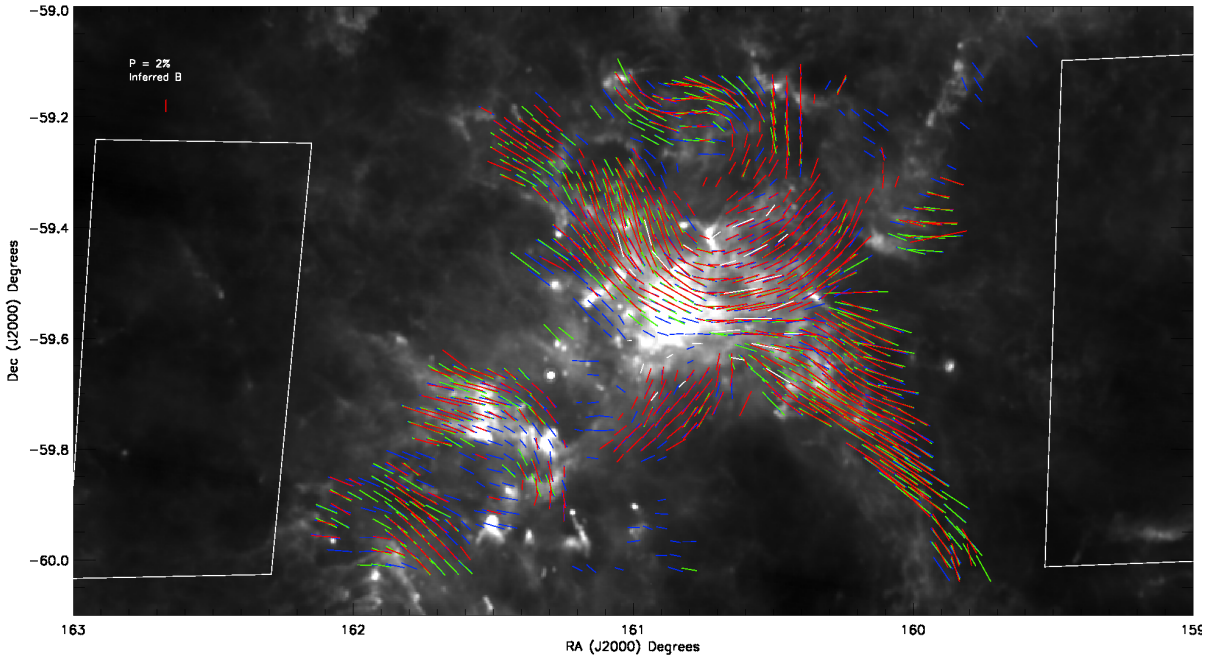

Figure 5.5: Preliminary BLASTPol 2012 Carina Nebula map. The grayscale map is the Herschel SPIRE 350μm map. Line segments represent polarization pseudovectors at 250μm (blue), 350μm (green) and 500μm (red) rotated by 90° to show the inferred direction of the magnetic field projected on the plane of the sky. White lines are 450μm polarization pseudovectors from SPARO observations (Li et al. 2006). The reference regions used are outlined in white.

Nest" identified by Hill et al. (2011), where the polarization is so weak that it fails in most cases to pass the p>1.5% threshold.

At a distance of ∼155 pc, Lupus I shown in Figure 5.4 is a much nearer cloud than Vela C. The BLASTPol 2012 maps show similar structure to the BLASTPol 2010 maps discussed in Matthews et al. (2013). In general the field is close to perpendicular to the main cloud filament, and in good agreement with the optical polarization measurements from Rizzo et al. (1998), but approximately four times more 2012 pseudovectors than 2010 pseudovectors pass the null tests.

5.5 Future Work

Before these maps will be ready for publication the data reduction products need to be finalized. In particular, the half-wave plate angles and star camera to submm beam offsets need to be improved.

With the 2010 data it was expected that the dominant error in the polarization angle determination would be systematics related rather than statistical, due to the melted filter. That assumption is probably not applicable to the 2012 data. For the 2012 data we will need to produce statistical error bars for our pseudovectors.

Our analysis of the data is limited by the fact that our mapmaker *naivepol* assumes uncorrelated and white noise. This means that we must high pass filter our TOD, so large scale modes are lost from the map. Work is underway to develop an optimal polarized mapmaker, but once complete it will need extensive testing through simulations.

Chapter 6

Summary & Future Work

6.1 Summary

My Ph.D. research focused on the design, construction, science planning and data analysis for BLASTPol, a balloon-borne submm telescope that maps linearly polarized radiation from dust grains in star forming regions. BLASTPol observes simultaneously at 250, 350 and 500 μm, with 30$''$ diffraction limited resolution at 250μm.

BLASTPol is unique in that it can trace magnetic fields across entire molecular clouds with resolution sufficient to follow the fields down into dense cloud substructures, such as cores and dense filaments. The experiment was designed to produce degree scale maps covering entire molecular clouds, with hundreds to thousands of independent polarization measurements per cloud.

BLASTPol had two scientific flights both launched from Antarctica. During the first 9.5 day flight launched in late December 2010 we encountered a number of problems. A damaged infrared blocking filter led to degradation of the optical performance of the telescope and significant instrumental polarization. Approximately half the 2010 data was rejected due to an additional highly correlated noise component. The reaction wheel motor, the primary azimuth pointing motor, failed a few hours into the

flight, however we were able to alter our motor control strategy to keep the telescope pointing.

Problems with the instrument were fixed for the second BLASTPol flight, launched in late December 2012, which lasted 16 days (the cryogens only lasted 12.5 days). The instrument performed nearly perfectly, with the exception of the star camera hard drives both of which had failed after six days. Before the star cameras failed we were able to complete our calibrator observations, observations of our primary science target (the Vela C molecular cloud) and 17 hours of observations of our secondary science target Lupus I.

A data reduction pipeline was constructed for the 2010 data which cleans the detector TOD, reconstructs telescope pointing, calculates and removes instrumental polarization, references the maps, and creates final polarization maps. Because uncertainties in the 2010 data are likely dominated by systematics from the damaged filter, statistical errors were not used to select polarization pseudovectors. Instead a series of "null" or internal consistency tests were used to test for systematics and reject potentially contaminated pseudovectors. This pipeline was tested with simulated BLASTPol observations, and I showed that even with a polarized beam and large instrumental polarization BLASTPol can reconstruct the mean instrumental polarization to $<0.5\%$ and the global polarization direction to $\sim 5^{\circ}$.

Data analysis for the 2012 flight is still ongoing, but running the preliminary data through the 2010 analysis pipeline results in an impressive set of maps that highlight the potential of the data.

6.2 Future Work

More work is needed to finalize the 2012 data reduction products. A new map maker is also needed. This mapmaker needs to be able to handle correlated noise and a non-symmetric beam. In addition a more robust, quantitative, simulation pipeline is

required that can generate and analyze a large number of simulations, which can be used to understand the uncertainties of the 2012 polarization pseudovectors.

The final science maps will be used to probe the role played by magnetic fields in star formation. The magnetic field morphology will be compared to both molecular cloud morphology (e.g. filamentary structure) and morphology of prestellar and protostellar cores within the clouds. The goal is to provide quantitative tests of predictions from numerical simulations of star formation (e.g. Soler et al. (submitted)).

Work is also underway to assemble a complementary dataset that can be used to probe other cloud physics and build a more complete model of the BLASTPol target clouds. For example for the Vela C molecular cloud we have access to high resolution Herschel far infrared data, infrared data from WISE and information on the gas velocity structure from Mopra CO,^{13}CO and C^{18}O cubes of the J=1-0 transition.

Finally, work is beginning on a next-generation or "SuperBLASTPol" polarimeter, which will have a larger 2.5 m mirror for better linear resolution and will incorporate a focal plane of $\sim$1000 dual-polarization sensitive MKIDS bolometers for $\sim 16\times$ the mapping speed of BLASTPol. The telescope has funding from NASA and a first flight is planned for late 2016.

Bibliography

Ade, P., Bock, J., Bowden, M., et al. 2008, ApJ, 674, 22

Ade, P. A. R., Pisano, G., Tucker, C., & Weaver, S. 2006, in Society of Photo-Optical Instrumentation Engineers (SPIE) Conference Series, Vol. 6275, Society of Photo-Optical Instrumentation Engineers (SPIE) Conference Series

André, P., Men'shchikov, A., Bontemps, S., et al. 2010, A&A, 518, L102

Angilè, F. 2011, Unpublished internal memo

Angile, F. 2013, PhD thesis, University of Pennsylvania

Angilè, F. E. in press, ApJ

Basu, S., & Ciolek, G. E. 2004, ApJ, 607, L39

Beck, R. 2001, Space Science Reviews, 99, 243

Bethell, T. J., Chepurnov, A., Lazarian, A., & Kim, J. 2007, ApJ, 663, 1055

Bonnor, W. B. 1956, MNRAS, 116, 351

Brown, R. L., Wild, W., & Cunningham, C. 2004, Advances in Space Research, 34, 555

Chandrasekhar, S., & Fermi, E. 1953, ApJ, 118, 113

Comerón, F. 2008, The Lupus Clouds, ed. B. Reipurth, 295

Crutcher, R. M. 2012, ARA&A, 50, 29

Davidson, J. A., Novak, G., Matthews, T. G., et al. 2011, ApJ, 732, 97

Devlin, M. J., Ade, P. A. R., Aretxaga, I., et al. 2009, Nature, 458, 737

Dobashi, K., Uehara, H., Kandori, R., et al. 2005, PASJ, 57, 1

Dotson, J. L., Novak, G., Renbarger, T., Pernic, D., & Sundwall, J. L. 1998, in Society of Photo-Optical Instrumentation Engineers (SPIE) Conference Series, Vol. 3357, Society of Photo-Optical Instrumentation Engineers (SPIE) Conference Series, ed. T. G. Phillips, 543–547

Dotson, J. L., Vaillancourt, J. E., Kirby, L., et al. 2010, ApJS, 186, 406

Ebert, R. 1957, Zeitschrift fur Astrophysik, 42, 263

Fissel, L. M., Ade, P. A. R., Angilè, F. E., et al. 2010, in SPIE, Vol. 7741

Girart, J. M., Beltrán, M. T., Zhang, Q., Rao, R., & Estalella, R. 2009, Science, 324, 1408

Glenn, J., Bock, J. J., Chattopadhyay, G., et al. 1998, in Proc. SPIE, Advanced Technology MMW, Radio, and Terahertz Telescopes, Thomas G. Phillips; Ed., Vol. 3357, 326–334

Goldsmith, P. F., Heyer, M., Narayanan, G., et al. 2008, ApJ, 680, 428

Goodman, A. A., Bastien, P., Menard, F., & Myers, P. C. 1990, ApJ, 359, 363

Greaves, J. S., Holland, W. S., Jenness, T., et al. 2003, MNRAS, 340, 353

Griffin, M. J., Swinyard, B. M., & Vigroux, L. G. 2003, in IR Space Telescopes and Instruments. Edited by John C. Mather . Proceedings of the SPIE, Vol. 4850, 686–697

Hanany, S., Hubmayr, J., Johnson, B. R., et al. 2005, Appl. Opt., 44, 4666

Harman, R. R. 2005, Wilkinson Microwave Anisotropy Probe (WMAP) Attitude Estimation Filter Comparison, Tech. rep., Flight Mechanics Symposium; Greenbelt, MD

Heiles, C., & Crutcher, R. 2005, in Lecture Notes in Physics, Berlin Springer Verlag, Vol. 664, Cosmic Magnetic Fields, ed. R. Wielebinski & R. Beck, 137–+

Heyer, M., Gong, H., Ostriker, E., & Brunt, C. 2008, ApJ, 680, 420

Hildebrand, R. H., Kirby, L., Dotson, J. L., Houde, M., & Vaillancourt, J. E. 2009, ApJ, 696, 567

Hill, T., Motte, F., Didelon, P., et al. 2011, A&A, 533, A94

Hoang, T., & Lazarian, A. 2008, MNRAS, 388, 117

Houde, M., Rao, R., Vaillancourt, J. E., & Hildebrand, R. H. 2011, ApJ, 733, 109

Houde, M., Vaillancourt, J. E., Hildebrand, R. H., Chitsazzadeh, S., & Kirby, L. 2009, ApJ, 706, 1504

Johnson, B. R., Collins, J., Abroe, M. E., et al. 2007, ApJ, 665, 42

Lazarian, A. 2007, J. Quant. Spec. Radiat. Transf., 106, 225

Li, H., Griffin, G. S., Krejny, M., et al. 2006, ApJ, 648, 340

Mac Low, M.-M., & Klessen, R. S. 2004, Reviews of Modern Physics, 76, 125

Markley, F. L. 2003, Journal of Guidance, Control, and Dynamics, 26, 311

Marsden, G., Ade, P. A. R., Benton, S., et al. 2008, in Society of Photo-Optical Instrumentation Engineers (SPIE) Conference Series, Vol. 7020, Society of Photo-Optical Instrumentation Engineers (SPIE) Conference Series

Marsden, G., Ade, P. A. R., Bock, J. J., et al. 2009, ApJ, 707, 1729

Matthews, B. C., McPhee, C. A., Fissel, L. M., & Curran, R. L. 2009, ApJS, 182, 143

Matthews, B. C., Wilson, C. D., & Fiege, J. D. 2001, ApJ, 562, 400

Matthews, T. 2013, personal communication

Matthews, T., Ade, P., Elio Angilè, F., et al. 2013, submitted to ApJ, arXiv:1208.4866

Matthews, T. G. 2013, PhD thesis, Northwestern University

McKee, C. F., & Ostriker, E. C. 2007, ARA&A, 45, 565

Mizuno, A., & Fukui, Y. 2004, in Astronomical Society of the Pacific Conference Series, Vol. 317, Milky Way Surveys: The Structure and Evolution of our Galaxy, ed. D. Clemens, R. Shah, & T. Brainerd, 59

Moncelsi, L., Ade, P., Elio Angilè, F., et al. 2012, ArXiv e-prints, arXiv:1208.4866

Nakamura, F., & Li, Z.-Y. 2008, ApJ, 687, 354

Nakamura, F., & Li, Z. Y. 2011, ApJ, 740, 36

Netterfield, C. B., Ade, P. A. R., Bock, J. J., et al. 2009, ApJ, 707, 1824

Novak, G. 2010, Polarization Measurement Conventions for BLAST-Pol version 4, Unpublished internal memo

Olmi, L. 2002, in Highly Innovative Space Telescope Concepts Edited by Howard A. MacEwen. Proceedings of the SPIE, Vol. 4849, 245–256

Ostriker, E. C., Stone, J. M., & Gammie, C. F. 2001, ApJ, 546, 980

Palmeirim, P., André, P., Kirk, J., et al. 2013, A&A, 550, A38

Pascale, E., Ade, P. A. R., Bock, J. J., et al. 2008, ApJ, 681, 400

Pascale, E., Ade, P. A. R., Bock, J. J., et al. 2009, ApJ, 707, 1740

Pettersson, B. 2008, Young Stars and Dust Clouds in Puppis and Vela, ed. B. Reipurth, 43

Pisano, G., Savini, G., Ade, P. A. R., Haynes, V., & Gear, W. K. 2006, Appl. Opt., 45, 6982

Pittelkau, M. E. 2001, Journal of Guidance, Control, and Dynamics, 24, 1187

Planck Collaboration, Ade, P. A. R., Aghanim, N., et al. 2011, A&A, 536, A1

Renbarger, T., Chuss, D. T., Dotson, J. L., et al. 2004, PASP, 116, 415

Rex, M., Chapin, E., Devlin, M. J., et al. 2006, in Presented at the Society of Photo-Optical Instrumentation Engineers (SPIE) Conference, Vol. 6269, Ground-based and Airborne Instrumentation for Astronomy. Edited by McLean, Ian S.; Iye, Masanori. Proceedings of the SPIE, Volume 6269, pp. 62693H (2006).

Rizzo, J. R., Morras, R., & Arnal, E. M. 1998, MNRAS, 300, 497

Rownd, B., Bock, J. J., Chattopadhyay, G., Glenn, J., & Griffin, M. J. 2003, in Millimeter and Submillimeter Detectors for Astronomy. Edited by Phillips, Thomas G.; Zmuidzinas, Jonas. Proceedings of the SPIE, Vol. 4855, 510–519

Savini, G., Pisano, G., & Ade, P. A. R. 2006, Appl. Opt., 45, 8907

Shu, F. H., Adams, F. C., & Lizano, S. 1987, ARA&A, 25, 23

Smith, M.D. 2004, The Origin of Stars (Imperial College Press, London)

Soler, J. 2013, PhD thesis, University of Toronto

Soler, J. D., Hennebelle, P., Martin, P. G., et al. submitted, submitted to ApJ, arXiv:1303.1830

Srisuwananukorn, A. 2013, Non-detection of Submillimeter Polarization by Rayleigh Scattering in Saturn's B-Ring, Undergraduate Honors Thesis, Northwestern University

Tomisaka, K., Ikeuchi, S., & Nakamura, T. 1988, ApJ, 335, 239

Vaillancourt, J. E., Dowell, C. D., Hildebrand, R. H., et al. 2008, ApJ, 679, L25

Ward-Thompson, D., Kirk, J. M., Crutcher, R. M., et al. 2000, ApJ, 537, L135

Ward-Thompson, D., Sen, A. K., Kirk, J. M., & Nutter, D. 2009, MNRAS, 398, 394

Wiebe, D. 2008, PhD thesis, University of Toronto

Yamaguchi, N., Mizuno, N., Saito, H., et al. 1999, PASJ, 51, 775

Zhang, J., Ade, P. A. R., Mauskopf, P., et al. 2009, Appl. Opt., 48, 6635